Investigations on the Impact of Ions on the Air-Water-Interface

Dissertation

zur Erlangung des Doktorgrades der Naturwissenschaften (Dr. rer. nat.)
der Naturwissenschaftlichen Fakultät IV - Chemie und Pharmazie
der Universität Regensburg

vorgelegt von:

Eva Brandes

aus Göttingen

2019

Promotionsgesuch eingereicht am:	16. Mai 2019
Tag des Kolloquiums:	15. Juli 2019
Diese Arbeit wurde angeleitet von:	Prof. Dr. Hubert Motschmann
Prüfungsausschuss:	Prof. Dr. Hubert Motschmann
	apl. Prof. Dr. Richard Buchner
	Prof. Dr. Arno Pfitzner
Vorsitzender	Prof. Dr. Robert Wolf

Danksagung

Diese Doktorarbeit entstand am Institut für Physikalische und Theoretische Chemie der Universität Regensburg. Ohne die Zusammenarbeit und dem Austausch mit einer Reihe von Menschen wäre dies nicht möglich gewesen.

Zuallererst möchte ich mich bei Hubert Motschmann bedanken. Er hat mich herzlich in seine kleine aber feine Arbeitsgruppe aufgenommen und mich in die faszinierende Welt der Grenzflächenspektroskopie entführt. Zudem hat er mir ermöglicht, an zahlreichen Konferenzen teilzunehmen, somit konnte immer auch ein bisschen über den Tellerrand hinauszugucken.

Besonderer Dank gilt auch Peter Karagiogiev, er hat mich mit großer Geduld in die technische Welt der Laserspektroskopie eingeführt und stand mir immer mit Rat und Tat zur Seite.

Im Rahmen dieser Arbeit habe ich die Möglichkeit bekommen, hochinteressante Messungen mit Hilfe der Dielektrischen Relaxationsspektroskopie durchführen zu können. Ich möchte Richard Buchner dafür danken, dass er mir diese Messungen ermöglicht hat und mir bei der Interpretation der Daten sehr geholfen hat. Ohne die Hilfe von Andreas Nazet wäre mir die technische Durchführung nicht möglich gewesen.

Für die Zusammenarbeit an dem Katalyse-System möchte ich Stefan Troppman, Antonin (Tonda) Kralik und Burkhard König danken. Sie haben mir dieses interessante System vorgestellt und die Proben dafür synthetisiert.

Ich möchte allen Mitgliedern des Lehrstuhles Kunz danken, insbesondere meinen Arbeitsgruppenkollegen Christian Luigs, Matthias Hofmann, Alexander Dietz, Ulrike Paap und Dominik Feucht. Es war immer möglich einen Ansprechpartner für Fragen und Hilfestellungen zu finden.

Für die schönen Mittagspausen möchte ich vor allem Beate Möser, Christoph Hölzl, Ragnheiður (Heiða) Guðbrandsdóttir und Philipp Dullinger danken. Neben den Mittagspausen entwickelte sich die Spieleabende zu einem fast wöchentlichen

Highlight. Insbesondere unser Kampf gegen die Epidemie in Pandemic Lagacy wird mir als bleibendes Erlebnis in Erinnerung bleiben, aber auch die vielen anderen Brettspiele die wir im Laufe der Jahre spielten.

Ein besonderer Dank gilt meinen Eltern und insbesondere meinem Freund Drewes, die mir immer den Rücken freigehalten haben und mich bei allen meinen Tätigkeiten immer unterstützt haben.

Contents

1 Introduction

Water covers over seventy percent of the earth, most of it is salt water stored in the oceans. Additionally to the surface water, a large amount of water is located in the atmosphere, where it governs not only the weather, but is as well one major source of the natural greenhouse effect.[1]

Water is a quite peculiar liquid; it is famous for its density anomaly and its extended hydrogen bond network. Additionally to the exceptional bulk behavior there occur some surprising effects at the surface, too. These effects play little role for e.g. sea water, which acts in most cases as a more or less homogeneous bulk. However, in the atmosphere, surface effects of water droplets become more dominant. This is due to the high surface to bulk ratio of the droplets. Additionally, surfaces are the predominant feature of all reactions in inhomogeneous systems. Therefore, it is worth to take a closer look at the water surface in various instances.

Interfaces are hard to investigate. This is the reason why many effects are still under discussion or yet wait to be discovered. Interfaces make up only a tiny fraction of the system and have a quite small geometrical extension. Nevertheless, they are frequently the site of reactions and phenomena that dominate the macroscopic properties of the entire system. Hence, the understanding of the self-organization of molecules at interfaces is a central theme of colloid and interface science.

Linear and nonlinear optical reflection techniques are powerful tools in the armory of surface scientists that deepened our understanding of the interfacial architecture. In the recent years the picture of the air-water interface was altered, especially the non-monotonic concentration profile of ions was introduced as a new concept. It shows that the interface should be rather termed as *interphase*, because it has a vertical extension and is far more than just a dividing surface.

To investigate the air-water interface I used a surface specific spectroscopy –

namely SFG spectroscopy. Not the pure air-water interface was in focus, but rather the structural changes of the interface upon the modification with a salt, or with a membrane. The pure air-water interface shows already many interesting features, however, the presence of other substances proved to have great impact on the interfacial water. I investigated both, the impact of the interface on the probe and vice versa. This was accomplished by the simultaneously observation of the resonances of the probe itself and of the interfacial water. Additionally, I paid special attention to the effect of the counterions. Counterion binding is known to have a great impact on the interfacial structure.

In this thesis three systems were investigated. The pure electrolyte-air interface of two octahedral metal complexes showed some interesting features, which could be correlated to the bulk structure (section 4). A photoelectric catalytic system was investigated, and structural effects proved to be an important factor for the optimization of the reaction (section 5). In the third part the concentration dependent counterion pairing of a charged amphiphile could be described (section 6). All of these very different systems showed interesting features in the interfacial region.

2 Theory

In this chapter the most important theoretic concepts used in this thesis are presented. Liquids in general and liquid surfaces in particular are a complex system with many possible approaches for the theoretical description. The schemes shown in the following give a first insight in the general structure of water and electrolytes and then introduce basic theories of light matter interaction. The latter is the basis for the methods introduced in chapter 3.

2.1. Ion Specificity

Ions are in the most simple approach (see section 2.2) described as point charges with only electrostatic interaction with the surrounding. This picture is far too simple and does not capture the variety of ion phenomena. Especially the polarizability and the solvation shell of ions leads to ion specific behavior. The first experimental data on this topic were produced by Franz Hofmeister in 1888. He studied the denaturation of proteins using dissolved egg white by adding salt. The experiments revealed a dependence on the nature of the salt, which cannot be explained models assuming only point charges.[2] Hofmeister introduced an order for both, anions and cations, which is well known as the *Hofmeister* or *lyotropic series*. He noted that the monitored effects are most likely based on a series of interactions such as lyotropic swelling of proteins, water binding or osmotic pressure.[3] Although this series was developed on proteins it turned out that the order of the ions appear in various contexts. Some examples are shown in section 2.2.3. Since the publication of Hofmeister there have been many efforts to give a physical description of the ion specificity. The more research on the topic was carried out, the more questions arose. For example in the investigations of Klobusitzsky from 1925 some anions change place when changing the cation from potassium to sodium.[4] This indicates a strong impact of the counter ion on the

structure, anions and cations cannot be described separately. Even until this day there is no unifying theory of the Hofmeister effects, the *Holy Grail* of solution chemistry.[5]

2.1.1. Structure Maker and Structure Breaker

It is undeniable that the impact of the ions on water is one of the major causes of the Hofmeister effects. Depending on the nature of the ion, the induced structure may vary. Small ions have a higher charge density than large ones of the same charge. The key idea is to put the ion-ion interaction in relation to the ion-water interaction. Small ions have a large impact on the surrounding water even beyond the first hydration shell. These ions are called *structure maker.*[6] Large ions are termed as *structure breaker.*[7] Very similar to these expressions are the terms *kosmotropic* and *chaotropic*, which were introduced by Collins and Washbough in 1985.[8]

2.1.2. Law of Matching Water Affinities

Collins predicted the formation of contact ion pairs depending on the competitive interactions of the ions with their counterions and with water. This concept is referred to as the *law of matching water affinities*. Hard ions have a very strong interaction with other hard ions. A little bit less strong is the interaction of hard ions with water. For soft ions this relationship is the other way round, they experience stronger interactions with water than with other soft counterions. The water-water interaction is somewhere in the middle of these two extremes. Two hard ions will prefer the direct interaction, instead of being solvated by water. When there are only soft ions in the solution, the predominant interaction is between the water molecules. They bind more likely to themselves than solvating the soft ions, which form as a consequence ion pairs. Only in a mixture of soft and hard anions and cations the ions will be separated from each other. This prediction seems to correlate with experimental data. For example the solubility of alkali halides experiences a minimum at matching water affinities (see table 2.1). However, in this model solvent separated ion pairs cannot be described (see section 3.2.3).

One example for ion pairing affects the taste of coffee. One major component of coffee responsible for the bitter taste is caffeine, which is mainly known for

[mol/L]	F^-	Cl^-	Br^-	I^-
Li^+	**0.1**	19.6	20.4	8.8
Na^+	1.0	6.2	8.8	11.9
K^+	15.9	**4.8**	7.6	8.7
Rb^+	12.5	7.5	6.7	7.2
Cs^+	24.2	11.0	**5.1**	**3.0**

Table 2.1.: Solubility of different alkali halides.[9] The lowest solubility of each anion is marked in bold.

its stimulating properties. Caffeine tends to form to a certain extent dimers. Other than the monomers, the dimers are not bitter.[10] The extent of dimerization strongly depends on other additives in the solution, such as salts or sugar. Kosmotropes tend to lead to dimerized caffeine, while more monomers form upon the addition of chaotropes.[11] There are some recent measurements on the system suggesting that this effect results from competitive binding. Caffeine prefers to bind to added chaotropes instead of forming dimers. On the other hand, kosmotropes are excluded from the caffeine vicinity, leading to a dimerization of the caffeine. The highly hydrated sucrose acts as a kosmotrope. The less bitter taste of sweetened coffee is therefore not only pure imagination, but rather a result from the dimerization of caffeine.[12]

2.2. Theories on the Ion Distribution at Interfaces

The description of ion distributions at charged or non-charged interfaces evoke a series of theories and improvements of the theories in the past. Some are based on first principles, some use a variety of fit parameters, but all of them try to solve the puzzling question of ion behavior close to the interface. In this section I want to give a historic overview over the zoo of theories. First these theories were proposed for the case of a charged metal surface exposed to the electrolyte. This picture was modified also for other system such as a charged amphiphile at the air-electrolyte interface.

The electrostatic interaction of dissolved ions with the solvation molecules gets usually described by the Poisson Boltzmann equation. Here the ions are treated as point charges and only the interaction between ions and the influence of the thermal motion is captured. Interactions of ions are calculated relative to the

mean field instead of individual interactions. This approach gives reasonable results for concentrations smaller than 200 mM and potentials lower than 50 mV.[13]

2.2.1. Charged Interfaces

There are several models trying to describe the electrostatic structure at charged interfaces. In figure 2.1 an overview over the different double layer models is given, which will be discussed in the following.

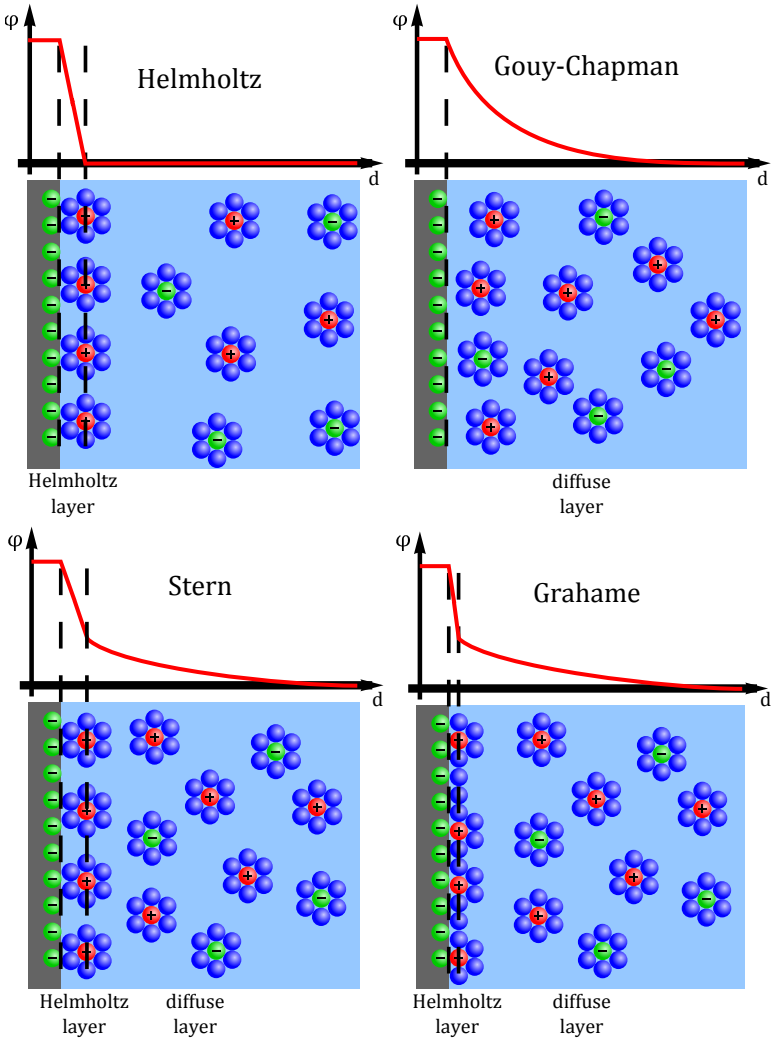

Figure 2.1.: Comparison of the ion distribution and the electric potential φ for different double layer models (for details see text).

Helmholtz Double Layer

Hermann von Helmholtz was the first one to tackle the ion distribution at a charged interface. He introduced the term electric double layer.[14] His approach is, similar to many early concepts, based purely on electrostatic. He predicted a single counter ion layer adjacent to the charged surface. In this oversimplification thermal motion, ion diffusion, adsorption onto the surface and solvent-surface interaction are considered negligible. The resulting electric potential φ decreases in a linear fashion from the charged interface to the liquid bulk value.

Gouy-Chapman Double Layer

The static picture introduced by Helmholtz was improved by Louis Georges Gouy and David Leonard Chapman independently in separate publications in 1910[15] and 1913[16], respectively. Instead of fixed point charges the ions are subject to Brownian motion. No Helmholtz layer is formed, and the ion concentration decays exponentially. The extension of the diffuse layer is far reaching into the liquid. With this approach, Maxwell-Boltzmann statistics can be applied. The great drawback of this theory is the negligence of spatial extension of the ions, which allow unrealistic high ion concentrations at the interface. However, for very small concentrations in the range below one millimolar, this model gives reasonable results.

Stern Layer

To overcome the limited concentration range of previous approaches, Otto Stern combined in 1924 the static layer of Helmholtz with the diffuse concentration profile of the Gouy-Chapman theory.[17] Some ions are specifically adsorbed to the interface and form the so-called Stern layer. The finite size of ions is taken into account, which limits the closest approach of an ion to the charged interface by the ionic radius. The electric double layer is assumed to be thin compared to the size of the particles. No Brownian motion is taken into account in this layer. Major drawbacks of this method are the constant dielectric permittivity and viscosity throughout the diffuse layer and disregard of all interactions other than coulombic.

Grahame's Modification

David C. Grahame altered the Stern model in 1947 in order to overcome some of the problems.[18] He noted that the electrode is usually occupied by solvent molecules. The ions would have to lose its solvation shell allowing them to get in contact with the charged surface. He divided the Helmholtz layer in an inner and an outer part, where the inner plane is defined via the radius of the adsorbed solvent molecules and the outer plane by the distance of the center of the ions at the closest approach to the electrode. These layers are followed by the diffuse layer.

Other Non-Ionspecific Theories

After the basic setup many more approaches followed. The description was e.g. altered by an introduction of a finite size of the ion, the dependence of the dielectric constant on the electric field, image forces or ion correlation.[19–22] In all cases a combination of a static layer followed by a diffuse layer is used.

2.2.2. Ion Specificity at Air-Electrolyte Interfaces

At the air-electrolyte interface many ion specific effects can be observed. Ions are attracted by the interface by dipole - induced dipole interactions, and are at the meantime repulsed from the surface by electrostatic interactions. Depending on the nature of the ions, e.g. the polarizability, one or the other contribution dominates. In electrolyte solutions the electrostatic contribution is always strongly dependent on the counterion distribution. Furthermore, the interfacial water structure reorients upon addition of ions, which may alter the ion contribution. The interaction of all these properties leads to a complex picture, where it is a difficult task to interpret experimental data in a meaningful manner.

With classical thermodynamics it is possible to describe equilibria at interfaces. This is based on the Gibbs energy G with the easily accessible variables pressure p and temperature T. If a surface is present, the surface tension γ and the surface area A are included. The differential of the Gibbs energy dG is a function of the pressure, the temperature, the number of particles n_i of the phase i and of the surface area.

$$dG = V\,dp - S\,dT + \sum_\mathrm{i} \mu_\mathrm{i} dn_\mathrm{i} + \gamma\,dA \tag{2.1}$$

If the surface area is increased, the Gibbs energy change depends on the surface tension.

The surface tension is strongly dependent on the interfacial structure. It results from the cohesive force between molecules. In the bulk this cohesive force pulls the molecule isotropically in all directions. At the surface the lack of binding partners leads to an asymmetric picture (see figure 2.2). Since the attractive force pulls the molecules at the interface in the direction of the bulk, a defined surface is formed.

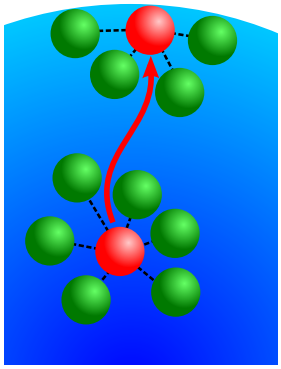

Figure 2.2.: Change in the coordination number upon pushing a molecule from the bulk to the surface and creating a new surface area.

The surface tension can be approximated with a simple approach. At constant pressure, temperature and particle number the surface tension only depends on the energy and the surface area. The energy can be estimated by the coordination number z_i and the corresponding binding energy w_AA. The change in area is just given by the area of the molecule (r^2, rough estimation via the radius). This assumes that the observed molecule pushes the molecules at the surface to the side and creating a new surface.

$$\gamma = \left(\frac{\partial G}{\partial A}\right)_{\mathrm{p,T,n_i}} \approx \frac{\Delta E}{\Delta A} \approx \frac{w_\mathrm{AA}}{2}\frac{z_\mathrm{B} - z_\mathrm{S}}{r^2} \tag{2.2}$$

The coordination numbers of the bulk are usually larger than at the surface. The binding energy can be estimated by the enthalpy of vaporization ΔH_vap. For simple molecules, such as CCl_4 this estimation gives reasonable values.

In the systems investigated in this thesis, this approach is too simple. Gibbs introduced the quantity of the surface excess $\Gamma_\mathrm{i} = \frac{n_\mathrm{i}}{A}$, where the number of moles of component n_i is set in relation to the interfacial area A. The total differential

of the surface tension γ is now only dependent on the surface excess and the chemical potential μ_i.

$$-d\gamma = \sum_\mathrm{i} \Gamma_\mathrm{i} \mu_\mathrm{i} \tag{2.3}$$

One of these components is the solvent, others are in the case of a univalent salt the anion, the cation and the undissociated salt. The Gibbs dividing surface is chosen such that the term of the solvent vanishes.[23] With the definition of the chemical potential it is possible to derive the Gibbs adsorption isotherm.

$$-d\gamma = mRT\Gamma_2 d\ln a_1 \tag{2.4}$$

$$\approx mRT\Gamma_2 d\ln c_1 \tag{2.5}$$

For dilute solutions the activity a_1 can be replaced by the concentration c_1. The coefficient m takes the dissociation into account. For a univalent ion the extrema are $m = 2$ for a completely dissociated salt and $m = 1$ for an undissociated salt.[24] For partially dissociated salts the value is in between.[25]

The surface excess is the excess of the surface concentration over the bulk concentration. A common representation is a plot of the surface tension versus the logarithm of the concentration.

$$\Gamma_2 = -\frac{1}{mRT}\frac{d\gamma}{d\ln a_\mathrm{i}} \tag{2.6}$$

$$\approx -\frac{1}{mRT}\frac{d\gamma}{d\ln c_\mathrm{i}} \tag{2.7}$$

A negative slope indicates a positive surface excess, which is interpreted as an enriched surface, a negative sign of Γ_1 is attributed to a depletion. In figure 2.3 two possible surface pressure plots are shown.

Measuring the concentration dependence of the surface tension is rather easy (see section 3.3.1). The systems can be classified in two categories, either a positive or a negative slope of the isotherm (figure 2.3). A negative slope is related to a positive surface excess; therefore the molecule of interest accumulates at the surface. This is the typical behavior of all surface active molecules, especially of tensides. At a certain concentration the surface is fully packed by a monolayer and micelles begin to form (inlet of figure 2.3). After this point, denoted as critical micelle concentration (cmc), the surface coverage is constant. The behavior of tensides is well studied, first they occupy the surface and at full coverage micelles

or other structures form.

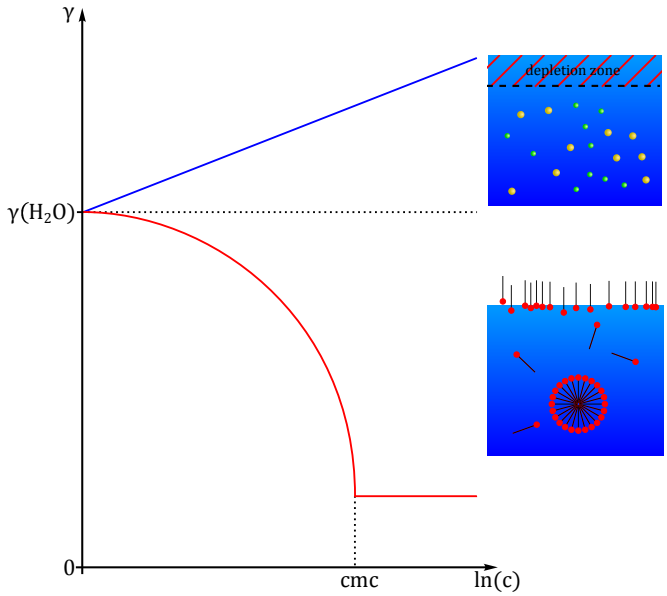

Figure 2.3.: Scheme of the surface tension isotherm of electrolytes (blue) and tensides (red). Inlets: Possible arrangements corresponding to the surface tension isotherm.

A positive slope is usually measured for electrolyte solutions, meaning that the overall concentration of the electrolyte is according to Gibbs smaller at the surface.[26] On the other hand, reaction kinetics of aerosol containing bromide ions required the propensity of ions towards the interface.[27] Some authors tend to overinterpret thermodynamic data. The surface excess is an integral quantity of the surface, with no layer resolution. It can accommodate any concentration profile that yields the very same surface excess (see figure 2.4).

2.2.3. Experimental Data and its Implications

Surface effects can dominate reactions, especially if the surface constitutes a large portion of the system, such as droplets.[28] This is especially true for processes taking place in the atmosphere. In kinetic studies of the reaction of brine droplets with ozone upon irradiation the measured surface chlorine concentration exceeded the expected value of classical models. Only with the assumption of a chloride enriched surface the results could be rationalized.[27]

The work of Hofmeister was the first investigation on ion specific effects in this context.[2,29–31] This series of papers is based on the behavior of proteins, however,

it opened a new field in soft matter chemistry which is still not thoroughly understood. Further investigations on proteins followed by other chemists, indicating a link between the anion and cation effect.[4] By now there is a zoo of effects known, some have even strong impact on our everyday life. Especially surface effects seem to be strongly affected by ion specific effects. In the following I will present some of the subsequent experiments.

In the recent years a non-monotonic concentration profile with an enriched and a depleted layer with an integral surface concentration lower than in the bulk was established (see right depiction in figure 2.4).[32] There are different surface propensities of anion and cations depending on the Hofmeister effects. Molecular dynamic (MD) simulations suggest an enhanced anion concentration at the surface, where strong ion specific effects occur.[33]

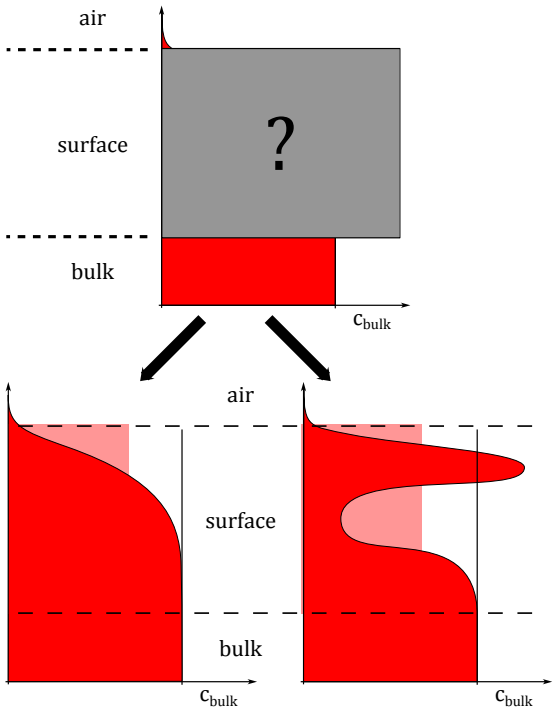

Figure 2.4.: Several surface profiles can lead fit the condition of an overall lower concentration at the surface. Two possibilities are shown here. Left: *Classical* picture of a depletion layer. Right: Non-monotonic concentration profile with an enhanced concentration followed by a depletion zone. The integral concentration in the surface area is in both cases equal (light red).

The surface enhanced concentration of electrolytes manifests not only in simulation data, but in many experiments as well. X-ray photoelectron spectroscopy (XPS) is a surface specific technique where the probing depth can be tuned by the

used photoelectron kinetic energies. For water the probing depth is in the range of 5 to 10 Å at energies of 100 to 200 eV.[34] Measurements of KBr and KI show a large enhancement of the halide over the cation, even more than MD simulations from Jungwirth predict for NaBr and NaI.[33,35] The derivations may stem from the different cation and especially from carbonaceous material at the surface in the experiment (a method for surface purification is described in section 3.3.4).[36]

Sum frequency generation spectroscopy (SFG, see section 3.1) is a surface specific spectroscopy. In most cases the water signature is used to gain information on ion pairing. The Allen group compared the SFG signal of sodium halides with bulk data obtained with Raman and ATR-FTIR measurements.[37] They attributed the two main resonances to less ordered (3450 cm^{-1}) and better ordered (3250 cm^{-1}) water.[38] The amplitude of the less ordered water was normalized by the amplitude of the water peak attributed to the stronger intermolecular coupling. This ratio increased in the order of H_2O<NaF<NaCl<NaBr<NaI in both measurements, bulk and surface. This was interpreted by a more chaotropic character of the latter anions. However, this effect is strongly amplified in the surface surrounding, indicating an enhanced anion specific effect at the interface.

In many SFG measurements only the water signature is measured. This is often difficult to interpret because no direct information on the ions themselves can be captured, but only the indirect effect on the interfacial water structure. There are only few simple molecules that can be investigated directly with SFG, due to the limited spectral range and the prevailing selection rules. In our measurements we carefully choose our probe molecules such that we can measure both, the water response and the resonances of the molecules itself, to gain a complete picture of the system. Furthermore, it is important to note that special care must be taken on the surface purity. Very often substances are used as received, however, surface active impurities accumulate at the surface and may alter the interface dramatically. This is even the case for solutions produced from high purity stock chemicals. In our investigations we used a specialized purification device, to remove in particular these impurities (see section 3.3.4), and verified prior to the measurement the successful purification by SFG spectroscopy.

In nature there are in most cases no pure surfaces, very often surfaces are covered with surface active material. In body cells, the same molecules can be found to form cell membranes, interacting in a specific way with different ions to enable a series of processes. There exist a variety of studies, in most cases performed on monolayers. There is a series of experiments monitoring the halide

behavior at lipid covered interfaces. Electron spray ionization mass spectroscopy was used to determine the surface behavior in droplets.[39] In these investigations a strong dependence of the anionic radius and of the energy of dehydration was found.

Cremer et al. found an impact of the counter ions on chain ordering by using SFG. They suggest that soft ions may penetrate ion membranes to be transported through.[40] Not only the chain itself is modified by the presence of ions. The water structure under PNIPAM was found to depend on the counter ions. This becomes evident in surface potential measurements.[41] The most common phospholipid in cells is DPPC (Dipalmitoylphosphatidylcholine). With a variety of methods, such as surface-pressure isotherms, Brewster angle microscopy (BAM), grazing incidence x-ray diffraction (GIXD) and infrared reflection absorption spectroscopy (IRRAS) a Hofmeister effect for anions could be observed.[42] With the nonlinear technique of second harmonic generation (SHG), an effect of anions and cations was found in a system of tetrabutylammonium iodide with added alkali halides.[43] The same method was used on the pure air electrolyte surface, here only an anion dependence could be measured.[44,45]

Wojciechowski et al. used total reflection X-Ray fluorescence (TRXF) to probe the surface profile of sodium halides at the air-water interface covered with the cationic lipid CTAB.[46] The resulting signals of the used anions are arranged in the order of the lyotropic series. Since TRXF is surface specific due to the short ranged evanescent field of X-ray radiation, this effect was interpreted in terms of different tendencies of building Stern layer depending on the individual anion species. Similar effects on anions were found from Leontidis et al. with grazing incidence X-ray diffraction (GIXD) and infrared reflection-adsorption spectroscopy (IRRAS) for a phospholipid monolayer.[42]

Cremer et al. used SFG (see section 3.1) to compare the interfacial water signal of sodium halides at the interface to quartz and $\mathbf{TiO_2}$.[47] In the case of the negative charged quartz, soft ions, such as $\mathbf{SCN^-}$ give a lower signal than e.g. the hard $\mathbf{Cl^-}$. When the solid surface is switched to the positive charged $\mathbf{TiO_2}$ this trend is reverse. This was interpreted such, that the z-position of the sodium changes due to charge changes, while the anions stay more or less in the same place. Therefore sodium is in one case in vicinity to $\mathbf{SCN^-}$ (quartz) and in the other to $\mathbf{Cl^-}$ ($\mathbf{TiO_2}$). This effect is known to reduce the water signal dramatically.[48]

The Allen group performed work on the cation Hofmeister effect.[49,50] For both,

chloride and nitrate, a strong cation dependence could be measured with phase sensitive SFG. A sign change in the imaginative spectra between the different cations indicates a change in the interfacial ion architecture.

A very elegant approach to measure the pairing of anionic surfactants with anions is to measure the size of the micelles in salt solution. Ion pairs are less hydrated than unhydrated headgroups. This leads to a smaller headgroup area and therefore to a higher packing parameter p. The packing parameter is directly correlated to the micelle size, and therefore is a bigger size of the micelle a measure for the formation of contact ion pairs. With this concept Vlachy et al. measured different combinations of anionic surfactants and simple cations.[51] Both, anions and cations, could be ordered in terms of the Hofmeister series.

To understand the experiments, computer simulations are often applied. Molecular dynamics (MD) is a versatile tool to predict surface profiles, however, the use of a realistic set of parameters is challenging. Further ambiguities are the result of the long range nature of electrostatic interactions, which in most cases cannot be fully covered with MD simulation.

2.3. Polarization and Dielectric Relaxation

The relative permittivity ε is the essential quantity to describe the interaction of an external electric field $\vec{E}$ with a dielectric media. At low intensities only first order terms are relevant (see also section 3.1). The electric field leads to a charge separation, known as polarization $\vec{P}$, which is basically a macroscopic dipole $\vec{M}$ moment per unit volume V (figure 2.5).

$$\vec{P} = \frac{\vec{M}}{V} \tag{2.8}$$

The polarization increases in a linear fashion with the electric field by the vacuum permittivity ε_0 and the electric susceptibility χ.

$$\vec{P} = \varepsilon_0 \chi \vec{E} \tag{2.9}$$

The polarization can be split in two components, the induced polarization $\vec{P_\alpha}$ and the orientational polarization $\vec{P_\mu}$, which operate on different timescales for relaxation. After turning off an external electric field, $\vec{P_\alpha}$ relaxes almost immediately, $\vec{P_\mu}$ decays over a timescale in the range of picoseconds to nanoseconds (see

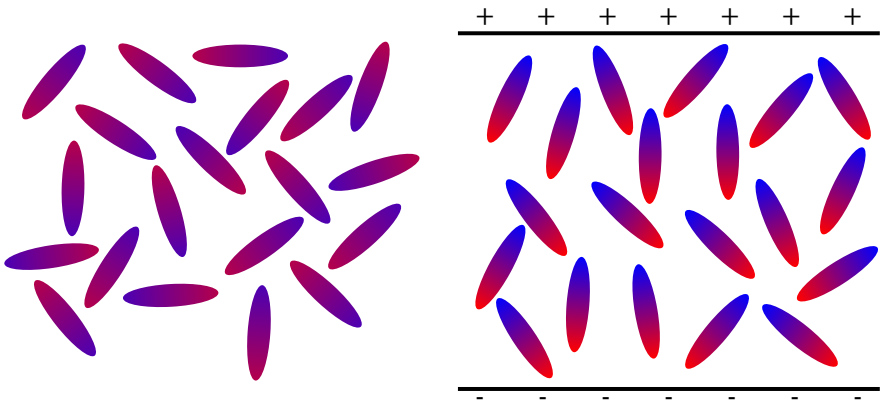

Figure 2.5.: Left: No external electric field is applied, the molecules are randomly oriented. Right: An external electric field is applied to the system. The overall orientation of the dipoles (corresponding to $\vec{P_\mu}$) and induced dipole strength (color-coded, $\vec{P_\alpha}$) is enhanced.

figure 2.6). These different decay times are the reason why the induced and the orientational polarizations can be treated as linearly independent.[52]

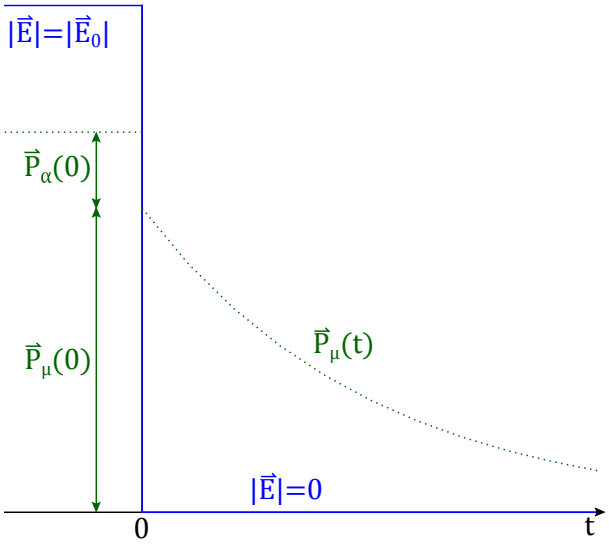

Figure 2.6.: Polarization depending on the external electric field $|\vec{E}|$. The induced dipole $\vec{P_\alpha}$ decays immediately, the dipolar polarization $\vec{P_\mu}$ needs some time.

2.4. Light and its Theories

2.4.1. Definitions

For the following sections a few terms commonly used for the description of light are introduced. Light is an electro-magnetic radiation, which can be described due to the wave-particle dualism as a wave and as a particle.[53] In most cases the description of the propagation is described in terms of the wave model while interaction with matter is most commonly described by the particle properties of light.

The electric field $\vec{E}$ and the magnetic field $\vec{B}$ are perpendicular to the propagation direction $\vec{k}$ (see figure 2.7). The force of the electric field on charge is proportional to the charge q (see equation 2.10); the magnetic field exerts force only on moving charges (equation 2.11).

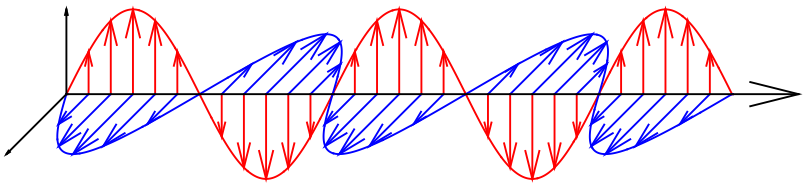

Figure 2.7.: The electric field (red) and the magnetic field (blue) are perpendicular to each other and to the propagation direction (black). The electric and magnetic field are maximal and minimal at the same time.

$$\vec{F}_{\mathrm{E}} = q \cdot \vec{E} \tag{2.10}$$

$$\vec{F}_{\mathrm{B}} = q \cdot \left(\vec{v} \times \vec{B}\right) \tag{2.11}$$

Since the speed of the charges $\vec{v}$ is negligible for all interactions covered in this work, only the force exerted by the electric field contributes.

Every polarization of a beam can be spit in the superposition of maximal two components. The simplest case is linear polarized light; here only one polarization is needed. More complicated is circular or elliptic polarized light, this can be described by two phase shifted components (figure 2.8).

When light hits a surface it may be reflected, refracted or both. In figure 2.9 the most important terms are shown graphically. A surface leads only to

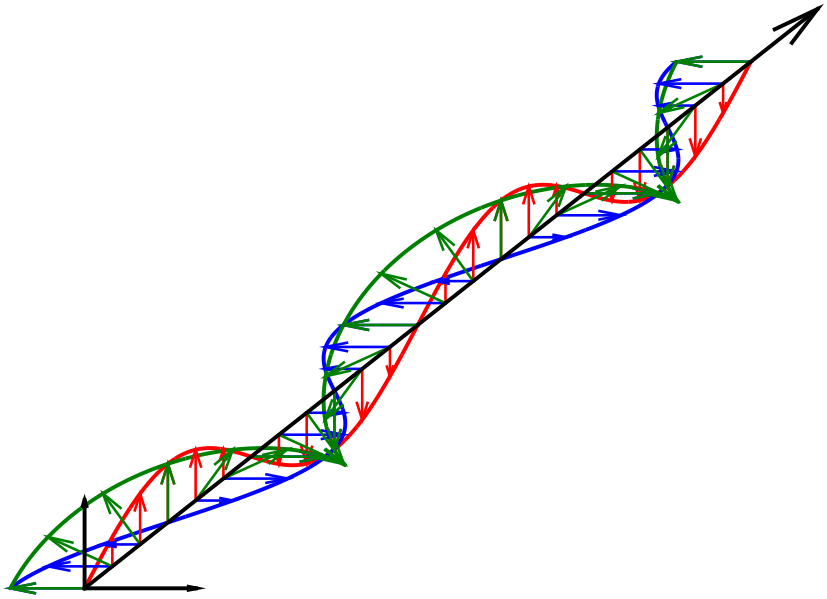

Figure 2.8.: The superposition of two phase-shifted linear polarized beams (the electric field is denoted with red and blue) results in circular polarized light (green).

refraction if the refractive indices n_1 and n_2 are different for the two media. The beam of incidence i and the surface normal n create the wave plane w, which is depicted in grey. Depending on the angle of incidence θ_i, which is in most cases defined as the angle between the surface normal and the beam of incidence, the light gets reflected (r) or transmitted (t). This and the relation to the refraction angle θ_t are covered in section 2.4.2. All polarizations of light can be split in two perpendicular components. For the behavior on surfaces it is convenient to orient the two components relative to the wave plane. Light with a polarization lying within the plane is called p-light, shown in figure 2.9 in orange. The perpendicular polarized light is called s-light from the German term *senkrecht* for perpendicular (figure 2.9, red). These two polarizations may behave quite different at the surface.

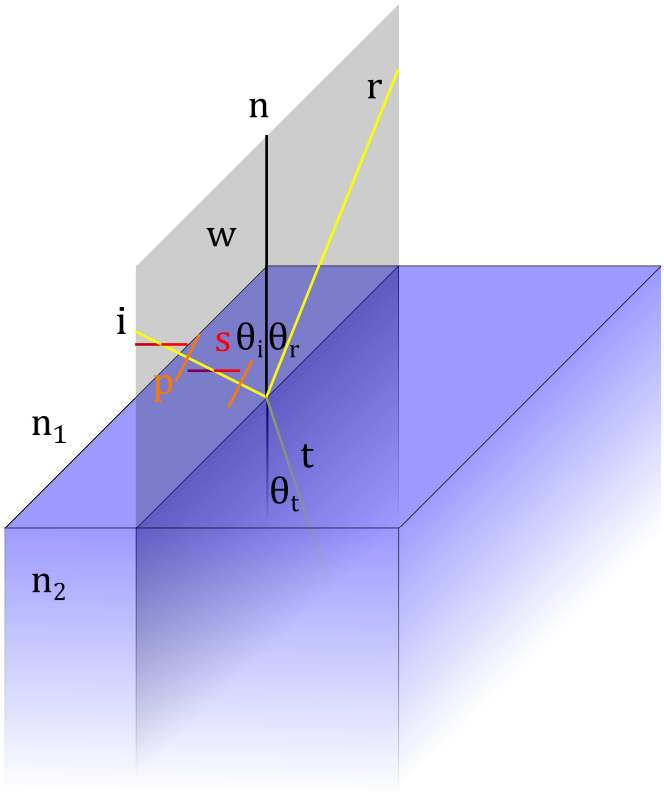

Figure 2.9.: Schematic sketch of the basic terms for light hitting a surface. Description of the sketch is given in the text.

2.4.2. Snell's Law

The Snell's law relates the refraction angle to the incidence angle of light. It is named after the Dutch astronomer Willebrord Snellius, however, the relationship was already described in the year 984 by the Persian mathematician Ibn Sahl.[54] It can be easily rationalized by finding the fastest way for light from a point in medium with the refractive index n_1 to another point in medium with the refractive index n_2. It turns out that there is a fixed relationship of the angle of incidence θ_i and the refractive angle θ_t depending on the refractive indices.

$$n_1 \sin\theta_\mathrm{i} = n_2 \sin\theta_\mathrm{t} \tag{2.12}$$

2.4.3. Brewster Angle

With Snell's law (eq. 2.12) and trigonometry the reflection coefficient can be transversed into functions with the angle of incidence as single variable. The

intensities are the square of the amplitudes r_s and r_p.

$$R_\mathrm{s} = |r_\mathrm{s}|^2 = \left| \frac{n_1 \cos\theta_\mathrm{i} - n_2 \sqrt{1 - \left(\frac{n_1}{n_2}\sin\theta_\mathrm{i}\right)^2}}{n_1 \cos\theta_\mathrm{i} + n_2 \sqrt{1 - \left(\frac{n_1}{n_2}\sin\theta_\mathrm{i}\right)^2}} \right|^2 \tag{2.13}$$

$$R_\mathrm{p} = |r_\mathrm{p}|^2 = \left| \frac{n_2 \cos\theta_\mathrm{i} - n_1 \sqrt{1 - \left(\frac{n_1}{n_2}\sin\theta_\mathrm{i}\right)^2}}{n_2 \cos\theta_\mathrm{i} + n_1 \sqrt{1 - \left(\frac{n_1}{n_2}\sin\theta_\mathrm{i}\right)^2}} \right|^2 \tag{2.14}$$

An example plot of the reflectivities as a function of the angle of incidence is shown in figure 2.10. It is easily seen that the reflectivity of s-polarized light increases, while the corresponding value of p-light goes through a minimum at the Brewster angle θ_B. The value of the Brewster angle depends on the refractive

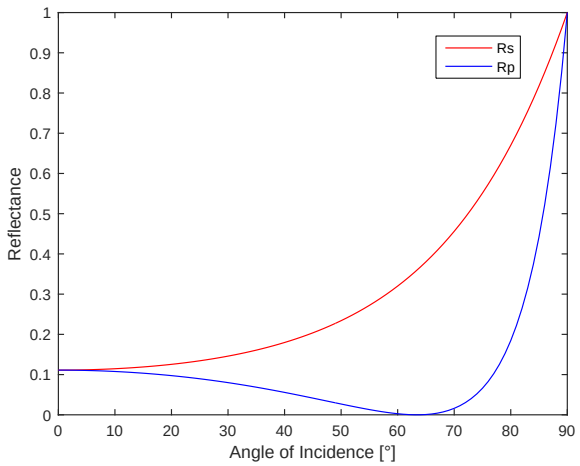

Figure 2.10.: Reflection coefficient of s- and p-light on the interface where the refractive index changes from $n_1 = 1$ to $n_2 = 2$.

indices of both media. At a certain angle the refracted beam is perpendicular to the reflected. For p-light this means that the direction of the electric field of the refracted beam points directly in the direction of the reflected beam. Since the electric field and the wave vector cannot be parallel to each other, this geometric arrangement leads to no intensity of the p-polarized reflected beam.

With the Snell law (eq. 2.12) the Brewster angle ($\theta_B = \theta_i$) can be calculated.

$$\theta_B = \tan^{-1} \frac{n_2}{n_1} \tag{2.15}$$

In the special case of the air-water interface the corresponding refracting indices of 1 for air and 1.33 for water result in a Brewster angle of 53°. At this angle no p-light is reflected at the air-water interface. This is the basis for the Brewster angle microscopy (see section 3.3.3), which is used to characterize surface layers.

2.4.4. Limit of Diffraction

The interface is the region where the change from bulk properties to gas properties occurs. The exact composition of this surface region is subject to discussion (see section 2.2). The actual geometrical dimension of this region depends strongly on the composition of the system.[37]

Surface specific methods are based on different mechanisms. Traditional spectroscopy measures always both, the bulk and the surface contribution. The spacial resolution achieved in spectroscopy can be adjusted by the focus and by many more parameter. The physicist Ernst Abbe showed that there is a limit of resolution d, depending on the wavelength λ of the irradiated light.

$$d = \frac{\lambda}{2n \sin \theta_i} \tag{2.16}$$

Other parameters are the refractive index of the light transmitting medium n. θ_i is half of the field angle of the objective. Since the light transmitting media is in most cases air with a refractive index close to 1, and the angle θ_i is between 0° and 90°, the best possible diffraction limit is $d = \frac{\lambda}{2}$. For visible light the diffraction limit is therefore in the range of hundreds of nanometer. Since the surface structure of the ions at air-electrolyte interfaces reaches only a few Ångström into the solution,[55] with standard spectroscopic method based on visible light the bulk contribution always outperforms the surface contribution. Therefore, with standard spectroscopy in the visible range no information on the surface can be gained.

One way to avoid this is the use of a total reflection setup. The resulting evanescent field decays exponentially with a linear dependence of the incoming wavelength. The decay length l depends on the refractive indices n_1 and n_2 and

on the angle of incidence θ.[56]

$$l = \frac{\lambda}{2\pi\sqrt{n_1^2 \cdot \sin^2\theta - n_2^2}},\ \theta > \theta_c \tag{2.17}$$

θ must be larger than the critical angle θ_c to guarantee total reflection.

However, the vertical resolution is again only for very short wavelengths sufficient small for surface investigations. Frequently used are X-rays with a wavelength of less than two nanometer. This makes it possible to investigate ion distributions at the interface. A similar resolution is possible with neutrons. The significant drawback of these powerful techniques is the great deal of technical effort required for these methods. High energies are needed, this is only possible at central facilities.

To make spectroscopy with visible light, other ways must be found to avoid the limit of diffraction. Second order nonlinear optical methods, namely SFG (section 3.1) and SHG (section 3.3.7), use a different approach. Here the probing depth is determined by the system, and not by the experimental setup. The special selection rules make it possible to probe only the few topmost layers of the interface (see sections 3.1.2 and 3.1.3).

3 Methods

To investigate exclusively the surface of soft matter is a difficult task. Methods based on force measurements, such as atomic force microscopy, are suitable to monitor the accumulation of matter at the surface, however, molecules covered by the surface are not easily accessible. Furthermore, this kind of methods is well suited for static systems, however, the molecule distribution at soft interfaces is a highly dynamic system which is very sensitive on external influences.

To avoid a destructing impact of the measurement method on the surface structure, optical methods are the method of choice. A big drawback of these methods is the diffraction limit (see section 2.4.4). In the linear regime, the only possibility to gain information on the surface is to compare the spectra of the probe with the same system without the molecule of interest. This approach is quite challenging, because the intensity difference is vanishing small.

A much more elegant way is the use of nonlinear optics. The great advantage is the intrinsic surface specificity, only molecules at and close to the interface contribute. The main method used in this thesis is Sum Frequency Generation (SFG) spectroscopy, which is based on the nonlinear response of the interface (see section 3.1). Although the device is rather complicated, the probe handling is comparably easy.

The bulk was investigated by the complementary Dielectric Relaxation Spectroscopy (DRS), which gives insight into the ion structure in the bulk. Furthermore, several additional techniques were used, either by performing experiments or by the comparison of already published data.

3.1. Sum Frequency Generation Spectroscopy

Sum Frequency Generation (SFG) spectroscopy is based on second order nonlinear effects. It is a sophisticated method to investigate the surface of soft matter. It is the main method used in this thesis. The principle of sum frequency generation is based on the nonlinear contributions of light at high intensities.

3.1.1. Theoretical Foundations of SFG

The electronic structure of molecules can be for low intensities described by a harmonic oscillator. In this regime the response on irradiation is at the same wavelength as the incoming light. When the intensity of the light is increased, the nonlinear response of the system occurs, which can be decomposed by Fourier decomposition in different components (see figure 3.1).

Upon interaction with matter in the nonlinear regime, optical rectification ($P(0)$) and terms with a higher frequency (e.g. $P^{(2)}(2\omega)$) arise. The intensities of these higher order terms decrease rapidly, the second order term is still rather well accessible, third or higher order contributions are very challenging to measure due to its low intensities. All higher order processes are not described by classical optics. They are many photon processes. The photons may stem from a single laser beam or from two or more laser beams. The most common two photon processes used for application are described briefly in the following (see figure 3.2).

The easiest way to understand this diagram is to take a closer look on the polarization of the nonlinear matter. The overall polarization is the sum of the different order of polarization, which depends on the susceptibility χ and on the electric field E.

$$\begin{aligned} P &= P^{(1)} + P^{(2)} + P^{(3)} + ... \\ &= \varepsilon_0 \left(\chi^{(1)} E + \chi^{(2)} EE + \chi^{(3)} EEE + ... \right) \end{aligned} \tag{3.1}$$

All the processes shown in the diagram are of second order, therefore we will take a closer look on this term. Lets assume for the electric field a plane wave with a frequency ω and an amplitude E_0. ε_0 denotes the vacuum permittivity and is a constant.

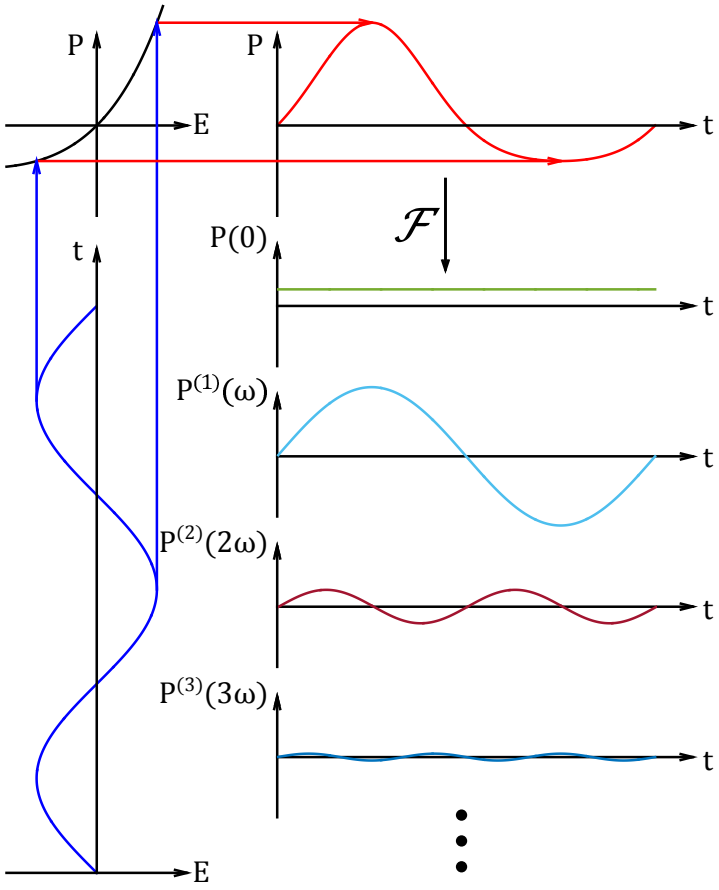

Figure 3.1.: A high intensity electromagnetic wave (blue) hits matter that that behaves in the intensity regime of the incoming light in a nonlinear fashion (black). The response is a nonlinear wave (red). It can be decomposed by a Fourier transformation into several contributions such as optical rectification (green) or double frequency (brown).

$$\begin{aligned} P^{(2)} &= \varepsilon_0 \chi^{(2)} E E \\ &= \varepsilon_0 \chi^{(2)} \left[E_0 \cos(\omega t)\right]^2 \\ &= \underbrace{\frac{1}{2}\varepsilon_0 \chi^{(2)} {E_0}^2}_{\text{optical rectification}} + \underbrace{\frac{1}{2}\varepsilon_0 \chi^{(2)} {E_0}^2 \cos(2\omega t)}_{\text{double frequency}} \end{aligned} \tag{3.2}$$

The double frequency term describes the SHG (Second Harmonic Generation) process. Only one laser beam is used. Additionally, optical rectification occurs, however, this is not experimentally used. In figure 3.1 SHG corresponds to $P^{(2)}(2\omega)$ and is the double frequency of the incoming beam. Therefore two photons of the same energy interact at the same time with the nonlinear matter

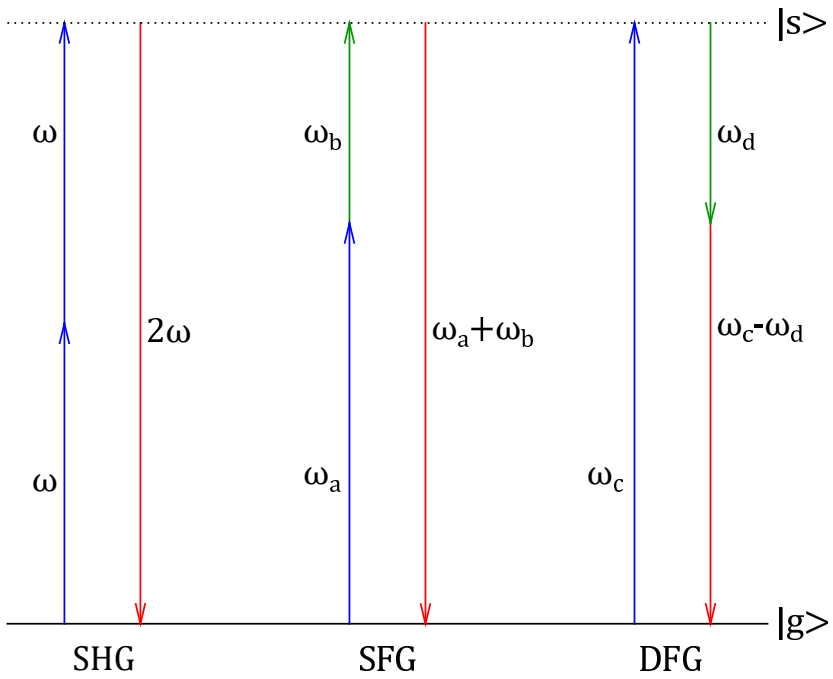

Figure 3.2.: Jablonski diagram for SHG, SFG and DFG. $|g>$ is the ground state $|s>$ denotes a virtual state. In between may be a resonance, than the signal is enhanced. For better clarity the energies of $|g>$ and $|s>$ is chosen to be equal for all cases in this picture.

and form one photon with the double energy. Often, SHG is used to investigate aromatic systems with a resonance in the UV range because in this case a visible light laser can be used (see section 3.3.7).

If two different wavelengths are used for the incoming beams, several different effects can occur additionally to the already mentioned ones. The incoming electric field can now be described by the sum of two planar waves.

$$E = E_{01}\cos(\omega_1 t) + E_{02}\cos(\omega_2 t) \tag{3.3}$$

When plugging equation 3.3 into equation 3.2 one obtains, additionally to the previous mentioned effects, the sum- and difference frequency of the two incoming wavelengths.

$$
\begin{aligned}
P^{(2)} &= \varepsilon_0 \chi^{(2)} EE \\
&= \varepsilon_0 \chi^{(2)} \left[E_{01} cos(\omega_1 t) + E_{02} cos(\omega_2 t)\right]^2 \\
&= \varepsilon_0 \chi^{(2)} \Bigg[\overbrace{\frac{1}{2}{E_{01}}^2 + \frac{1}{2}{E_{02}}^2}^{\text{optical rectification}} + \overbrace{\frac{1}{2}{E_{01}}^2 cos(2\omega_1 t) + \frac{1}{2}{E_{02}}^2 cos(2\omega_2 t)}^{\text{double frequency}} \\
&\qquad + \underbrace{E_{01}E_{02} cos((\omega_1 + \omega_2)t)}_{\text{sum frequency}} + \underbrace{E_{01}E_{02} cos((\omega_1 - \omega_2)t)}_{\text{difference frequency}} \Bigg]
\end{aligned}
\tag{3.4}
$$

In this equation all processes shown in the Jablonski diagram (figure 3.2) are covered. DFG (Difference Frequency Generation) is basically very similar to the optical rectification ($P(0)$), with the difference that two different incoming lasing frequencies are used. Therefore the resulting frequency is not zero but the difference of the two incoming frequencies.

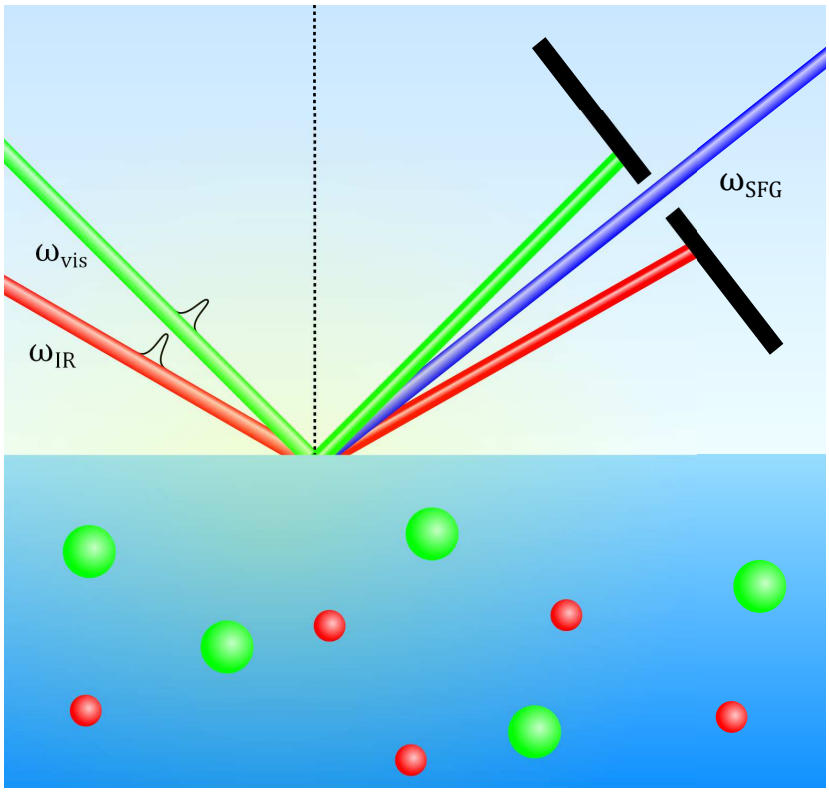

Figure 3.3.: Schematic sketch of the SFG setup. Two laser beams, a visible one at 532 nm (ω_{vis}) and a tunable in the infrared range (ω_{IR}) hit the surface with temporal and spacial overlap. Among other contribution the sum frequency (ω_{SFG}) is formed.

SFG is similar to SHG (see section 3.3.7), but with two incoming frequencies. This is the spectroscopic method used for investigations in this work. Two laser beams, usually one tunable wavelength and one with a fixed wavelength hit the surface with spacial and temporal overlap. The temporal overlap is of course obsolete for continuous wave (cw) lasing systems, however, these systems are usually not used for this application. The great advantage of pulsed systems is the high energy used for spectroscopy, which can dissipate before the next pulse excites the system again. The schematic setup is shown in figure 3.3. A fixed visible beam and a tunable infrared beam hit the surface. Due to nonlinear effects, additionally to the incoming beams, higher order beams are generated, among them the sum frequency beam. With the assistance of notch filter and screens only the SFG-contribution reaches the detector.

3.1.2. Selection Rules of SFG

SFG is – as already mentioned – a surface specific technique. Only non-centrosymmetric matter gives rise to a second order nonlinear signal. No matter where this condition occurs a signal will be measured. An isotropic distributed liquid moving according to the Brownian motion has no preferential orientation. This is not a result from a certain setup, but an inherent feature of this technique. SFG is a two photon process. The intensity of the SFG-signal I_{SFG} is proportional to the intensities of the two incoming beams I_{vis} and I_{IR} and to the square of the nonlinear susceptibility $\chi^{(2)}$.

$$I_{\mathrm{SFG}} \propto I_{\mathrm{vis}} I_{\mathrm{IR}} \left(\chi^{(2)}\right)^2 \tag{3.5}$$

The nonlinear susceptibility is the link between the macroscopic observable intensity and the microscopic hyperpolarizability. It is material dependent and can be rewritten in terms of the oriental average of the hyperpolarizability $< \beta_{\alpha\beta\gamma} >$.

$$\chi^{(2)} = N < \beta_{\alpha\beta\gamma} > \tag{3.6}$$

N is the number density. $< \beta_{\alpha\beta\gamma} >$ is a microscopic quantity which is proportional to the IR- and Raman-transition dipole moments.[57]

$$\beta_{\alpha\beta\gamma} = \frac{1}{2\hbar} \frac{M_{\alpha\beta} A_{\gamma}}{(\omega_{\mathrm{vis}} - \omega_{\mathrm{IR}} - i\Gamma)} \tag{3.7}$$

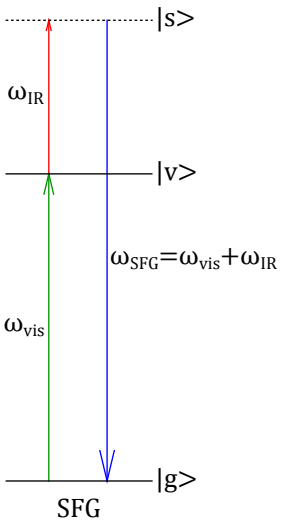

Figure 3.4.: Jablonski diagram of a SFG-transition. Visible (green) and infrared (red) light hit the nonlinear medium and the sum frequency is generated (blue). The ground state is denoted as $|g>$, in the resonance case $|v>$ is the excited state, otherwise both, $|v>$ and $|s>$, are virtual states.

$M_{\alpha\beta}$ and A_γ are the corresponding Raman and IR transition dipole moments.

$$M_{\alpha\beta} = \sum_s \left[\frac{< g|\mu_\alpha|s >< s|\mu_\beta|v >}{\hbar\left(\omega_{\mathrm{SFG}} - \omega\right)} - \frac{< g|\mu_\beta|s >< s|\mu_\alpha|v >}{\hbar\left(\omega_{\mathrm{vis}} - \omega\right)} \right] \tag{3.8}$$

$$A_\gamma =< v|\mu_\gamma|g > \tag{3.9}$$

When plugging equations 3.6 and 3.7 into equation 3.5, it becomes clear that only transitions are allowed which are simultaneously IR- and Raman-active. This can be only accomplished if the material is not centro-symmetric. This can be rationalized by a thought experiment. Lets go back to equation 3.4. The polarization of matter is proportional to the two incoming electric fields and the second order susceptibility. ε_0 is a constant. Solving the equation system reveals that the only solution is no polarization at all and therefore no signal.

$$\begin{aligned} \vec{P}^{(2)} &\propto \chi^{(2)}\vec{E}\vec{E} \\ &\Downarrow i \\ -\vec{P}^{(2)} &\propto \chi^{(2)}(-\vec{E})(-\vec{E}) = \chi^{(2)}\vec{E}\vec{E} \\ &\Downarrow \\ -\vec{P}^{(2)} &= +\vec{P}^{(2)} \\ &\Downarrow \\ \chi^{(2)} &= 0 \end{aligned} \tag{3.10}$$

This simple consideration is the reason why SFG is a surface specific technique. When taking a look on the structure of a soft bulk matter, one realizes that the structure is overall centrosymmetric. The molecules are statistically distributed with no preferential orientation. Soft matter is - other than crystals - isotropic in all directions of space. This means that no second-order nonlinear process is possible. Only at the interface the isotropic distribution is broken. The ions have a preferential orientation and there is no more an inversion symmetric counterpart for each molecule. Therefore, in this region $\chi^{(2)}$ is not any more zero, and there is a SFG contribution. The depth of this contribution is not easily distinguishable, because it strongly depends on the system. A surface covered with a charged lipid will have better and larger ranged net orientation than the pure air-water interface. This is the large difference of the surface specificity of nonlinear optical techniques compared to other surface specific optical techniques. The investigated depth is not dependent on the diffraction limit but only on the interfacial structure. This makes it possible to work with visible light with a vertical resolution in the range of a few molecule layers.[43] It is very hard to estimate the exact depth resolution, especially since there is a fluent transition from the partially ordered surface to the isotropic bulk.

3.1.3. Signal Intensity

The SFG signal is given by the integral of the orientational distribution function from one bulk phase over the interface to the adjacent bulk phase. This depends on several factors. As discussed previously, molecules adopt a preferential orientation at the interface, which is the basis for the SFG signal. The resulting signal depends on three parameters: 1. The intensity of the signal, a high intensity resonance gives a stronger signal. 2. The number of orientated molecules

is proportional to the intensity, because more molecules contribute to the signal. 3. The better the molecules are orientated, the higher the resulting signal will be. The first parameter is specific for the species, but when the same species is probed in different surroundings, then the intensity is only a function of the two latter parameters.

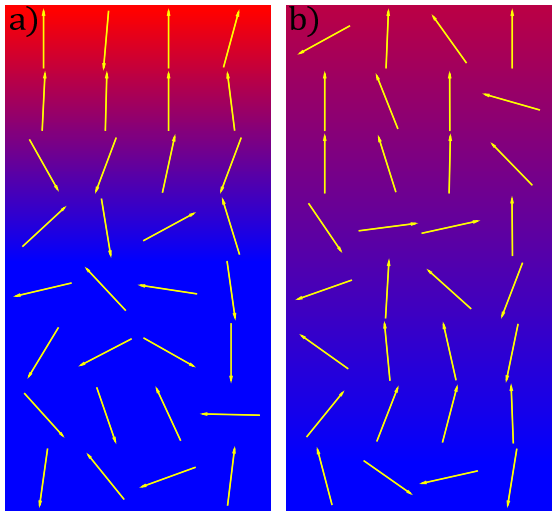

Figure 3.5.: Possible arrangement of molecules at the surface.

The SFG signal cannot be resolved to a certain probing depth without further information. A well oriented system in the first few molecule layers may give the same signal as a less well but deeper reaching oriented system. This is schematically shown in figure 3.5, where in a) the first few layers are well aligned, but the subsequent layers loose the net orientation very fast. In b) the net orientation is less, but the resulting signal is still in the same range, because the alignment reaches further down. The depth of oriented molecules can be attributed to the probing depth and may vary strongly. For example the positions of counterions have a large impact on the orientational depth. Many experiments and simulations have shown the impact of the ions on the interfacial depth.[32]

3.1.4. Spectral Regions

Very often SFG is performed on air water interfaces. The water may contain ions or other solutes. The surface may be covered by surface active compounds, such as lipids. In this scenario the information extracted from the system by SFG can be split in two groups, the water resonances and resonances from the

other molecules in the system. All resonances can be investigated in terms of the position and the amplitude. The position contains information about the chemical environment and the amplitude - especially the ratio of amplitudes - can be examined on the order of the structure.

Molecule Resonances

The resonances of the molecules can be used to learn more about the arrangement of the molecule itself. The great drawback is that not all molecules have accessible resonances. If there are resonances in the spectral range, the SFG signal gives information on the presence of the molecule at the interface. Additionally, structural information, such as the distortion from a center symmetric symmetry, can be obtained from the data.

Special role play molecules with hydrocarbon chains. The resonances of C-H vibrations are in the range of 2700 - 3000 cm^{-1},[58] and of the deuterated C-D-species at 2000 - 2300 cm^{-1}.[59] In table 3.1 the CH_2 and CH_3 resonances are shown. Both ranges are easily accessible with the SFG setup.

Group	Mode	in air	in water
		wavenumber [cm^{-1}]	
CH_2	Symmetric stretch	2854	2846
CH_3	Symmetric stretch	2878	2874
CH_2	Fermi resonance	2890-2930	2890-2930
CH_2	Anti-symmetric stretch	2915	2916
CH_3	Fermi resonance	2942	2933
CH_3	Anti-symmetric stretch	2966	2962

Table 3.1.: Alkyl resonances of SFG in air and in water.[58]

These oscillations carry a large amount of information. Especially the structural arrangement can be easily monitored, because in an all-*trans*-conformation there are local centers of inversion present (see figure 3.6), and the CH_2-groups do not contribute to the signal. In a less ordered chain with *gauche*-effects, this symmetry is broken and a signal for the CH_2-groups can be obtained.[58] Therefore the intensity changes of the CH_2-groups can be used to obtain information on order of the hydro-carbon chains. The CH_3 groups, on the other hand, cannot cancel due to symmetry reasons. Its intensity is mainly determined by the packing density and can be taken as a rough measure of the surface concentration.

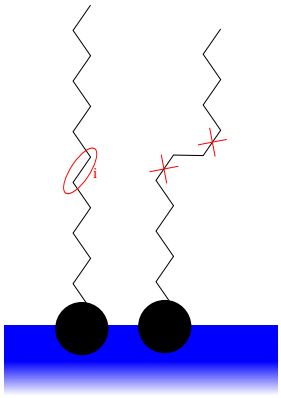

Figure 3.6.: Left: *all-trans* chain, the CH_2 groups are locally inversion symmetric and contribute therefore not to the signal. Right: Symmetry is broken due to *gauche* effects.

With standard SFG measurements no absolute values are obtained, because due to adjustment and external effects, such as humidity and temperature at the lasing system, the intensity may vary between the measurements. Therefore, we introduced the disorder parameter, which is the ratio of the amplitude of the symmetric CH_2-stretch-mode to the amplitude of the symmetric CH_3-stretch-mode. The lower this value, the better ordered are the chains.

For the determination of the structure of the mixture of different lipids, one of the structures can be deuterated. The resonances of the deuterated species shift to about 2000 - 2300 cm^{-1}, which is well separated from the CH-modes. With this it is possible to gain information on the structure of each individual of lipid-mixtures.

Water Modes

One major advantage of SFG for the investigation of the air water interface is the possibility to monitor the water structure. A SFG spectrum of pure water exhibits three peaks. Two very broad peaks, at roughly 3200 cm^{-1} and 3400 cm^{-1}, and a sharp feature at 3700 cm^{-1}. The latter one can be attributed to dangling OH bonds, which is unique to the surface.[38] This peak only occurs at clean surfaces, as soon as the surface is covered by a surface active substance this peak disappears. The two broad band peaks are in the spectral resonance region of ice (3200 cm^{-1}) and of water (3400 cm^{-1}), this is why they are often designated as *ice-like* peak and *water-like* peak.[60] The exact interpretation of the origin of these two peaks is still under discussion, but they may suggest a distance and angle

distribution similar to bulk water or ice respectively. In many cases the exact assignment of the peaks is not requisite, the knowledge that both peaks stem from the water is enough to make statements about the interfacial water architecture. A high signal indicates well oriented interfacial water. This might be the case for separated charges. A low water signal indicates the centrosymmetry of interfacial water.

3.1.5. Technical Description of the Device

To implement SFG measurements there are two common setups. The traditional setup uses a picosecond pulsed laser scanning each frequency separately. In the recent years many groups started to work with a femtosecond broadband laser, where a broad frequency range is covered by a single pulse. Both methods have advantages and disadvantages.

The way of taking spectra is completely different for these two methods. The ultra short pulses in the femtosecond regime lead to broadening of the frequency range.

$$\Delta\omega = \frac{2\pi K_{\mathrm{TB}}}{\tau} \tag{3.11}$$

The angular frequency ω is broadened, depending on the pulse duration τ and on a form factor of the pulse K_{TB}. The form factor equals 0.443 for a rectangular pulse and 0.142 for a Lorentian pulse. Other standard pulse shapes are in between.[61] Lets assume a 10 fs Lorentian pulse. Plugging in the numbers and converting to the more convenient wave numbers, one gets a broadening of $\Delta\bar{\nu} \approx 474\ \mathrm{cm}^{-1}$. This means that with a single pulse a much larger frequency range can be measured. This involves higher requirements on the detector. As a result a much faster measuring time can be achieved. Major drawbacks of this method are the high technical requirements, very high noise levels at the outer frequency range and the unwanted heating of the probe due to the strong excitation of single strong resonances. The latter may prevent the measurement of weak signals close to strong resonances.

The more traditional method uses picosecond pulses. This method was used for the investigations presented in this work. The greatest drawback of this method is the time-consuming measurement process, on the other hand the resulting spectra are of very good quality. The basic setup is rather simple, the technical realization somewhat challenging. Two pulsed laser beams are focused on the

probe, one fixed visible beam and a tunable infrared beam. The resulting sum frequency signal gets filtered and hits a monochromator.

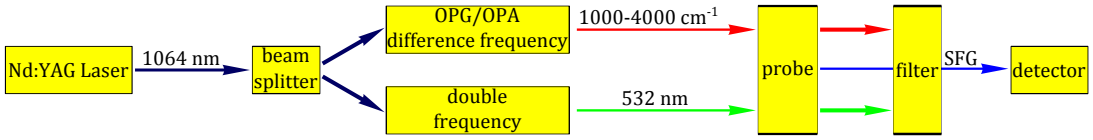

Figure 3.7.: Components of the SFG lasing system.

In figure 3.7 all important components are schematically shown. Light from the Nd:YAG laser unit is converted in green light and a tunable IR laser beam. Both beams hit simultaneously the probe, the reflected incoming beams are filtered and only the sum frequency intensity is measured in the detection unit. The function and setup of the single components are described in the following.

Nd:YAG Laser

Lasers are based on the population inversion. This is only possible in systems with more than two states. The active media of the used solid state laser is neodymium-doped yttrium aluminum garnet, or as chemical formula written Nd:$Y_3Al_5O_{12}$. It was first developed in 1964 by Geusic et al. in the Bell laboratory and is now one of the most common laser types used.[62] It is based on an energy state system as shown in figure 3.8. From the ground state the photons are pumped by a flashlight in the pump levels. From these excited states $^4F_{3/2}$ becomes populated by fast decays. The slow decay to $^4I_{11/2}$ and the fast decay of the lower level to the ground state lead to a population inversion as it is required for the stimulated emission. Without a resonator the 1064 nm wave is spontaneously emitted in all spacial directions. A resonator matched with the wavelength enhances the signal by mode locking. A Fabri-Perot etalon narrows the spectral width of the pulses with frequency dependent losses. To shorten the pulses a dye absorbs part of the pulses. In the resonator a series of pulses oscillate, called a train. A stable pulse is selected and decoupled from the primary resonator by a Pockels cells rotating the polarization of the pulse. This pulse passes twice through the amplifier, where it is enhanced. This infrared laser beam can now be used for further manipulation.

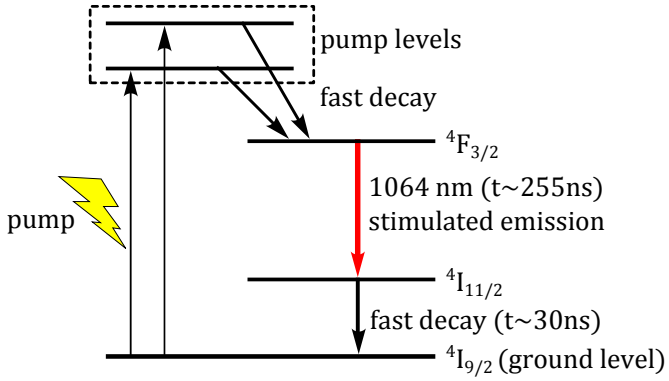

Figure 3.8.: Energy states of Nd:YAG laser.

Harmonics Generator

From the fundamental infrared beam of the Nd:YAG laser both is generated, the fixed visible and the tunable infrared beam. First of all the beam is split into two, one fraction is used later for the tunable infrared beam. The other fraction passes trough a nonlinear crystal along a unique axis. Due to nonlinear effects the second and third order harmonics are generated at two optical active crystals. The green second order beam (532 nm) is used directly for the spectroscopy. The ultra violet third harmonic beam (355 nm) undergoes further manipulation in the OPG/OPA unit.

OPG/OPA

One of the largest challenges of the setup is the generation of a laser beam with a tunable frequency. This task is resolved by a nonlinear optical mechanism based on parametric scattering. One photon is split into two, obeying the laws of momentum and energy conservation (see figure 3.9).

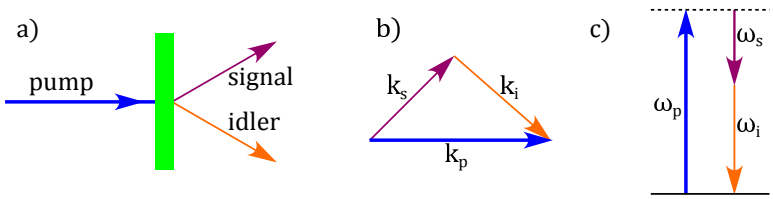

Figure 3.9.: a) The pump beam hits the nonlinear crystal and splits to a signal and an idler beam. b) The momentum conservation determines the direction of the two new beams. c) Due to energy conservation the sum of the outgoing frequencies must be equal to the pump frequency.

The resulting frequencies depend on several parameters, e.g. the temperature or the tilt angle of the crystal.[63] To obtain control, the crystal is thermostated, the only parameter changed is the angle. By changing the angle of the crystal, the desired frequency is generated by the pump beam. Since the desired frequencies are in the visible range, for the pump frequency the ultra violet beam from the harmonics generator is used. This process is called optical parametric generation (OPG).

The resulting visible beam has a low intensity and is rather broadband. First, the bandwidth is reduced by a monochromator, with a grating as the central component. To enhance this signal the process of optical parametric amplification (OPA) is applied. This process is also called difference frequency generation, because the difference frequency is a side product of this process. The pump and the idler beam travel colinearely through the optical active crystal. Upon phase matching the energy of the pump beam will amplify the idler and an additional beam with the frequency $\omega_2 = \omega_\mathrm{p} - \omega_\mathrm{i}$ is generated.

The tunable beam is so far only of limited use for molecule spectroscopy, because the available spectral region lies at higher energies than most resonances of interest. The adjustment to wavenumbers in the range of 1000 - 4000 cm^{-1} is done by taking the difference frequency with a previously separated fundamental beam.

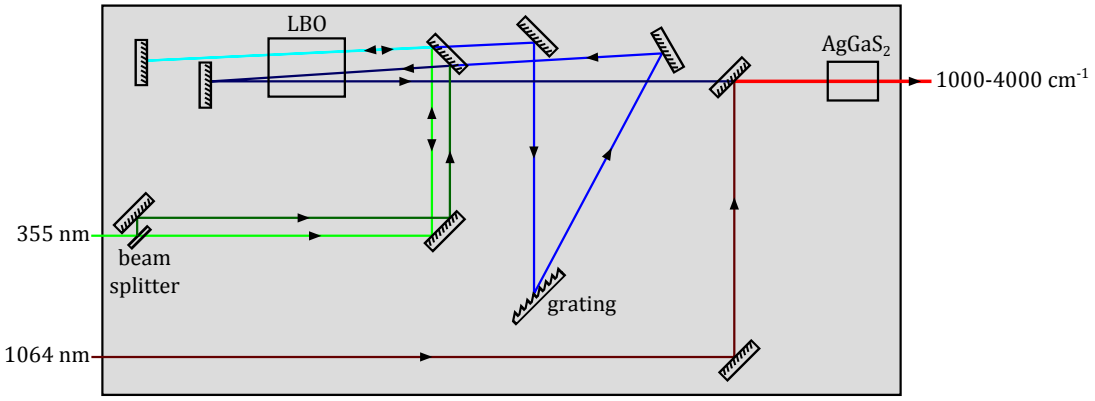

Figure 3.10.: This simplified beam path shows all processes in OPG/OPA unit. For clarity all delay lines, lenses, energy dumps and so on are left out. The single processes are color coded and described in the text.

In figure 3.10 all processes in the OPG/OPA unit are displayed in a schematic beam path. The 355 nm beam (light green) is guided to the lithium borate oxide (LBO) crystal, where in the OPG process (turquoise) takes place. The bandwidth

of this altered beam is narrowed in the monochromator with a grating as central component (blue). This weak signal is enhanced by an OPA process (dark blue), for this the previously separated *fresh* 355 nm beam (dark green) passes the LBO crystal simultaneously with the beam from the monochromator. This process is important for an uniform energy distribution of the laser cross section. From the resulting narrowband intense signal the difference frequency with the 1064 nm beam (brown) is gained by a silver gallium sulfide crystal ($AgGaS_2$) which is used as the final tunable infrared beam (red). In order for this process to work it is indispensable that the pulses overlap in the nonlinear optical crystals. This is only possible by adjusting the beam paths to the same length by adding delay lines (this is not shown in the figure for clarity reasons).

Probe

After all the manipulations on the laser beam described above, two pulsed beams are obtained. One visible beam at 532 nm and an infrared beam tunable from 1000 cm^{-1} to 4000 cm^{-1}. These two laser pulses are brought to temporal and spacial overlap at the surface of the probe. Here due to nonlinear effects, among others a sum frequency beam emerges (see section 3.1 and figure 3.3).

Detector

To avoid too high intensities at the detector, a notch filter removes most irradiation that does not stem from the SFG signal. As a detecting unit a monochromator is applied (see figure 3.11). With the monochromator only the desired wavelength is measured by adjusting the angle of a grating.

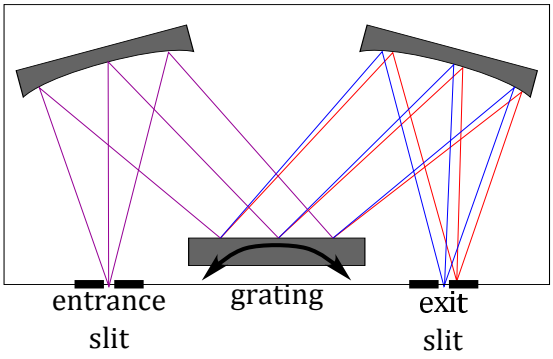

Figure 3.11.: Schematic sketch of the function of a monochromator.

Instrumentation

The entire used lasing setup was provided by the Lithuanian manufacture EKSPLA. The lasing unit PL2143 and the harmonic generation unit PG401 are mounted on an optical table RS4000TM by Newport. The detecting unit is the monochromator SP-2150i from Princeton Instruments.

3.1.6. Probe Preparation

To obtain reliable measurements several aspects must be respected. SFG is a very sensitive surface spectroscopy. At the surface the concentration distribution of molecules is very different to the bulk. This means that probes which are made from a bulk liquid need specific attention. Substances, which are according to standard criteria 99.999 % pure may show strong interfering signals at the surface (see section 3.3.4). Especially surface active substances, such as most carbon hydrates, accumulate at the surface and lead to a completely different surface architecture. To make sure that the surface contains only the wanted probe and no contamination the solution and all glassware must undergo a specialized purification mechanism.

All containers, which are in direct contact to a probe must be thoroughly cleaned. Since organic material demonstrates the peculiarity that it rather sticks to any surface than to be washed away, we used Caro's acid ($\mathbf{H_2SO_5}$), also known as *piranha solution*. It must be fresh prepared on a regular basis by mixing three parts of concentrated sulfuric acid ($\mathbf{H_2SO_4}$) with one part hydrogen peroxide ($\mathbf{H_2O_2}$). The acid decomposes and forms radical oxygen, which acts as an extremely strong oxidizing agent and destroys almost all organic structures. A nice side effect of this acid is the hydroxylation of most surfaces. This makes the surface very hydrophilic and therefore avoids the new agglomeration of organic material. A severe drawback of this acid is high risk evolving from the acid, because it is highly explosive, especially when adding organic solvents such as acetone.

Additional to the containers the solution itself must be cleaned. Bulk impurities in very low concentrations may accumulate at the surface and disturb the entire surface specific measurement. For this need we used for all stock solutions the Lunkenheimer purification device (see section 3.3.4). Only after verifying the successful expurgation with a SFG measurement of the hydrocarbon signals, the

stock solutions were diluted. These probes were reevaluated with SFG before using it for measurements.

In some parts we used a Langmuir film instead of a pure liquid. In this case the setup of the probe is different. A bulk liquid is filled in a Langmuir trough and a water insoluble amphiphile is dripped as chloroform solution on the surface. After evaporation of the chloroform a single molecular Langmuir film has formed which can be manipulated by the Langmuir trough (more information in section 3.3.2). In this case we have to deal with two sources of impurities. First of all the bulk liquid. In many cases this is water. We used for all solutions ultrapure water. The water is checked during sampling for its electric conductivity as measure for its purity. Furthermore we monitored the water spectra periodically with SFG. In the case a solution was used as a bulk phase we used the purification process already described. The amphiphile is far less critical, because as Langmuir film it does not split into bulk and surface phase. Therefore the bulk impurities distribute equally over the surface, but they are not subject to enrichment.

3.1.7. Measuring Routine

After the probe is prepared, it is ready for SFG measurements. The two laser beams are focused on the surface and the level is adjusted. The intensities of the two incoming beams are measured before they hit the probe. Since the intensities of the incoming beams are subject to variation (especially the infrared beam due to different wavelengths) we normalized every spectra by division of the raw data intensity with the two laser beam intensities according to formula 3.5.

We adjust the two laser beams on a sample with a strong resonance in the spectral regime of interest to ensure the highest signal possible, but this is a very fragile construct. Therefore, this routine must be repeated on a regular basis, taking human deficiencies into account. This is not covered by the normalization. Therefore, we compared only absolute intensities of the same adjustment. Relative intensities are not affected by the laser beam overlap, because the intensities upon a bad alignment are reduced over the entire spectra with no respect to the wavelength. This is the reason why we can use relative intensities to compare probes measured at different times.

To minimize evaporation throughout the measurement we covered the probe letting only a slit open for the light beams. Still, throughout the measurement the level of the probe must be readjusted.

Since the signal is very noisy we averaged in all measurements over at least 200 laser shots for every single point. In some cases with a very weak signal even over 500 laser shots per wavenumber are used.

3.1.8. Fitting Mechanism

Although we averaged over several measurements (see section 3.1.7), the resulting signal is still very noisy. Only very strong resonances have a lower variance. This is the reason why the fitting is an important factor for the interpretation of the data. We used as a fit function the Voigt profile. This function incorporates simultaneously a Gaussian and a Lorentian distribution by convolution of them.

$$V(x) = (G * L)(x) = \int G(\tau)L(x-\tau)\mathrm{d}\tau \tag{3.12}$$

The Gauss and the Lorentz function are defined as follows:

$$G(x) = \frac{1}{\sigma\sqrt{2\pi}} \exp\left(-\frac{x^2}{2\sigma^2}\right) \tag{3.13}$$

$$L(x) = \frac{\Gamma}{\pi\left(x^2+\Gamma^2\right)} \tag{3.14}$$

σ denotes the standard deviation and Γ the full width at half maximum (FWHM).

To avoid unphysical fits, we fitted in all cases either concentration sequences or sequences of similar structure. We were particularly vigilant about a monotonic change in all fit parameters. By this we could extract the most likely structure, although this may not be the best fit of each individual spectrum.

3.2. Dielectric Relaxation Spectroscopy

Dielectric Relaxation Spectroscopy (DRS) is a highly specialized technique to monitor the relaxation times of structures in soft matter. Other than SFG no information on the surface can be gathered, DRS purely measures bulk properties. This method was used in section 4 as a complementary method to SFG for the investigation of the bulk structure in terms of ion pairing. DRS measures the interaction of the sample with an oscillating electric field. The response can be either measured in the time domain or as a function of the field frequency ν. The latter is used, because here the response $\hat{\eta}(\nu)$ can be expressed by the complex permittivity $\hat{\varepsilon}(\nu)$ and the dc electric conductivity κ.

$$\hat{\eta}(\nu) = \hat{\varepsilon}(\nu) - i\frac{\kappa}{2\pi\nu\varepsilon_0} \tag{3.15}$$

ε_0 is the permittivity of free space. The complex permittivity can be split in a real and in an imaginary part.

$$\hat{\varepsilon}(\nu) = \varepsilon'(\nu) - i\varepsilon''(\nu) \tag{3.16}$$

The relative permittivity $\varepsilon'(\nu)$ is the in phase response. At very low frequencies, the system is able to follow the external electric field and the value at this condition is the static permittivity ε. At very high frequencies, only intramolecular processes are possible, all intermolecular processes are too slow and do not contribute any more. The plateau of $\varepsilon'(\nu)$ at this condition is by definition the infinite frequency limit ε_∞. In some cases the intra- and intermolecular timescales are not well separated, which makes it difficult to determine the infinite frequency limit. At intermediate frequencies the electromagnetic radiation is absorbed by the sample. This out-of-phase response is described by the dielectric loss $\varepsilon''(\nu)$. Through the Kramers-Kronig relation these two quantities are interchangeable, however, in order to avoid systematic errors, both quantities are fitted at the same time by the same appropriate relaxation model.[64]

Dielectric peaks are very broad. To be able to interpret the data therefore a very large frequency range must be covered, typically in the range of 1-30 THz. This is not possible by a single device, several devices must be used to produce a single spectrum.[65] The identification of the broad peaks are the major difficulty for the interpretation of dielectric spectra. In electrolytes, both, solute

and solvent, contribute via dipole reorientations and vibrations to the total signal, often with similar frequencies and magnitudes. The best fit does not guarantee that it is physical meaningful, because often an unambiguous assignment is not possible.[66] The signal can be decomposed into n band-shape functions $\widetilde{F}_\mathrm{i}(\nu)$ with amplitude S_i.

$$\hat{\varepsilon}(\nu) = \varepsilon_\infty + \sum_{i=1}^{n} S_\mathrm{i}\widetilde{F}_\mathrm{i}(\nu) \tag{3.17}$$

The band shape function can be modeled with the Havriliak-Negami equation or with simplified versions of it (see table 3.2). Each mode i has a certain relaxation time τ_i. α_i and β_i, which both take values between zero and one, are shape parameters.

Model	**Shape Parameters**	**Function**
Havriliak-Negami (HN)	$0 \leq \alpha_\mathrm{i} < 1 \quad ; \quad 0 < \beta_\mathrm{i} \leq 1$	$\widetilde{F}_\mathrm{i}(\nu) = \left[1 - (i2\pi\nu\tau_\mathrm{i})^{1-\alpha_\mathrm{i}}\right]^{-\beta_\mathrm{i}}$
Debye (D)	$\alpha_\mathrm{i} = 0 \quad ; \quad \beta_\mathrm{i} = 1$	$\widetilde{F}_\mathrm{i}(\nu) = \left[1 - i2\pi\nu\tau_\mathrm{i}\right]^{-1}$
Cole-Davidson (CD)	$\alpha_\mathrm{i} = 0 \quad ; \quad 0 < \beta_\mathrm{i} \leq 1$	$\widetilde{F}_\mathrm{i}(\nu) = \left[1 - i2\pi\nu\tau_\mathrm{i}\right]^{-\beta_\mathrm{i}}$
Cole-Cole (CC)	$0 \leq \alpha_\mathrm{i} < 1 \quad ; \quad \beta_\mathrm{i} = 1$	$\widetilde{F}_\mathrm{i}(\nu) = \left[1 - (i2\pi\nu\tau_\mathrm{i})^{1-\alpha_\mathrm{i}}\right]^{-1}$

Table 3.2.: Havriliak-Negami function and the corresponding simplified peak shapes with constrains in the shape parameters α_i and β_i.

One of the advantages of DRS is also its greatest disadvantage. DRS is applicable for all electrolytes in all solvents because it is not species-specific. All processes that contribute to fluctuations of the macroscopic dipole moment are measured. This also means that processes with similar lifetime overlap. Even the lifetime of a single species may vary depending on its surrounding. Theoretical predictions of relaxation times are in the most cases only approximate.[64,67] This makes the interpretation of DRS spectra very difficult, however, they contain a lot of information on the chemical environment of the species.

The amplitude of a relaxation is given by equation 3.18.

$$S_\mathrm{i} = \frac{\varepsilon}{2\varepsilon + 1} \, \frac{N_\mathrm{A}}{\varepsilon_0 k_\mathrm{B} T} \, c_\mathrm{i}\mu_\mathrm{i,eff}^2 \tag{3.18}$$

From the amplitude S_i of the species i the concentration c_i can determined. In order to do this, the effective dipole moment $\mu_\mathrm{i,eff}$ must be determined. The

effective dipole moment depends on reaction field effects[68,69] and on dipole-dipole correlations.[66,70] N_A is Avogadro's constant, k_B is Boltzmann's constant, and T is the temperature of the system.

3.2.1. Pure Water Dynamics

For the reorientation of water molecules several mechanisms are under discussion. The first approach was done by Debye, who introduced the rotational diffusion, where the water molecules change its orientation in a diffusive way in small angular steps.[71] Recent experimental and theoretical work predict different mechanisms, where water molecules orient in large-amplitude jumps.[72] The kinetics of the reorientation of water is usually described in time correlation functions. Measurements and simulations suggest a wait-and-switch mechanism with two timescales. There are only few techniques capable for the investigation of reorientation processes in this timescale. Most common are IR-pump-probe spectroscopy[73] and NMR[74]. The fast process is attributed to librations, the OH-bond is moving in a conical space (see figure 3.12 a). This movement occurs in a timescale of less than 200 fs. The much slower full reorientation is due to jumps based on the change of binding partner for hydrogen bonds (see figure 3.12 b). This process is at a timescale of a few picoseconds, however, the jump itself is in the sub-picosecond regime. Both mechanisms have been established with the assistance of molecular dynamic simulations[75] and are due to the very challenging experimental measurements still under discussion.[72]

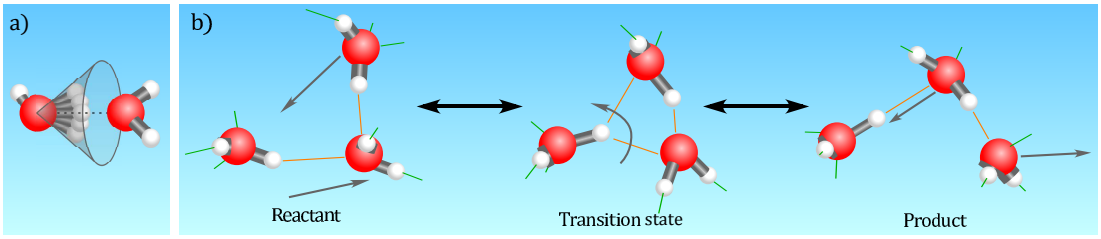

Figure 3.12.: Graphical representation of the reorientation mechanism in pure water according to Laage et al.:[72] a) Libration movement in the sub-picosecond regime, b) Angular jumps.

3.2.2. Solvation Processes

Water is a unique liquid, which is indispensable for many processes. While the water-water interaction covers a wide range of interactions, the solvation processes are even more versatile. As already covered in chapter 2, there is a zoo of ion specific interactions, and among the possible explanation the solvation is always a major argument.

With DRS it is possible to monitor ion solvation by investigation of the water relaxation modes. The dynamic of the solvent molecule is strongly affected by the solute. The relaxation time may be shifted, or the overall amplitude of the water signal may decrease. It is also possible that new modes arise. Basically, the following cases can occur:

- The solvent structure is barely affected by the solute.
- The solvent is slowed down by the solute.
- The solvent is irrotational bound by the solute.

All of these modifications can be directly seen in the spectra except for the last one. If the solute-water interactions are much stronger than the water-water interactions and the exchange rate of the water is sufficiently slow, than the water becomes immobilized on the DRS timescale. Irrotationally bound water leads to a decrease in the amplitude of the overall water signal S_s. The number of irrotational bound solvent molecules per solute molecule Z_ib can be calculated via the difference of the analytic solvent concentration c_s to the measured solvent concentrations of all modes corresponding to the solvent.

$$Z_\mathrm{ib} = \frac{c_\mathrm{s} - c_\mathrm{s,app} - c_\mathrm{s,slow}}{c} \tag{3.19}$$

The apparent water concentration $c_\mathrm{s,app}$ is the concentration measured in the bulk relaxation time regime of water. The slow water mode $c_\mathrm{s,slow}$ may occur, depending on the system. A common approach to separate Z_ib into the ion contributions is to work with a reference ion. Usually chloride is used with $Z_\mathrm{ib}(Cl) = 0$.[76] With the assumption that Z_ib values are additive it is possible to calculate irrotational bound water for ions separately.

$$\begin{aligned} Z_\mathrm{ib}(MCl_\mathrm{x}) &= Z_\mathrm{ib}(M^{x+}) + x \cdot Z_\mathrm{ib}(Cl^-) \\ &= Z_\mathrm{ib}(M^{x+}) \end{aligned} \tag{3.20}$$

The number of irrotational bound molecules varies over a large range. Some ions, such as chloride and potassium have no irrotationally bound water molecules, however, especially highly charged molecules, e.g. Al^{3+} have irrotationally bound molecules at double-digit level.[77] The reduction in the overall water signal in DRS spectra can be therefore explained by irrotational bound water molecules.

Additionally, the relaxation time of the bulk water peak may shift and new water peaks may occur. The shift of the bulk water peak stems from the slight impact the ions have on the bulk structure. The impact of the electrolyte on the bulk water dynamics is mostly composed from the degree of hydrogen bonding of the electrolyte. Depending on the relative strength of ion-water and water-water interaction, the relaxation time of water may slightly change compared to the pure solvent. Other factors are of course the temperature and the viscosity of the solvent. In protic solvents the dynamics of the solvent is dominated by cooperative relaxation of the hydrogen bonding network.[78–81] This relaxation is sometime described as a *wait-and-switch* mechanism, where the hydrogen bonds jump from one bonding position to another.[82] The Stokes-Einstein equation, which relates the relaxation times to the viscosity and temperature is due to these cooperative processes not valid for systems with a hydrogen network. There is a strong effect of the electrolyte itself, depending on its nature the relaxation time may decrease, increase or stay constant.[77] In the description of ions the terms *structure making* and *structure breaking* (see section 2.1) are commonly used. Ions must have – in order to follow this concept – an impact on the water structure beyond the first hydration shell. Many studies, such as DRS,[67,83,84], computer simulations[85,86] and neutron scattering data[87] indicate for many systems the existence of a second or even third hydration shell. Water exchanging quickly from the solvation shell to the bulk might have a slightly altered dynamic, but behave basically as bulk water. The relaxation time of bulk water is in the range of 8 ps.[77]

Additional to the bulk water new water peaks may occur, indicating a different mechanism. For many salts a water peak with a slower relaxation time than bulk water (about 15-30 ps) is found, called 'slow' water.[76,88–90] Slow water can be a result of a special moiety, this is especially observed for the carboxylate moiety,[91] but more often the effect stems from hydrophobic ion solvation.[76] Slow water in the presence of hydrophobic solutes is not a result of stronger hydrogen bonds, but rather because the number and the lifetime of the hydrogen bonds is increased adjacent to the hydrophobic surface.[67] The presence of a slowed down dynamic

of the solvent has been so far only observed in aqueous systems, therefore it is likely that this process is unique to water.[77]

3.2.3. Ion Pairs

Ions pairing is one major topic in the presented work. DRS is a sophisticated method to investigate ion pairs in the bulk, because there is little else contribution in the same spectral region as the ion pairs.[77] Furthermore, it is possible to distinguish between the exact structure of the ion pairs. The solvation and ion pairing interactions seem to have a major impact on the structure. DRS is a powerful method to investigate these processes. Most 'simple' ions are symmetric solvated and are therefore not dipolar. These ions are not observed in DRS measurements. Only if two ions pair, this new structure has an overall dipole moment and therefore gives rise to the DRS signal. This signal is only detectable if the average lifetime of the ion pair is greater than its rotational correlation time. If the lifetime of the complex is sufficiently long, DRS is extremely sensitive for ion pairs.[83] This is due to the large charge separation d in ion pairs leading to a large dipole moment μ_{IP}.[70]

$$\mu_{\mathrm{IP}} = qd + ... \tag{3.21}$$

With this it is possible to detect ion association for systems with a very small equilibrium constant for the ion association.[77]

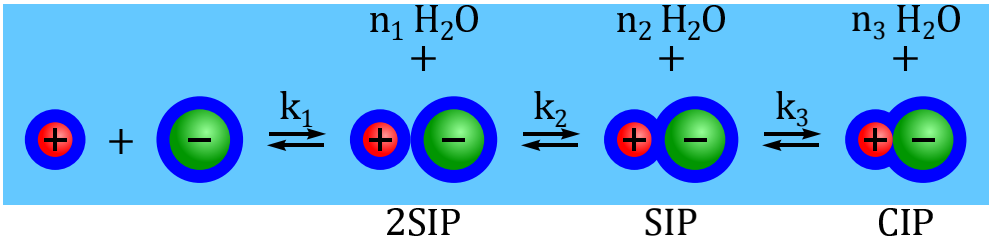

Figure 3.13.: Stepwise ion pairing according to Eugen and Tamm.[92] Both ions are in the unpaired case surrounded by a solvation shell. Upon ion pairing, both of the hydration shells may remain (2SIP). In some cases the hydration shells merge and only one layer of water is in between the ions (SIP). If the attraction between the ions is stronger than the hydration, contact ion pairs (CIPs) may form. All of these states are in equilibrium with each other.

Ion pairs can form different aggregates, they can remain their own hydration shell or share it or go even into direct contact. According to the model by Eigen and Tamm the ions associate step by step, pushing out the separating water (see

figure 3.13).[92] These states are called 'contact ion pair' (CIP), 'solvent-shared ion pair' (SIP) and 'double-solvent-separated ion pair' (2SIP). Usually not all three steps of this mechanism are detectable. With DRS it is very simple to identify the ion pair species, because the dipole moment is direct proportional to the distance of the charge centers (see equation 3.21), and so the position of the peak depends on the ion pair size. The great advantage of DRS is first of all that all these species are detectable, and that there is usually little else contribution in the same spectral range.[77] Other techniques, such as UV-Vis, IR-Raman and NMR are unsuitable for the detection of SIP's and 2SIP's, due to the similarity to hydrated ions.[93] These methods can be used to crosscheck the CIP concentration detected with DRS. One great advantage of DRS over other techniques is the increase in sensitivity from CIP<SIP<2SIP, resulting from equation 3.18. The amplitude is proportional to the dipole moment squared, which is directly correlated to the distance of the centers of charge. This distance is much greater for 2SIP's than for e.g. CIP's (see figure 3.13). For a wide range of ion combinations different ion pair species were found, in some systems even all variations shown in figure 3.13.[77]

3.2.4. Instrumentation

The timescale range of DRS is among the largest of all experimental techniques for the investigation of dynamical processes. This is not possible with a single instrument. The relative permittivity was measured in the frequency range of $0.02\ \text{GHz} \leq \nu \leq 89\ \text{GHz}$. The used instruments are listed in appendix A.4. The values below 50 GHz were measured with a two-port vector network analyzer, in combination with two open-ended dielectric probes. The frequencies higher than 60 GHz were scanned by a waveguide spectrometer with variable path length. The four accessible frequencies are important for the interpretation of the DRS spectra, in our case especially for the determination of the shape function and amplitude of the bulk and fast water peak.

3.3. Supplementary Methods

In this section further methods are presented, which are either used to gain supplementary data to characterize the probe, or which are relevant for the discussion of the data.

3.3.1. Ring Tensiometer

To measure the surface tension of a liquid is basically a very simple task. An object immersed in the liquid undergoes a pulling force depending on the surface tension. A simple setup with a balance measuring this force is sufficient to probe the relative surface tension. The mechanism used to measure the surface tension is based on the force distance curve of pulling an object out of the liquid. It is schematically shown in figure 3.14. The force increases with the distance up to a maximal value. At this point the two lamella are almost parallel to each other. Upon pulling higher, the lamella thins out and becomes more unstable, until the film ruptures. The special geometry at the point of highest force allows a calculation of the surface tension. This relationship is based on the Wilhelmy equation (eq. 3.22) with some correction parameters.

$$\gamma = \frac{F}{2A\cos(\theta)} \tag{3.22}$$

The area A is assumed constant throughout the measurement and for the contact angle θ most often complete wetting ($\theta = 0$) is assumed. The force F is the measured quantity.

The surface tension is used for the characterization, especially the critical micellar concentration is well accessible with a ring tensiometer. Many measuring geometries are based on this basic setup. The Du Noüy ring method uses as a probing object a platinum iridium ring. In this work the K100 ring tensiometer from KRÜSS was used. The device is fully automatic. For each concentration several measurements are taken until the discrepancy between the measurements is small enough. Each measured point is gained by pulling the ring out of the surface until the film ruptures. After one concentration is done, the probe is diluted with the help of microdispensers.

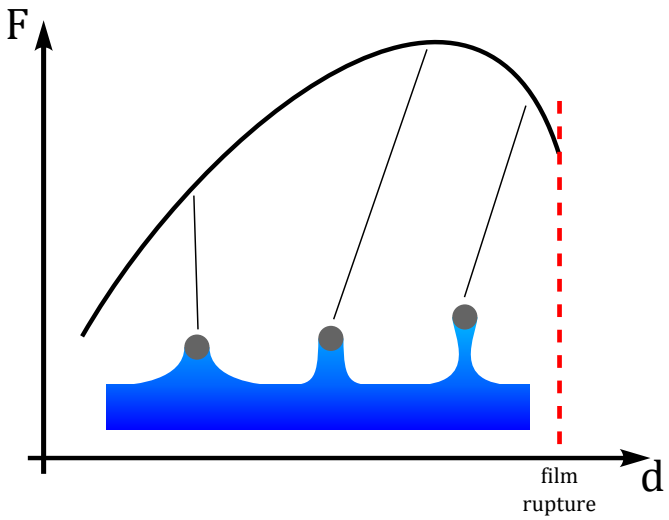

Figure 3.14.: Force distance curve of a film balance. Three example states are shown. At low distances the probe object is well covered by the lamella. At the point of maximal force the lamella is almost parallel. Increasing the distance from this point on leads to a thinning of the lamella upon film rupture.

3.3.2. Langmuir Trough

A Langmuir trough is a combined device that enables manipulation and monitoring of the surface tension of an insoluble amphiphile. It is based on the experiments performed by the female autodidact Agnes Pockels in the 1880s. She was able to perform with rudimentary technical option pioneering experiments on the field of surface tension.[94] This experiment was altered by Langmuir and is today used to manipulate the surface tension of a amphiphile system. The Langmuir trough comprises different components (compare figure 3.16):

- The trough itself is usually coated with Teflon, in order to get a chemical inert hydrophobic surface.
- The surface area of the trough can be adjusted by one or two movable barriers. They block the surface, however they do not reach the ground of the trough. Therefore the bulk phase (usually water or electrolyte) remains the same and only the surface coverage of the amphiphile is changed due to the change in area.
- The surface tension of the film is monitored by a Wilhelmy pressure sensor. A plate or paper is placed vertically in the liquid and a force caused by

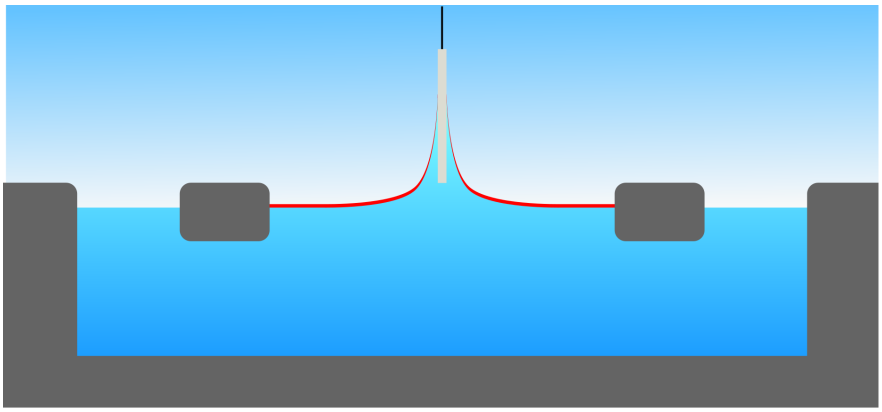

Figure 3.15.: Section plane of a Langmuir trough. The trough is filled with the subphase, in most cases water. A certain area is blocked by movable barriers. On this area the probe is dripped on (in most cases dissolved in chloroform which evaporates). This film alters the surface tension, which is monitored with a Wilhelmy plate.

surface tension is measured by a pressure sensor. Via the Wilhelmy equation (eq. 3.22) the surface tension γ can be extracted.

The simultaneous monitoring of surface area and surface pressure makes it possible to create a surface phase diagram and to gain information on the structure of the amphiphile. This leads to a phase diagram of the two dimensional surface (see figure 3.16). The possible arrangements of the surface phase resemble bulk phases. At low coverage not the entire surface is covered and islands of surface active material float around. This is called the gas phase (G). At higher surface pressure the surface is completely covered and depending on the system different arrangements can occur. Full coverage with an unordered structure similar to a liquid is called liquid expanded phase (LE). At higher pressure some segments of the alkyl chains form ordered structure, but there is no overall ordering. This is called liquid crystalline phase (LC). If the aliphatic chains can condense completely, the crystalline phase (C) can occur. At a certain surface coverage, the minimal area per molecule is achieved. Upon further compression, the so called film collapse (FC) occurs. In this regime the amphiphiles pile up and no well defined monolayer is anymore present. Usually the surface pressure stays at this state constant. Not all probes undergo all states displayed in figure 3.16 upon compression.

The Langmuir trough can also be used for adjusting and perpetuating of a certain surface concentration throughout the measurement with another method,

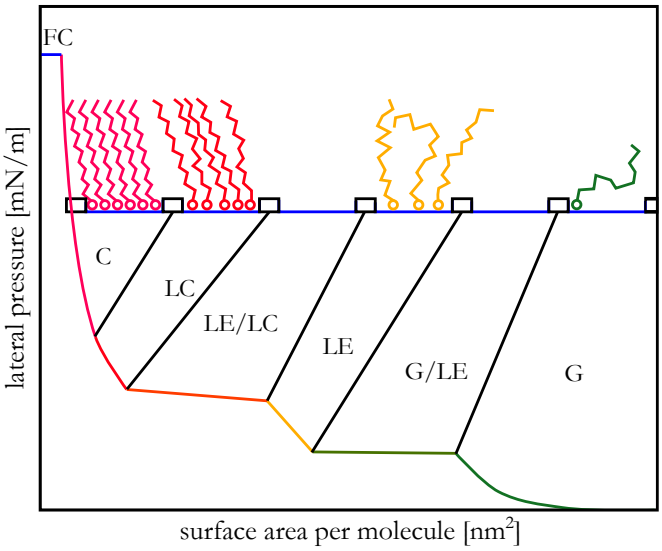

Figure 3.16.: Schematic sketch of a Langmuir isotherm with a representation for each phase and the phase transitions (see text).

e.g. SFG. By this means, the Langmuir trough is a powerful auxiliary agent which makes surface specific measurements of insoluble surfactants very practically.

In this work the Langmuir isotherms were used to describe a catalytic system (section 5). The Langmuir trough as a supplementary device for SFG was used for all insoluble amphiphilic probes to adjust the surface pressure and with it the surface concentration of the probe.

3.3.3. Brewster Angle Microscope

A common method to characterize a Langmuir film is the Brewster angle microscope. For this method a light beam in *p*-polarization is focused on the interface. As shown in section 2.4.3 there is, depending on the refractive indices of the interface, a certain angle at which no *p*-light is reflected. The reflected beam would be perpendicular to the refracted beam, but in this direction the refracted *p*-light has no electric field (see figure 3.17) A light beam adjusted to this angle will not be reflected, unless the interface is modified, e.g. by a lipid film. This film gives rise to a tiny change in the reflected light amplitude, however, the percentage change will be large due to the low absolute intensity. Only at or close to the Brewster angle, a lipid would lead to an easy detectable signal change. Therefore, the Brewster angle microscopy is a versatile tool, which can be used in combination with the Langmuir trough to gain information on the composition of the

surface layer.

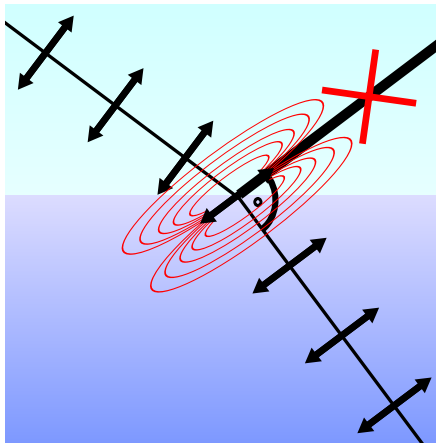

Figure 3.17.: *p*-light at the Brewster angle. The reflected beam is perpendicular to the refracted beam, therefore no electric field strength can be measured in that direction.

3.3.4. Lunkenheimer Surface Purification

In this work many methods probe only the surface of a sample. Therefore it is especially important that the probe is without contamination at the interface. Surface active compounds accumulate at the interface and have great impact on the measured data. Compounds that stem from impurities disturb the system and must be removed. Most cleaning techniques are intended to remove the overall contamination content. This is a suitable approach for most applications, however, in this special case the few remaining contamination accumulate at the place where they disturb most. The routine developed by Klaus Lunkenheimer is based on a device which has - depending on the tilting angle - either a very large or a rather narrow surface area. The compound is cleaned by several iterations of the following routine (see figure 3.18):

1. Surface active impurities adsorb at the expanded surface.
2. The glass vessel is tilted, this leads to a reduction in surface area. The surface active impurities are close packed in a non-equilibrium state.
3. With a capillary most impurities are sucked off from the surface
4. The vessel is tilted back, a new equilibrium can be established.

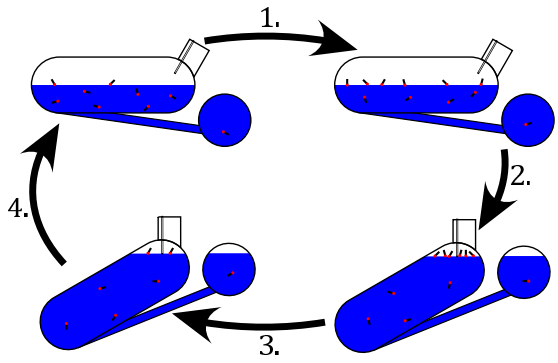

Figure 3.18.: Lunkenheimer purification routine (see text).

This routine is based on two time scales, the slow adsorption of the surface active matter to the surface and the possibility to tilt the vessel rather fast. A good result can be only achieved when in the process the first step is long enough to allow a strong surface coverage (in this work 10 minutes were used) and the second and third step are rather fast (this depends on the machine, usually about 10 seconds). Multiple repetitions lead to a surface clean probe, ready to use for further studies.[95]

In figure 3.19 a SFG spectra of the alkyl and water region before and after purification is shown. In the alkyl region (2800 - 3000 cm^{-1}) the dirty probe shows several peaks. Additional to this, the intensity of the water is dramatically reduced. While the *water-like* peak (approx. 3400 cm^{-1}) remains almost constant, the *ice-like* peak (approx. 3200 cm−1) is strongly suppressed by the impurities at the surface. Therefore, there is an urgent need for rigorous purification in order to get reliable results. All probes were purified with the Lunkenheimer purification device. The successful purification was determined with SFG spectroscopy.

3.3.5. NMR

Nuclear magnetic resonance spectroscopy is a highly specialized research method to determine the electronic environment of single atoms and its interaction with its neighbors. Atoms have a magnetic moment $\vec{\mu}$, which can be oriented with an external magnetic field. Depending on the angular momentum of the atom I the orientation of the magnetic moment is limited certain states. Without an external magnetic field, the different states of the magnetic moment are energetically degenerated, however, according to the Zeeman-Effect the energy difference ΔE of the different states is proportional to the external magnetic field B_0 and to the

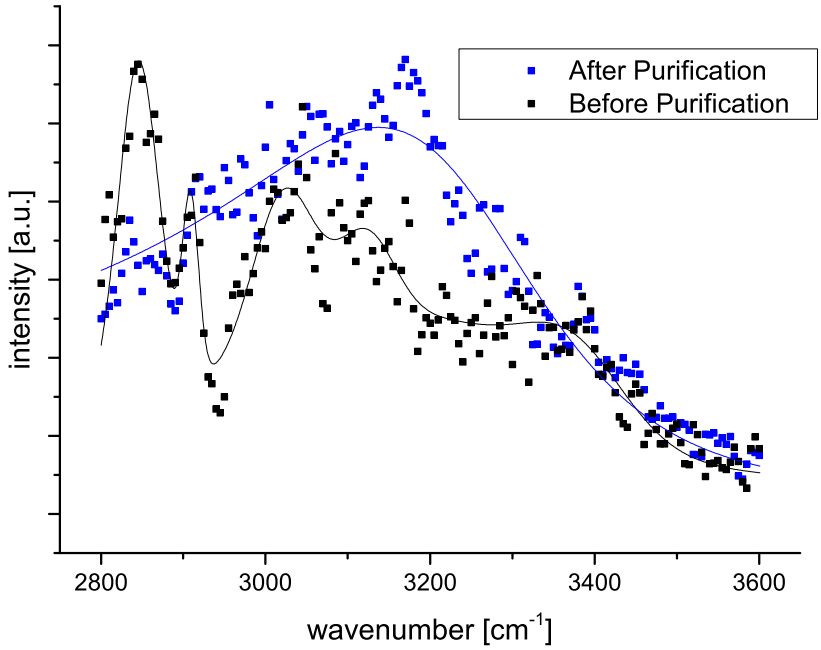

Figure 3.19.: Alkyl and water spectra before and after purification.

gyromagnetic ratio γ.

$$\Delta E = \hbar\gamma B_0 = \hbar\omega_0 \tag{3.23}$$

The Lamor frequency ω_0 depends on the individual magnetic fields at each atom and is therefore a measure for the chemical environment. In the measurement this frequency gets excited with a short pulse, the frequency is then determined with a Fourier transformation.

Neighboring effects lead to the formation of multiplets. In combination with the specific Lamor frequency and the integral intensity of the peaks the structure of a molecule can be in most cases unambiguously determined. NMR was used to verify the composition of the probe from section 6.

3.3.6. Ellipsometry

Ellipsometry is a method which is used to determine dielectric properties and the thickness of thin layers. The basic principle was established in 1887 by Paul Drude, the term ellipsometry is much younger.[96–98]

In ellipsometry, *s*- and *p*-polarized light hits the surface and the complex ratio of the reflectivity coefficients is measured.

$$\rho = \frac{r_\mathrm{p}}{r_\mathrm{s}} \tag{3.24}$$

The elliptometric parameters Ψ and Δ are used to represent this ratio. $\tan\Psi$ is the amplitude ratio of the reflection and Δ is correlated to the phase shift difference of the two polarizations. With this, the central equation of ellipsometry can be established.

$$\rho = \frac{r_\mathrm{p}}{r_\mathrm{s}} = \tan\Psi \mathrm{e}^{\mathrm{i}(\delta_\mathrm{p}-\delta_\mathrm{s})} = \tan\Psi \mathrm{e}^{\mathrm{i}\Delta} \tag{3.25}$$

The great advantage of ellipsometry is the circumstance that not the absolute intensity is measured, but rather a ratio. This makes the measurement itself very stable. With ellipsometry it is possible to gain a large amount of information from the system. However, only in the simplest case of an isotropic, homogeneous and infinitely thick layer can be converted directly into optical constants of the probe via the Fresnel equations. In all other cases the surface must be modeled, which is a possible source of misinterpretation of the data.

3.3.7. SHG

Second harmonic generation spectroscopy (SHG) is based on the same principles as SFG, therefore the selection rules (section 3.1.2) are the same. Instead of two frequencies, only one is irradiated at the probe, generating the double frequency (figure 3.2 in section 3.1). However, the measuring routines of SHG measurements are quite different. In most cases not a spectrum of the wavelengths is token, but at a set wavelength the irradiation angle or the concentration of the probe is changed. One major difference to SFG is the different spectral range covered. Common resonances are in the ultraviolet regime, therefore SHG is very sensitive on push-pull aromatic systems.

3.3.8. MD-Simulation

Molecular dynamics simulation is not a classical analytic method, but rather a computer simulation of a set of molecules. Other than ab initio simulation quite big systems can be modeled, because not a full simulation of all states is done.

Only the interactions and the resulting atomic and molecular movements are modeled. With the iteration over several very small time steps the system gets equilibrated. The force fields are usually based on the Lennard-Jones Potential V_{ij}.

$$V_{\mathrm{ij}} = 4\varepsilon \left[\left(\frac{\sigma}{r}\right)^{1} 2 - \left(\frac{\sigma}{r}\right)^{6} \right] \tag{3.26}$$

ε is the depth of the potential well and σ is the distance where the inter-particle potential is zero. r is the distance between Particle i and particle j. With particular modification of this basic equation it is possible to incorporate additionally to van-der-Waals forces other interactions, such as polarization. With a careful choice of the constrains, MD is a powerful tool to provide possible molecular resolved distributions of atoms in systems. Especially the comparison of MD data with experimental data proved to be very useful.

4 Octahedral Complexes

4.1. Introduction to the System

SFG is known for the selective probe of structure without a center of inversion. Therefore, octahedral complexes are not the typical molecule of choice for second-order nonlinear optical investigations. However, it can occur that the symmetric structure abandons its symmetry due to the non-isotropic forcefields at the interface and give rise to a SFG signal.[99] In this part of the investigation we chose octahedral complexes with cyanide ligands, because they offer an oscillation at about 2000 cm^{-1}, which is well in the spectral range of our device, namely the two simple isoelectronic complexes, potassium hexacyanoferrate(II) ($K_4\,[Fe(CN)_6]$) and potassium hexacyanocobaltate(III) ($K_3[Co(CN)_6]$) in aqueous solution. In the following I will refer to these molecules with the abbreviations **HCF** for the ferrocyanide and **HCC** for the complex with the cobalt central ion. We performed SFG measurements on the cyanide resonance and on the water structure for both molecules. Furthermore, we measured dielectric properties of **HCF** with DRS, in order to compare bulk effects with surface effects.

4.2. Sample Preparation

In this section we investigated the pure air-electrolyte interface. Since all surface active substances accumulate at the interface with a dramatic impact on the surface characteristic, we had to take particular great care on the surface purity. Although the used chemicals are of high purity (see appendix A.3), they still contain surface active material. A specialized purification of the surface is needed. All probes used for SFG were purified by the Lunkenheimer surface purification (see section 3.3.4). The successful cleansing was checked by a SFG spectra of the alkyl range. Only if no signal occurs, we could be sure that no hydro-carbon

material is accumulated at the surface.

4.3. Hexacyanoferrate (HCF)

4.3.1. SFG Measurements on HCF

In preliminary work[100] we performed SFG measurements on the aqueous solution of the ferrocyanide complex. Since both, water and the complex, contain modes in the range of our instrumentation, we could gain information on the molecule itself and on the interfacial water structure of the solution.

Cyanide Modes

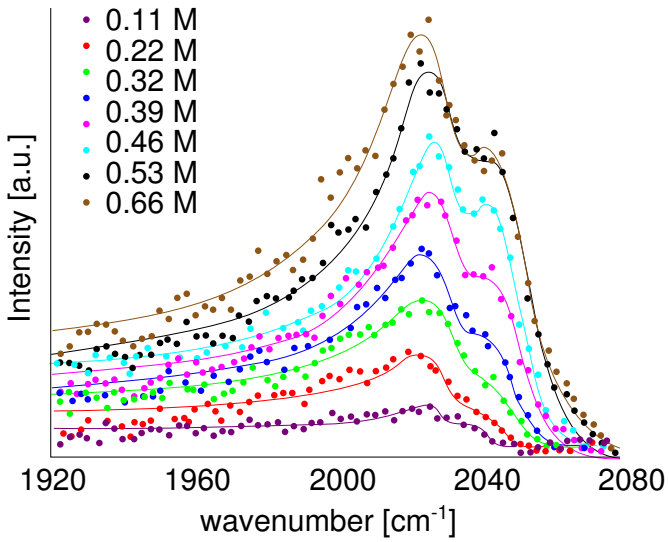

Figure 4.1.: SFG measurement on the cyanide spectra of **HCF** at different concentrations.[100]

The cyanide modes of the complex are well in the range of our device. However, the complex is of octahedral symmetry and therefore one of the most symmetric chemical structures. This should not lead to a signal due to the selection rules which prohibit inversion symmetry. The measurement, however, shows a different picture, in the frequency range of the cyanide stretch a signal occurs which is dependent on the salt concentration (see figure 4.1). Therefore we concluded that the ferrocyanide must dispatch the octahedral configuration at the interface. At

least the chemical environment must be non-octahedral, therefore an anisotrop solvation is another possible picture.

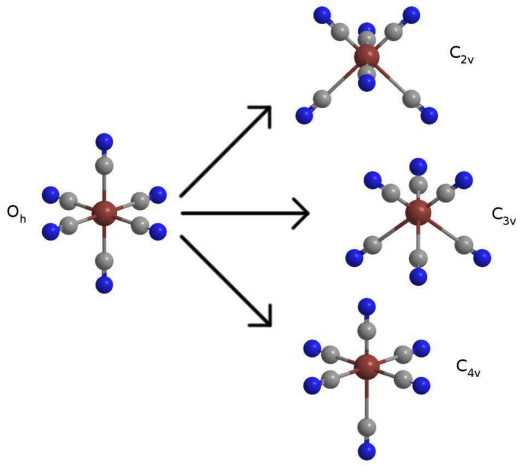

O_h	→	D_{4h}	→	C_{4v}
A_{1g}	→	A_{1g}	→	A_1
A_{2g}	→	B_{1g}	→	B_1
E_g	→	$A_{1g}+B_{1g}$	→	A_1+B_1
T_{1g}	→	$A_{2g}+E_g$	→	A_2+E
T_{2g}	→	$B_{2g}+E_g$	→	B_2+E
A_{1u}	→	A_{1u}	→	A_2
A_{2u}	→	B_{1u}	→	B_2
E_u	→	$A_{1u}+B_{1u}$	→	A_2+B_2
T_{1u}	→	$A_{2u}+E_u$	→	A_1+E
T_{2u}	→	$B_{2u}+E_u$	→	B_1+E

Figure 4.2.: Left: Possible distortions of an octahedral molecule and the corresponding point groups. C_{2v}: edge distortion, C_{3v}: face distortion, C_{4v}: corner distortion. Right: Attribution of the vibrational modes upon symmetry reduction exemplary for corner distortion ($O_h \rightarrow C_{4v}$). The corresponding character charts are listed in appendix A.1. The Raman active modes are labeled in green, the IR active modes in red. The simultaneously IR and Raman active modes, which are therefore SFG active, are marked in blue.

When orienting an octahedral molecule at the surface, three possible SFG active distortions are possible: C_{2v}, C_{3v} and C_{4v} (see figure 4.2). A molecule is SFG active when it has resonances which are simultaneously IR and Raman active. The corresponding point groups (appendix A.1) provide information on this. All of the distorted subgroups have at least two SFG active modes, C_{2v} even three. In figure 4.2 the reduction of symmetry is shown exemplary for the corner distortion ($O_h \rightarrow C_{4v}$), other possible distortions are shown in appendix A.2. The SFG active modes are labeled in blue. We fitted the cyanide spectra with two peaks, but since we have thermal motion most likely, all three subgroups contribute to the signal. Therefore this resonance is probably a mixture of a variety of resonances with two major peaks.

Water Modes

The water signal shows an enhancement compared to pure water (see figure 4.3). Therefore, ferrocyanide orients the interfacial water to a higher extend than salt

free water. The higher signal could be a result from a deeper reaching surface layer or from an overall better oriented thin surface layer or from a combination of both (see figure 3.5 on page 31). To determine the exact surface conformation, SFG is not the suitable tool, but from the data can be retracted that the complex has a major impact on the surface structure. Details on the salt-water interaction were investigated with DRS.

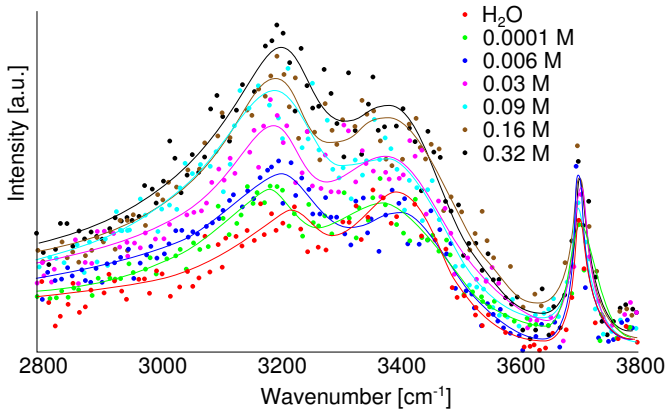

Figure 4.3.: SFG measurement on the water spectra of **HCF** at different concentrations.[100]

4.3.2. DRS Measurements on HCF

Dielectric relaxation spectroscopy measures the dipole relaxation after the orientation in an electric field. Depending on the size, dipole strength, and other parameters, the relaxation varies. With this method it is possible to distinguish between contact ion pairs (CIP), solvent separated ion pairs (SIP) and two solvent shells between the ion pair (2SIP) by its response frequency. With increasing dimension of the dipole, the relaxation becomes slower, therefore CIPs are found in a higher frequency range than e.g. SIPs.

We measured with three devices the spectral range from approximately 0.1 GHz to 89 GHz. The relative permittivity $\epsilon'(\nu)$ and the dielectric loss $\epsilon''(\nu)$ (see figure 4.4) are related by the Kramers-Kronig relation, however, we fitted them separately by the same model in order to avoid systematic errors.

In order to get consistent data, several fit models were tested on the entire measured concentration series. Special care was taken to avoid unphysical behavior. By a least square fit the best setup was found. It consists of four Debye

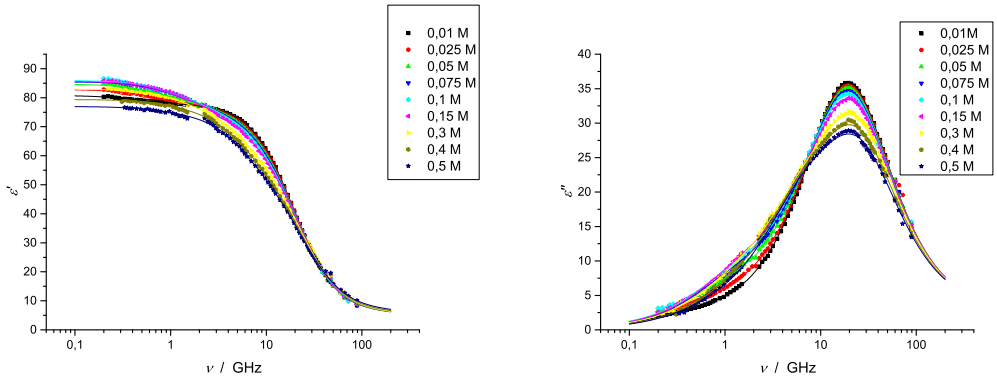

Figure 4.4.: Left: Relative permittivity $\epsilon'(\nu)$ of the measured concentrations. Right: Corresponding dielectric losses $\epsilon''(\nu)$. For each concentration both spectra were fitted simultaneously.

peaks, three of them are attributed to modes of water and the fourth to a SIP of the hexacyanoferrate.

In figure 4.5 the fit for the 0.15 M solution is shown. Although the peaks are very shallow, by the above mentioned criteria this fit is reasonable. The position of the low frequency peak fits well the assumed position of a dipole with the extension of a solvent separated ion pair of a potassium cation and a ferrocyanide anion. The water band is also well known. The slow water band could be assumed to stem from CIP, however, then the total amount of the measured water would be higher than the analytical amount of water. The existence of fast water in general and its relaxation time has been shown in other works.[72]

The change of the different water signals with concentration is shown in figure 4.6 and gives information on the type of water present in the solution. The most prominent peak throughout the measurement is the 'normal' water peak with a relaxation time around 8 ps. The amplitude, however, decreases by increasing potassium ferrocyanide concentration on the measured concentration range almost by half. This is due to the slowed down water resulting in the peak at 28 ps. This water is weakly bound to the ion and therefore the rotation is inhibited. The amplitude of the fast water increases also slightly, however, the error is larger due to its peak position out of the measurable range with the available devices. The amplitudes of the water peaks can be converted to water concentrations having regard to kinetic depolarization and shielding factors according to Sega.[101] Calculating Z_{ib} according to equation 3.19 (page 45) shows that there is no irrotational bound water present in this system.

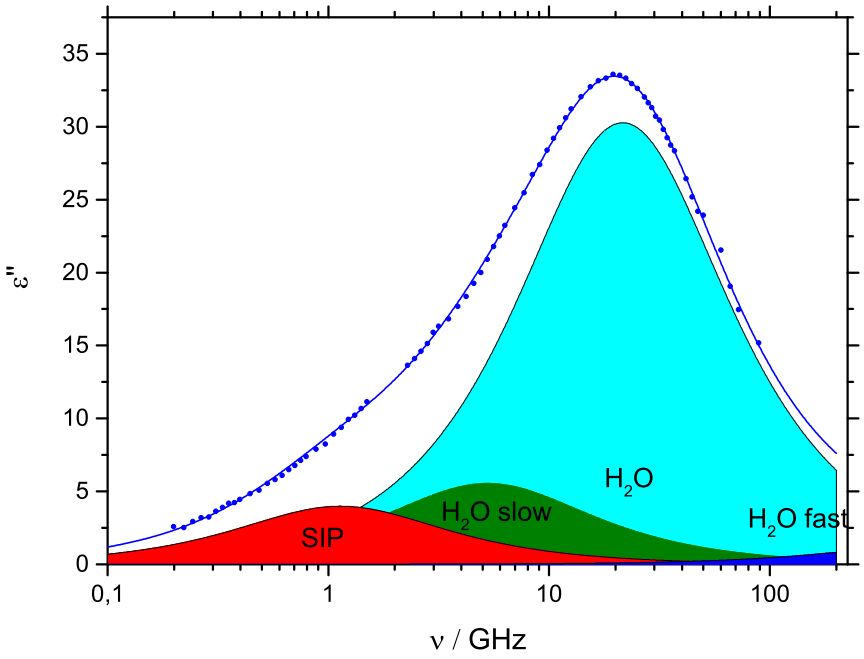

Figure 4.5.: DRS fit of 0.15 M hexacyano ferrate solution.

The transformation of water with the relaxation time of bulk water to slow water with increasing concentration is reasonable, because the ratio of available water molecules per ferrocyanide ion decreases and therefore the modes of water interacting with the ion increase. The hydration number of the complex anion can be retrieved by DRS by subtracting from the overall number of bound water the literature value of potassium according to equation 3.20 (see figure 4.7).[102] The hydration number stays almost constant over the entire concentration range with approximately 40 water molecules per anion (dashed line in figure 4.7). This is compared to other salts a rather high number, therefore has the anion a large ordering effect on the surrounding water. Converting the number of water molecules bound in the hydration shell to a ratio relative to the absolute amount of water, it can be seen that at high concentrations almost every third water molecule is bound in the hydration shell of the salt (see figure 4.7 right).

The SIP mode stems from the ferrocyanide itself. It forms with the counter ion potassium solvent separated ion pairs. Its amplitude is shown in figure 4.8. For the ion pair an association constant of approximately 390 L/mol is retrieved.

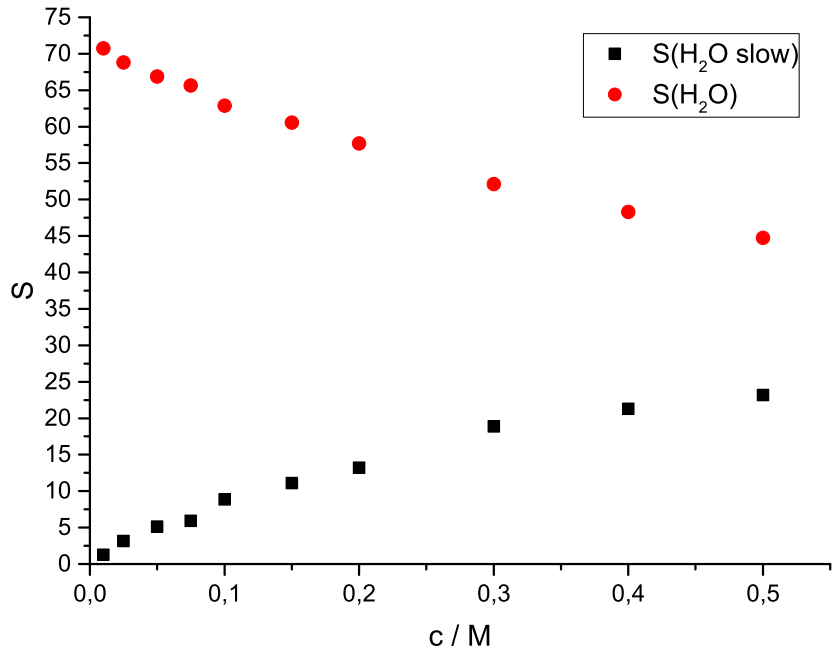

Figure 4.6.: Amplitudes of the normal and slow water modes from **HCF** measured by DRS.

The calculations used for this are analogous to the ones shown by Eiberweiser et al.[102] As expected the amplitude increases with quantity of substance in the low concentration regime. At a concentration of 0.1 mol/L it levels off and decreases further on. Converting this data to relative ion pair concentrations, the percentage of the SIP contribution decreases in a steady fashion (see figure 4.8 right). This means that less SIP's are detected at higher concentrations. There are several possible reasons for this behavior. The ion pair may just dissociate at higher concentrations, however, with approximately every second water molecule bound in the hydration shell, this is rather unlikely. DRS measures permanent dipole moments. In order to decrease the dipole moment, the ion pair can either orient such that the dipole moments cancel, or larger, symmetrical clusters form. The ferrocyanide ion carries a quadruple negative charge and has four potassium counter ions, therefore it is possible that symmetrical clusters form with two or more potassium ions oriented around the anion.

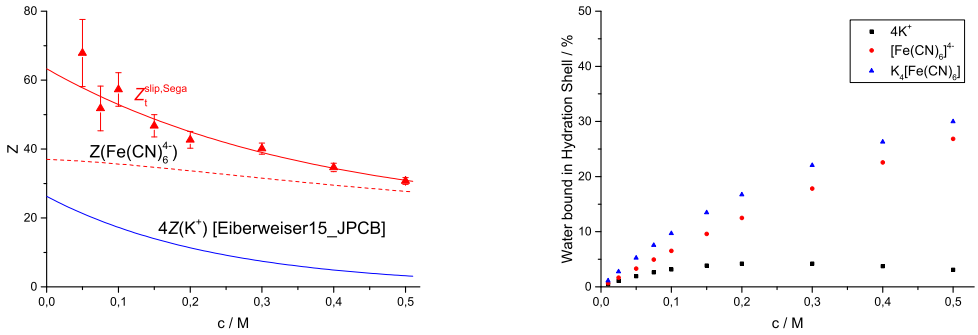

Figure 4.7.: Left: Hydration numbers of $4K^+$ (blue line, according to Eiberweiser et al.[102]) and of the salt corrected for the kinetic depolarization (slip) and the shielding factor according to Sega[101] (red line). The difference of these values gives the hydration number of the anion (dashed line). Right: Ratio of the bound water to the overall water concentration.

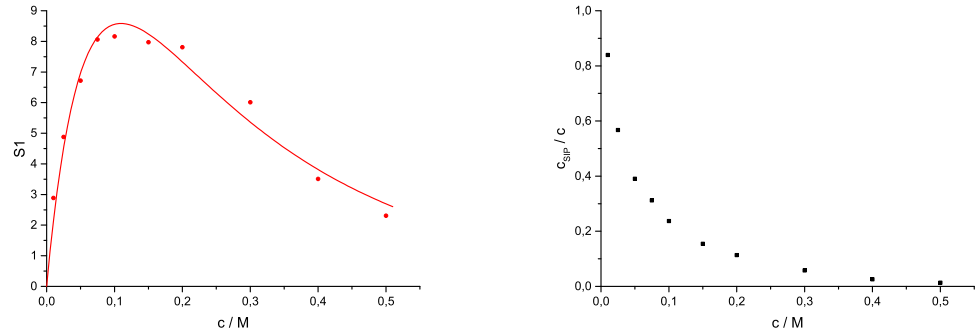

Figure 4.8.: Left: Amplitude change of SIP mode with concentration, right: relative SIP concentration.

4.3.3. Comparison of DRS Data with SFG Data

DRS and SFG are two complimentary methods, while DRS measures properties in the bulk, SFG provides information on surfaces or interfaces. Both methods probe both, the water and the ferrocyanide ion, however they are sensitive to different properties. Both in common is that a center of inversion cancels the signal, however due to different reasons. In second order nonlinear optics, the tensor correlating the electric fields with the polarization is zero and therefore no SFG response can be measured. In DRS only media with a dipole can be probed. If the ion pair is arranged in such a way that no net dipole moment is present, no DRS amplitude can be monitored.

SFG measurements showed an anisotropic orientation at the interface of both, ion and water. Both increase with the ion concentration. A possible explanation for the strong impact of the salt on the ion pair is a layered ordered structure of the ions separated by a water layer.[48] This resembles the picture seen with DRS. However, other than in the bulk no symmetrical clusters can form. Therefore, the SFG water signal increases with concentration increase. On the other hand, the DRS SIP mode decreases, possibly due to the formation of symmetrical clusters.

One likely picture of the water structure therefore is the formation of SIP-like structures between ferrocyanide and the counterion potassium at the interface. This, in combination with the asymmetric solvation leads to a reduction in symmetry from octahedral to lower order point groups and therefore to a SFG active compound. At higher concentrations more potassium binds as SIP to the anion, but while in the bulk the compound looses its permanent dipole moment, at the surface symmetric binding is not possible.

4.4. Hexacyanocobaltate (HCC)

Potassium hexacyanocobaltate (**HCC**) is isoelectronic to potassium ferrocyanide and therefore chemically very similar to the iron complex. We performed the same purification routine as before applying the Lunkenheimer apparatus (see section 3.3.4) and checked for surface impurities by monitoring the SFG signal of the alkyl resonances.

4.4.1. SFG Measurements on HCC

We investigated again both, water signals and cyanide signals. The cyanide modes stem from the complex itself and give therefore information about its structure. The water modes, on the other hand, monitor the water structure at the surface.

Cyanide Modes

The cyanide signal behaves quite similar to the iron complex (see section 4.3.1). The intensity of the cyanide modes increases with concentration almost in a linear manner. This indicates a very similar behavior to the ferrocyanide and is easily understandable. The cobalt complex reduces at the interface its symmetry from octahedral to a lower symmetry. At higher concentrations a strong peak at

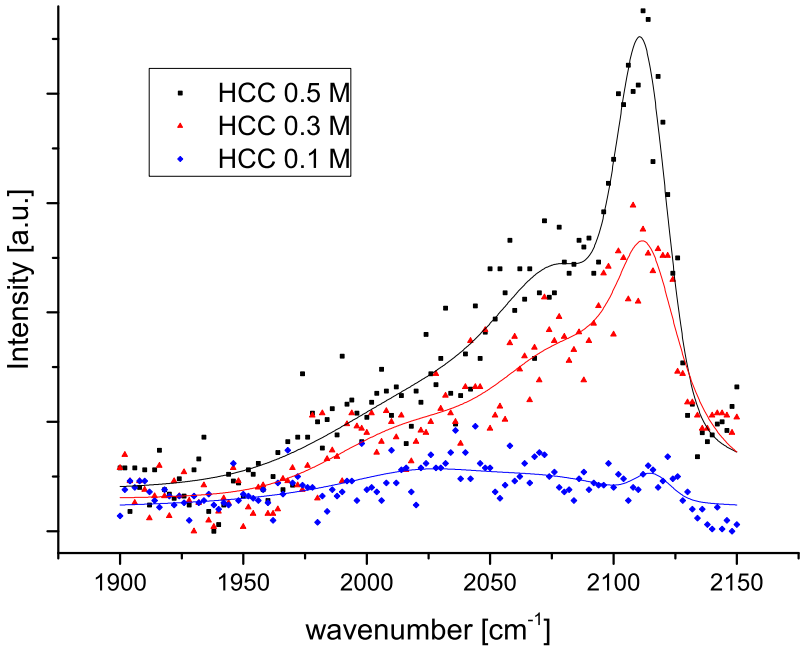

Figure 4.9.: SFG spectra of the cyanide modes of **HCC** at different concentrations.

2110 cm^{-1} occurs, squired by a side peak (see figure 4.9). The shape and the peak position are slightly different to the ferrocyanide (figure 4.1), but the origin of this peak is undoubtedly from the cyanide ligands.

Water Modes

Spectra of the water modes are shown in figure 4.10. Similar to the ferrocyanide, the intensity of the peak at 3200 cm^{-1} is higher than from the 3400 cm^{-1} peak. The surprising behavior of this system is the intensity trend with concentration. In this case, the water intensity does not increase with salt concentration but rather decrease. This means that either the water is less oriented or less water is oriented.

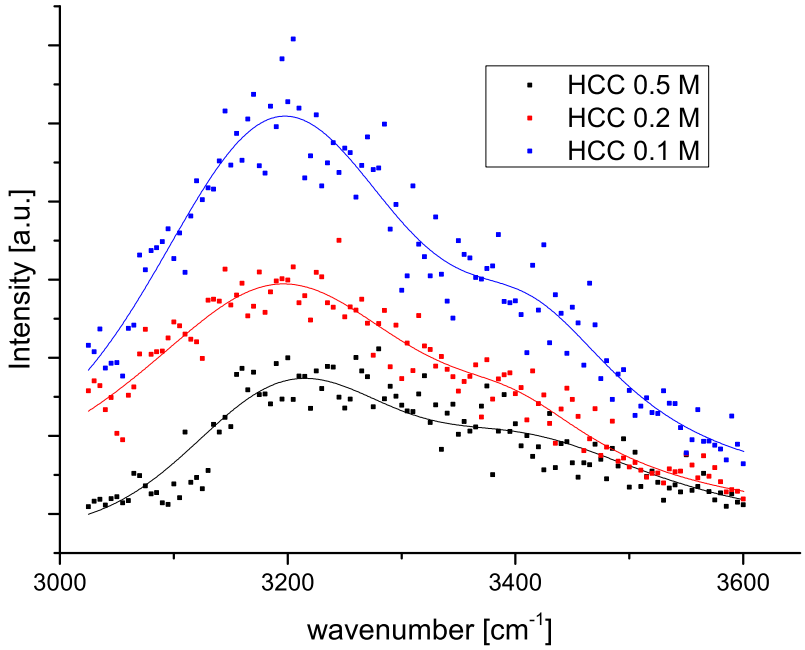

Figure 4.10.: SFG spectra of the water modes of **HCC** at different concentrations.

4.5. Comparison of HCF and HCC

Both, the cyanide and the water resonances contain more than one peak. We did not interpret the single peaks. The exact assignment of the water peaks is still under discussion (see section 3.1.4). The cyanide mode may stem from several confirmations. We interpreted the spectra only in terms of absolute intensity. Thus it is reasonable to compare only the integral intensities of the spectral regimes. In figure 4.11 the integral intensities of the cyanide range (left) and over the water range (right) are shown for both systems at different concentrations.

In all cases the signal intensity increases with concentration except for the water modes of **HCC**. This is quite surprising, since the cyanide mode increases and therefore more **HCC** accumulates at the interface. The chemical very similar ferrocyanide behaves as expected, the **HCF** surface concentration increases and with it the orientation of the interfacial water. **HCF** forms according to the DRS measurements in the bulk SIP ion pairs (see figure 4.12 a). At higher concentrations the SIP mode decreases, possibly due to the formation of an asymmetric

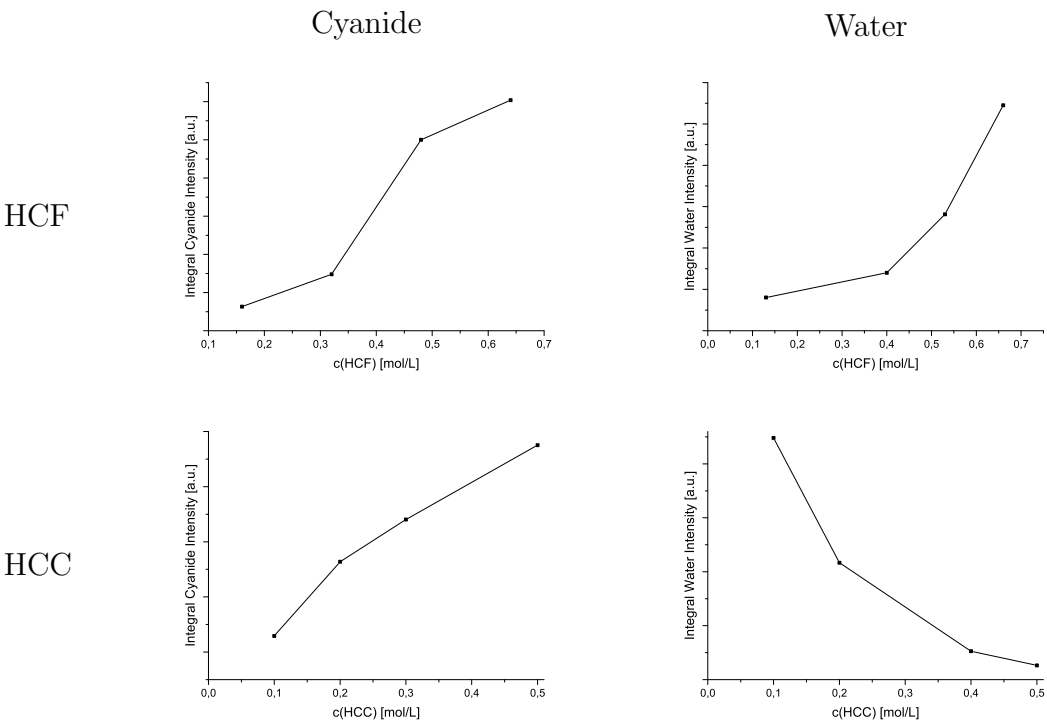

Figure 4.11.: Comparison of integral SFG intensities of the cyanide (1900 - 2150 cm^{-1}) and water spectra (3000 - 3600 cm^{-1}) of **HCF** and **HCC**.

complex (figure 4.12 b). At the surface the condensation most likely takes place as well, but the complex is due to the non-isotropic surrounding not inversion symmetric. Since potassium has a lower surface propensity than ferrocyanide the potassium ions most likely arrange below the complex, separated from the anion by a layer of water (figure 4.12 a). At higher concentrations this separation remains, and due to the higher ion concentration the water is oriented over the entire surface (figure 4.12 b). Therefore the thickness of the surface remains, but the water is within this layer better oriented.

The cobalt complex behaves different. The complex itself gives rise to a similar signal as the ferrocyanide complex. This is because the complex relinquishes the octahedral conformation in favor of a distorted complex. However, the behavior of the counterions is a different one. We know from the cyanide modes, that the anion is present at the interface. Since we need electroneutratility, the counterions must be somewhere in the interfacial region. A layered ion structure with separating water in between, as we postulated it for the **HCF** interface would always lead to an increase in the SFG water signal with concentration. We see the opposite, and the only possible explanation is the direct condensation of the

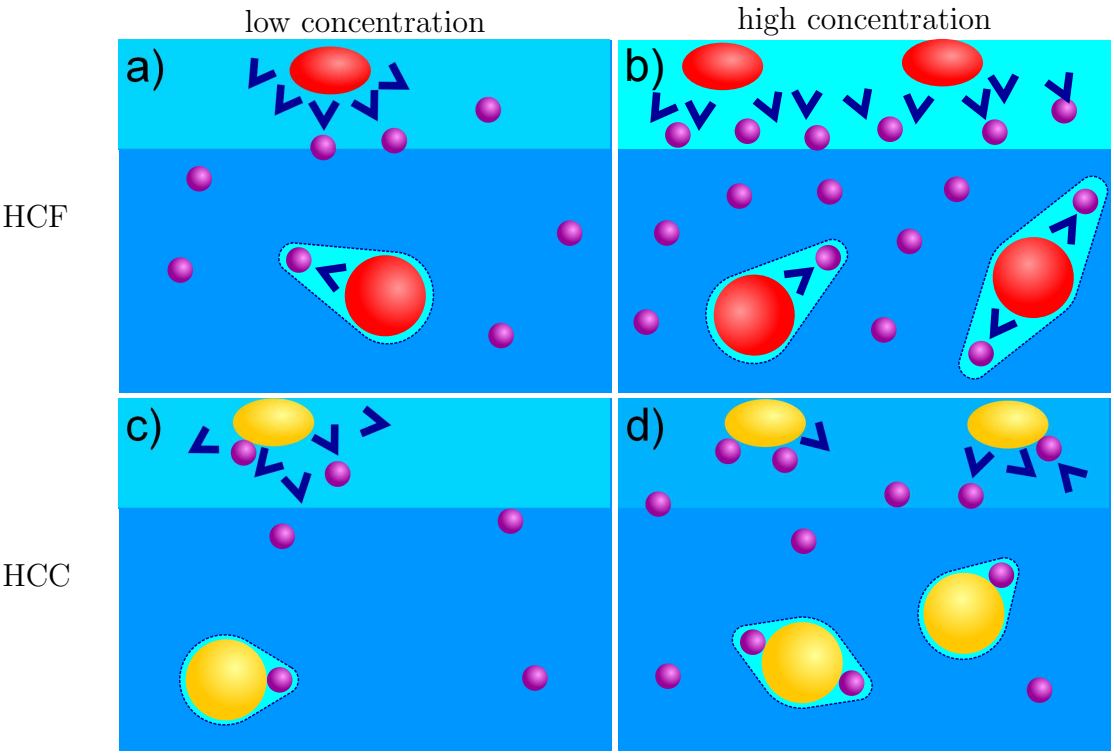

Figure 4.12.: Schematic sketch of possible arrangements of **HCF** and **HCC** at the interface and in the bulk at low and high concentration. The lighter the blue of the interfacial water, the better are the corresponding water molecules aligned.

counterions to anions. At higher salt concentrations the ratio of water to salt decreases and therefore it is likely that more potassium will condense. In this case less water is trapped in between cation and anion. This leads to a reduction of the water signal. Assuming a similar structure for the bulk, we expect to find CIP's (contact ion pairs), which is so far pure postulation.

Comparing the shape of the SFG water signals of **HCF** and **HCC**, the *ice-like* peak of the water has in both cases a higher intensity than the *water-like* peak. The terms *ice-like* and *water-like* state only that the binding angles and distances between atoms is similar to the corresponding structure of bulk ice or water, but not that we have the same structure. However, since both systems have a similar interfacial water architecture according to the peak shape, the non-condensed **HCC** is somewhat similar to water bound in the SIP-like structure of the **HCF** at the interface.

5 Catalysis on Membranes

5.1. Scientific Issue

Energy supply is one of the most challenging current issues. The power demand per capita has strongly increased in the last century, furthermore the population is constantly growing. From this development two major problems occur.

The energy need must be matched and stored. By now it is impossible to match the demand by the use of e.g. only wood, like it was common in Europe over centuries. Other energy sources must be used, in the recent years mostly fossil fuels, but the availability is limited. There is a great need of alternative energy sources to cover the global energy requirements.

Most fuels are linked to environmental pollution. The global warming is partly a result from the extensive use of burning various types of carbon based materials in order to produce heat or power. Another development is the use of nuclear power plants to produce electricity. This approach is a clean way of energy transformation when properly implemented, however, the nuclear waste and the potential danger of this method relativizes the advantages. There are by now few green energy sources, but the demand clearly surpasses the supply.

Many mechanisms to produce energy are strongly linked to a certain place and only work properly at certain times, e.g. wind and solar energy. The energy must be converted to a storable unit that can be released at any given time to meet the current demand. The most promising energy storage mechanisms are based on chemical conversion. The great advantage of this approach is the relatively high energy to volume ratio. Other ways to store energy, such as pumped-storage power plants, work pollution free, but have an immense impact on the environment due to the required extensive constructional measures. One of the main problem of the energy storage is the energy loss when converting from e.g. current to chemical energy. This energy loss can be reduced by optimizing

the occurring reactions. To reduce the activation energy a catalyst can be applied.

Catalysis is one of the most seminal fields in chemistry. The catalyst speeds up a reaction and increases by that the effectiveness of the process. After the reaction, the catalyst recovers its initial state. This process can be optimized by adjusting the system. Homogeneous catalysts have the great advantage that they are directly exposed to the system. Drawbacks of this setup are on the one hand the difficult retraction processes necessary to reuse the catalyst and on the other hand the low probability of a close approach of reactants with the catalyst. This can be improved by reducing the dimensionality of the system to a plane. This can be accomplished by the use of surface active components.

In some applications it is necessary to switch the reaction on and off. This can be achieved e.g. by a photosensitive catalyst, which accelerates the reaction only upon irradiation.

5.2. Description of the System

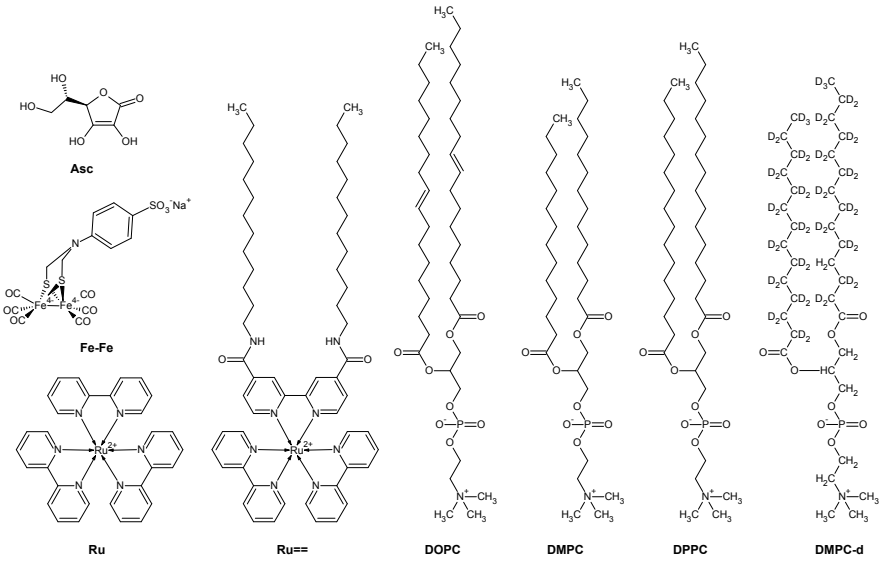

Figure 5.1.: Chemicals used for this investigation with the used abbreviations (see text).

One of the most urgent challenges of our time is the development of clean and sustainable energy sources. Photocatalytic hydrogen production is a promising approach to replace fossil fuels by other storable fuels in order to reduce the CO_2

production. Such systems are based on a photosensitizer, which absorbs light and then excites the catalyst. This catalyst then accelerates the actual reaction which produces hydrogen gas.

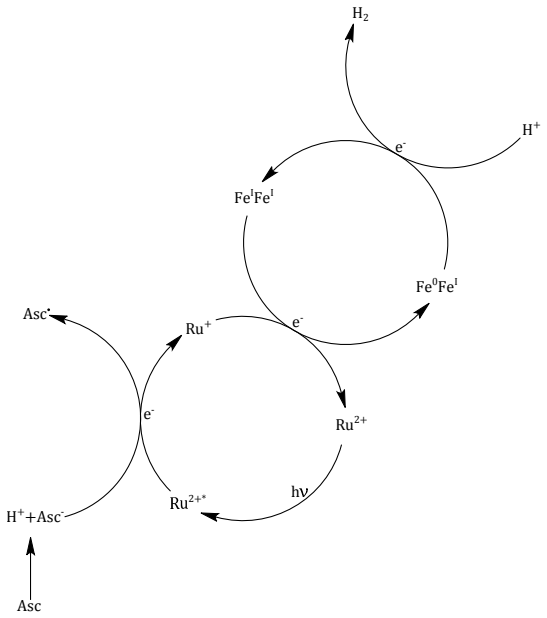

Figure 5.2.: Catalytic circle of the investigated system (see text for further description).

All compounds we used in our study are shown in figure 5.1. In our study we used as a photosensitizer two species of a ruthenium complex. One contains only the headgroup, and to the other one a hydrophobic tail was added (figure 5.1 **Ru** and **Ru==** respectively). The synthesis of the photosensitizer is discussed by Hansen et al.[103] The catalytic circle is displayed in figure 5.2. It can be split in four processes. The central process is the activation of the Ru^{2+} complex upon irradiation. The ascorbic acid (**Asc**, figure 5.1) acts as electron donor for the reduction of the ruthenium complex. This reduced species reacts back to the initial state of the catalyst, while the [FeFe]-hydrogenase (**Fe-Fe**, figure 5.1) gets oxidized. With this compound it is possible to produce hydrogen from protons. The realization of this process is due to solvation problems quite challenging. Very often mixtures of organic solvents and water are applied to overcome this issue. One very elegant approach is based on the introduction of self-assembled amphiphiles. Phospholipids form vesicles and are suitable to conduct this reaction. Different phospholipids were applied, namely **DOPC** (1,2-Dioleoyl-sn-glycero-

3-phosphocholine), **DMPC** (1,2-Dimyristoyl-sn-glycero-3-phosphocholine) and **DPPC** (1,2-Dipalmitoyl-sn-glycero-3-phosphocholine). Additionally, we used a version with a deuterated tail of **DMPC**, abbreviated as **DMPC-d** (structure: see figure 5.1).

Although the phospholipids are not part of the reaction, the efficiency of the conversion strongly depends on them.[104] In figure 5.3 the turnover numbers (*TON*'s) of the pure catalytic system are compared with the values obtained with a phospholipid membrane. The turnover number is the dimensionless ratio of the amount of product to the amount of used catalyst and is therefore a measure for the efficiency of the reaction. Two interesting effects can be seen upon comparison of the *TON*'s, first of all, the addition of a phospholipid membrane has a significant effect on the reaction with an enhancement of the *TON* of more than factor five. Secondly, the different phospholipids provide rather different values. Especially the difference between **DMPC** and **DPPC** is quite astonishing, because the only difference of the two is the chain length (14 carbons vs. 16 carbons behind the ester group).

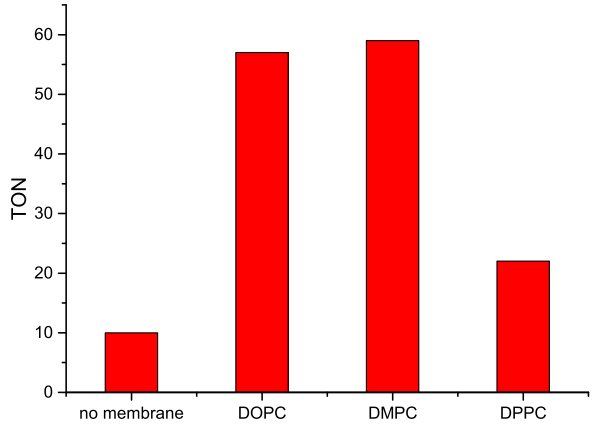

Figure 5.3.: Comparison of the different *TON* values in dependence of the used type of membrane according to Troppmann et al.[104]

The scope of these investigations is to identify the impact of the phospholipids on the reaction. Since the reaction takes place at an interface, we focused on the structural arrangement of the hydrocarbon chains and of the interfacial water. One sophisticated method for this approach is SFG spectroscopy. Some

simplifications and modifications of the system are required to get descriptive results. First of all, not the reaction itself is of interest, but rather the arrangement of single compounds. Therefore important parts of the reaction were left out. Instead of ascorbic acid the pH was adjusted with hydrochloric acid. The vesicle arrangement was replaced by a Langmuir film due to several reasons: A Langmuir film is easily accessible with SFG, a vesicle is much more challenging. Moreover, the packing of the film can be adjusted. For this reason is a Langmuir film much more variable than a vesicle. Drawback of this modification is of course the possible distortion of the system compared to the original one.

With SFG it is possible to gain information about both, the arrangement of the hydrocarbon tails and the water structure at the interface. We always compared the pure phospholipid membrane with a membrane consisting of 10 mol% of the photosensitizer **Ru==**. We prepared the acidic subphase, checked its cleanliness with SFG and dripped the ready mixed membrane molecules solved in chloroform on it. After evaporation of the chloroform the desired surface pressure was adjusted and held while measuring. The hydrocarbon modes were checked for *gauche*-defects to introduce the disorder parameter (see section 3.1.4). This disorder parameter gives information on the structuredness of the alkyl chains. The water modes were used to investigate the impact of the build-in photosensitizer on the direct adjoining water structure. With this data some statements about the head arrangement can be made. In some experiments the water soluble photosensitizer without the alkyl chain **Ru** was used. Since the water soluble catalyst **Fe-Fe** is an important part of the reaction, we checked if there is any impact of it on the interface in order to prove that the catalyst is present at the reaction site.

5.3. Comparison of Different Phospholipids

5.3.1. Impact of the Phospholipid

Surface Pressure Isotherm

Our main focus was the change of structure of the phospholipid layer upon addition of the photosensitizer. Especially the differences in between the different phospholipids were of special interest. First of all we measured the surface pressure isotherms (figure 5.4). While measuring, we always used the Brewster angle

microscope to monitor the film.

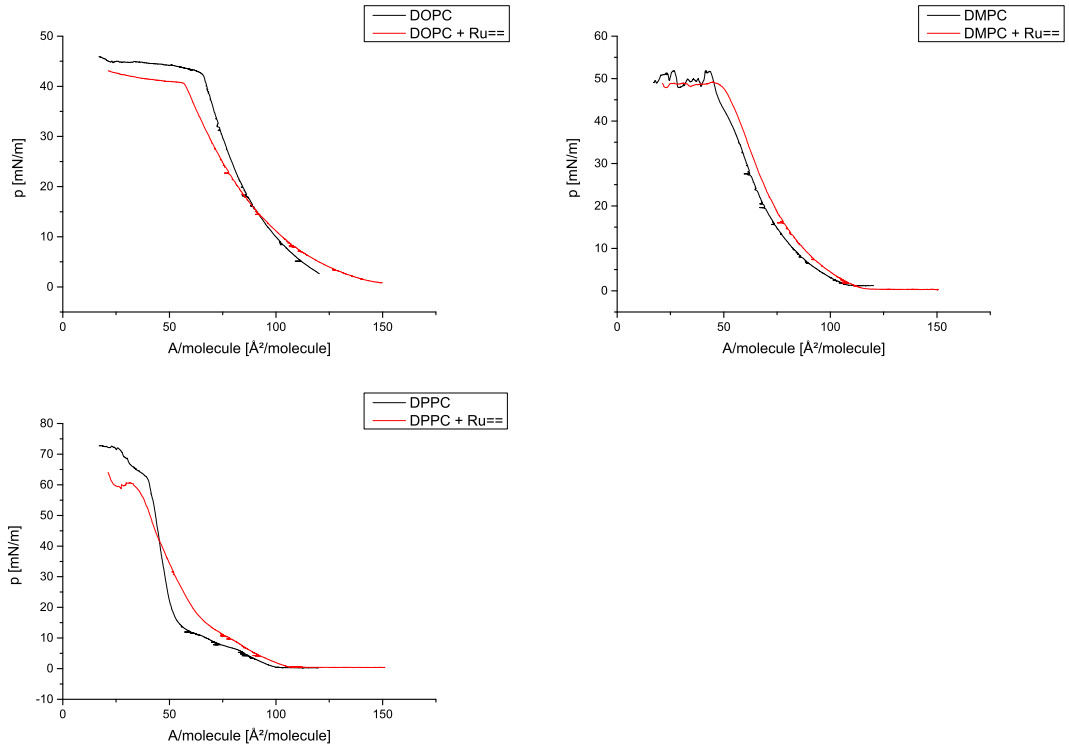

Figure 5.4.: Surface pressure isotherms of **DOPC**, **DMPC** and **DPPC** without (black) and with the photosensitizer **Ru==** (red).

In all cases the isotherms change upon addition of 10 mol% of **Ru==**. At low surface pressures the area per molecule is larger for the mixture. This is reasonable, because the photosensitizer is larger than the phospholipids. Surprisingly, the isotherms behave quite different for higher pressures. In all cases the Brewster angle microscope showed a uniform mixture of the two surface layer components.

For **DMPC** there is almost no difference between the two isotherms. The mixture requires slightly more space than the pure phospholipid, but except that, both graphs behave very similar. The transition from the gas-phase to a condensated phase is at about the same area per molecule and the film collapse occurs at the same surface pressure. This indicates a small impact of the photosensitizer on the phospholipid. Meanwhile, we monitored with the Brewster angle microscope the surface structure, and could not find indications for islands of photosensitizer. Therefore, **Ru==** is well build in into the membrane, and has only little impact on the space requirement itself.

DOPC shows a completely different picture. While for low surface pressures the mixture of **DOPC** and **Ru==** needs much more space, at higher surface pressures the space requirements are reversed. Therefore, at high surface pressures an attractive force is in play. Two processes play a role here, at low surface pressures the greater space requirement per molecule **Ru==** leads to higher average areas per molecule. At high surface pressures the photosensitizer induces a higher ordered structure, resulting in a lower area per molecule. This can only be the case, when the photosensitizer is well build in into the membrane. Another indication for this process is the slightly lower area per molecule at the film collapse.

DPPC is a well investigated system. Other than **DOPC** and **DMPC** a phase transition from the liquid expanded phase to the liquid crystalline phase can be seen in the isotherm. Upon addition of **Ru==** this phase transition vanishes. The photosensitizer acts in this case not as an ordering agent as for **DOPC**, but it rather inhibits the formation of the liquid crystalline phase. The less close packing leads to a larger space requirement of the mixture, except for high pressures, where the liquid crystalline phase is less compressible than the mixture.

SFG

With the SFG investigations we focused on the alkyl modes. Our main measure in this part is the disorder parameter, indicating the amount of *gauche*-defects. This is closely related to the structuredness of the Langmuir film.

In the figure 5.5 the alkyl spectra of pure **DOPC**, **DMPC** and **DPPC** (blue graphs) and of the same with 10 mol% of **Ru==** (red graphs) over acidic water are shown. In all graphs the signal is changed upon addition of the photosensitizer. The symmetric stretch modes of CH_2 ($\approx$ 2844 cm^{-1}) and CH_3 ($\approx$ 2874 cm^{-1}) are well separated from other peaks. Hence, we based our interpretation of the order of the layer on these two peaks. Since both, the CH_2 and the CH_3 mode change intensity, we introduced an disorder parameter as a measure for structural modification of the phospholipid membrane upon addition of the photosensitizer. The disorder parameter is defined as the ratio of amplitudes of the symmetric CH_2 stretch mode to the symmetric CH_3 stretch mode. The CH_3 mode depends mainly on the surface concentration, while the CH_2 mode only occurs where *gauche*-effects are present. The *gauche*-conformation is the less ordered structure especially compared to all-*trans*-chains. Therefore, the lower the

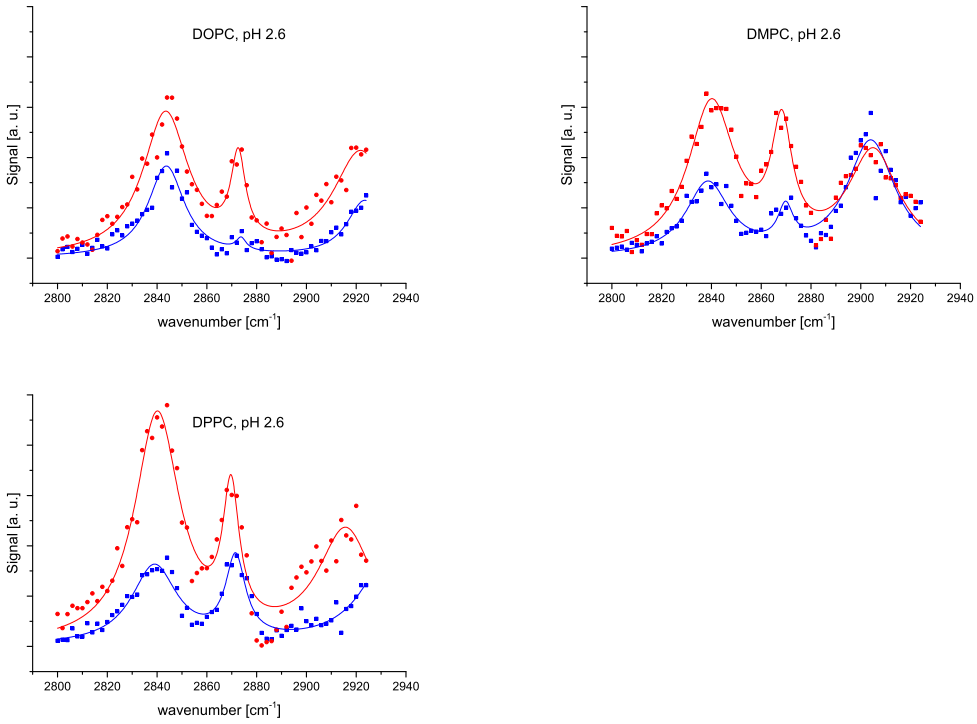

Figure 5.5.: Alkyl spectra of **DOPC**, **DMPC** and **DPPC** with (red) and without (black) 10 mol% of **Ru==** over acidic water.

CH_2 contribution, the lower is the disorder value, and the better is the alkyl chain oriented. We fitted all spectra with Voigt-Profiles and extracted the amplitudes of them. In figure 5.6 the percentage change of the disorder parameter upon addition of the photosensitizer to the membrane is shown. The result is quite astonishing, because in the case of **DOPC** and **DMPC** the alkyl chain order is increases upon the addition of the photosensitizer, for **DOPC** the disorder value of the mixture is nearly half the value of the pure phospholipid. Only for **DPPC**, where the membrane which showed the lowest turnover numbers for the catalytic reaction, the order is even decreased.

This behavior is very similar to the results we have seen in the surface pressure isotherm. **Ru==** induces order in the **DOPC** membrane, while it destroys the structure of the **DPPC** membrane. Only for **DMPC** the isotherm predicted no structural change. Since both, the phospholipids and the photosensitizer have alkyl resonances, we could not distinguish so far, whether the structural changes are mostly due to the phospholipid or photosensitizer structure. This will be

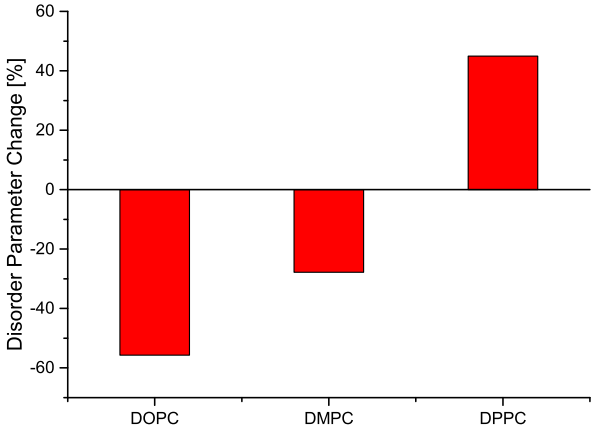

Figure 5.6.: Percentage change of the disorder parameter upon addition of **Ru==** to the different phospholipid membranes.

investigated in section 5.4.

The water spectra are very similar for all three membranes (see figure 5.7 for **DOPC**). The addition of **Ru==** increased the signal in all cases strongly. The charged headgroup has a strong ordering effect to the interfacial water. This can only be the case if the headgroup is directly exposed to the liquid. This suggests in all cases that the photosensitizer is well build in into the membrane, probably with the headgroup sticking out.

5.3.2. Impact of the Subphase

Since we used several simplifications of the interface, we compared the percentage change of the disorder parameter upon modification of the subphase. In the catalytic system the ascorbic acid buffers the solution at pH 2.6. Since we did not want a reaction to take place and **Asc** has alkyl resonances, which would interfere with the film, we decided to adjust the pH instead of it with hydrochloric acid. We were interested in the impact of the pH on the monolayer structure and compared the spectra of two films on neutral and on acidic water (see figure 5.8). The **DOPC** monolayer shows no difference between acidic and neutral water. For the same film with the added photosensitizer **Ru==** there is a slight signal enhancement. Looking at the change of disorder parameter for both systems

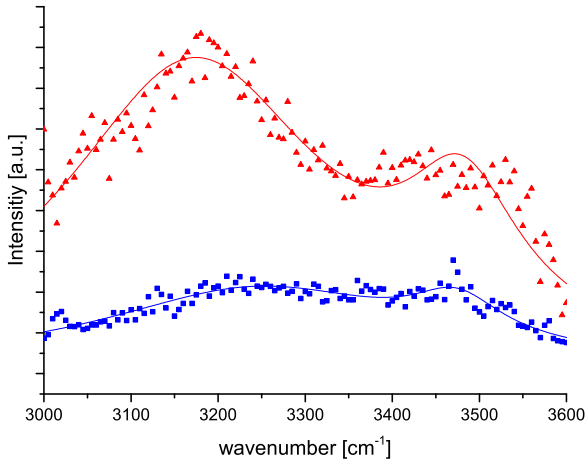

Figure 5.7.: Comparison of the water spectra of **DOPC** with (red) and without (blue) **Ru==**.

(figure 5.11) it becomes clear that the **DOPC** monolayer is almost not affected by the different subphase acidities, however, the photosensitizer slightly reacts on the pH. This is reasonable, because **DOPC** is a neutral molecule while **Ru==** carries a twofold positive charge. Therefore the acidification is a necessary tool to imitate the real system as close as possible.

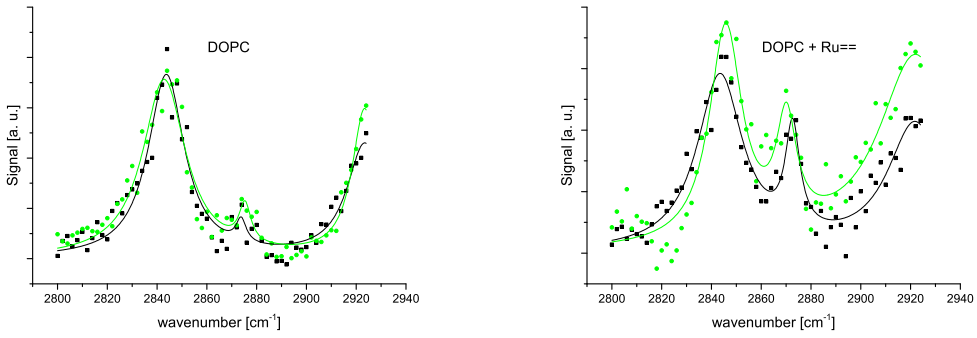

Figure 5.8.: DOPC (left) and **DOPC+Ru==** (right) over neutral water (green) and acidic water (black).

Another simplification of the system is the elimination of the catalyst **Fe-Fe** from the system. The resonances overlap with the monolayer resonances and we wanted to make sure that no reaction occurs. Looking at the alkyl resonances of

the **DOPC** monolayer over acidic water and acidic **Fe-Fe** solution (figure 5.9 left side) a change in signal is seen. The two peaks at wavenumbers below 2900 cm^{-}1 change the intensities in favor for the symmetric CH_3-stretch at ≈2875 cm^{-1}. The symmetric CH_2 stretch mode at ≈2840 cm^{-1} reduces intensity upon addition of **Fe-Fe**. Above 2900 cm^{-1} the spectra change dramatically, the peak is shifted and the intensity is extremely elevated. This could have many reasons, because in this spectral region many alkyl resonances are possible (see table 3.1 in section 3.1.4). Therefore it is not easy to assign a certain resonance to this mode. The catalyst obtains a stiff structure with two fixed CH_2 groups. These CH_2 groups are part of the cause for the strong change in this region. The symmetric CH_2 stretch mode looses intensity, so **Fe-Fe** most likely does not contribute to it. The enhancement of the symmetric CH_3 mode at ≈2880 cm^{-1} must stem from the film, because the catalyst does not have resonances in this spectral region. This indicates the presence of the catalyst at the interface.

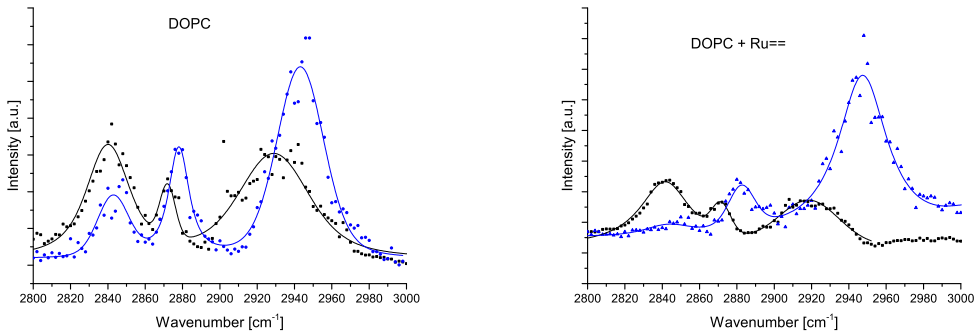

Figure 5.9.: DOPC (left) and **DOPC** + **Ru==** (right) over acidic water (black) and acidic **Fe-Fe** solution (blue).

On the Langmuir film containing the photosensitizer **Ru==** the situation is even more pronounced (see figure 5.9 right side). There is almost no resemblance between the spectra of acidic water (black) and acidic **Fe-Fe** solution. The most significant feature of the spectra is the tremendous rise of the resonance at ≈2940 cm^{-1}. Although this peak showed an increase for the **DOPC** film, here the amplification is by factors higher. The symmetric CH_2 stretch mode is almost canceled and the symmetric CH_3 stretch mode is shifted to higher wavenumbers indicating a different chemical environment. According to Lambert et al. this shift suggests a change from chemical water environment to an air environment (see table 3.1 in section 3.1.4).[58] The disorder of the film is decreased by almost

eighty percent (see figure 5.11). Therefore, **Fe-Fe** is present at the interface, altering the **DOPC** structure, but showing a specific interaction with **Ru==**.

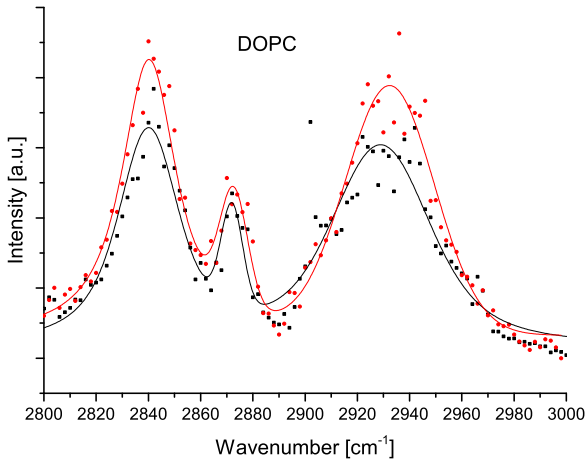

Figure 5.10.: DOPC over acidic water (black) and acidic **Ru** solution (red).

Instead of the amphiphilic photosensitizer **Ru==**, the soluble version **Ru** without the hydrophobic tails can be used (see figure 5.1). We showed already, that the catalyst accumulates at the interface. In order to perform the catalytic circle (figure 5.2) all reactants must be present at the interface. We focused on the impact of **Ru** on the **DOPC** monolayer (figure 5.10). The intensity of all peaks is slightly enhanced. Since the relative intensities, and especially the disorder parameter (figure 5.11), stay constant, this rise may be due to fluctuations of the lasing intensities or to the quality of laser beam alignment. The fluctuations of the lasing intensities should be accounted for by the normalization of the signal (section 3.1.7). Since the relative intensities stay constant (e.g. the disorder parameter in figure 5.11), the intensity enhancement is most likely a relic from the laser beam alignment. Therefore we can state that the soluble photosensitizer **Ru** does not have any impact on the Langmuir monolayer. This implies that it is repelled from the surface. Since the catalyst is attracted from the surface and the soluble photosensitizer **Ru** is repelled, the amphiphilic **Ru==** is the much better choice for the reaction, because in this case all reactants accumulate at the surface.

In figure 5.11 the changes in the disorder parameter upon modification of the sublayer are displayed in combination. Especially the catalyst **Fe-Fe** has

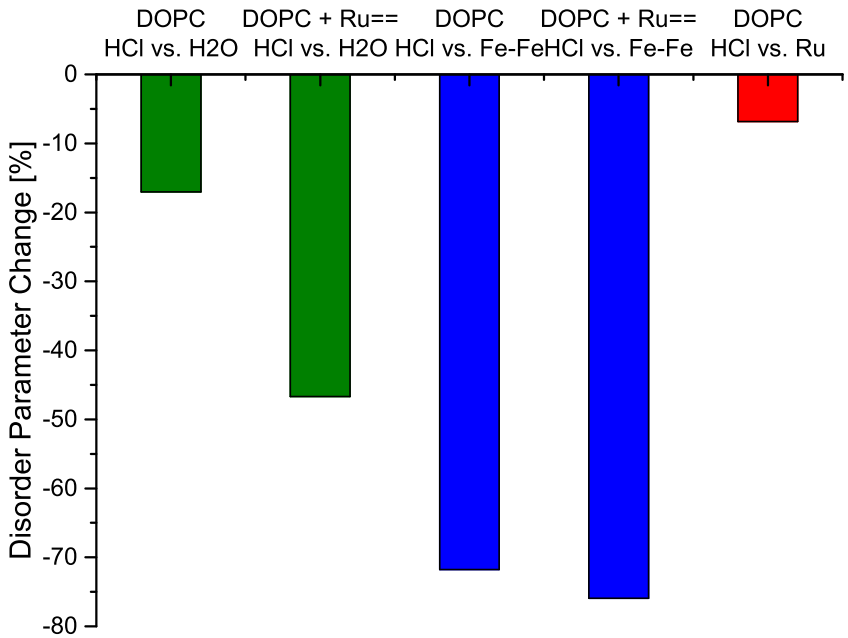

Figure 5.11.: Percentage change of the disorder parameter of **DOPC** of different subphases. Green: HCl vs. neutral water, blue: HCl vs. **Fe-Fe** and red: HCl vs. the soluble **Ru**.

a tremendous impact on the phospholipid membrane with and without photosensitizer a tremendous impact, indicating that it is definitely present at the interface. In all cases the disorder parameter decreases upon modification of the subphase. Since we attribute a low disorder parameter with a good result in the catalytic circle, and the modification of the subphase is always in favor of the more realistic system, the system seems to be close to the optimum catalytic system.

5.4. Deuterated Phospholipids

So far, we could not distinguish between the structure of the phospholipid and the photosensitizer, because both contribute to the alkyl signals. To be able to identify the individual contributions, we used phospholipids with deuterated tails (**DMPC-d** in figure 5.1). The resonances of the deuterated substances

are shifted due to the higher mass of the deuterium to wavenumbers around 2100 cm^{-1} and are therefore well separated from the CH-modes.[59] We compared the earlier measured change in the disorder parameter (see figure 5.6) with the change of the disorder parameter of the deuterated part of the phospholipid. In figure 5.12 this setup is visualized.

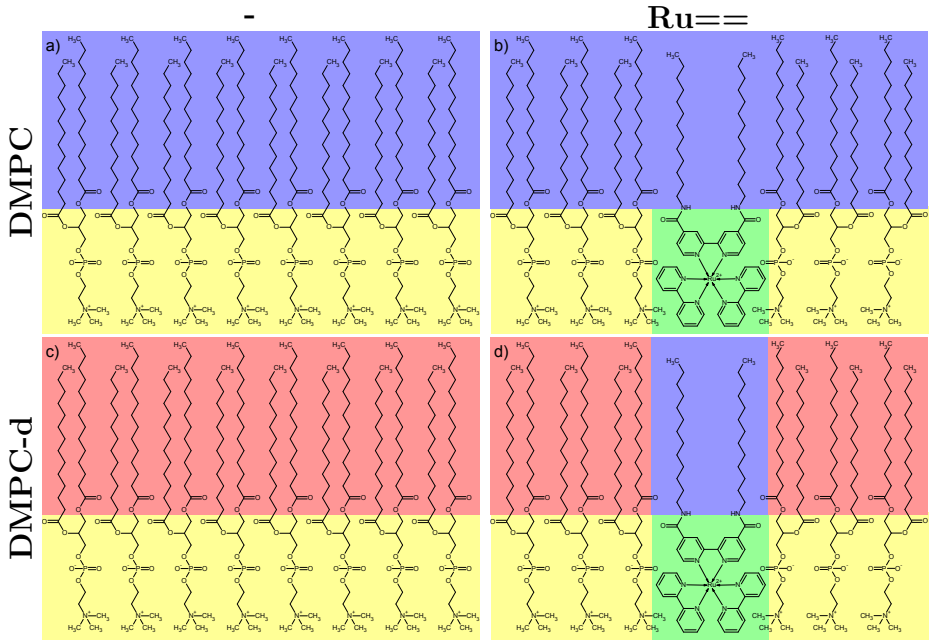

Figure 5.12.: This schematic representation stands for the different investigated compositions. The color codes are the following: yellow and green: headgroups (not measured with SFG), blue: undeuterated alkyl groups, red: deuterated alkyl groups. The left column represents the pure phospholipid without any added photosensitizer. In the right column the photosensitizer is added. In the top row undeuterated phospholipid was used as represented in section 5.3. In the bottom row deuterated phospholipid was used. In all these figures the aliphatic tails are depicted for the sake of simplicity in the all-*trans* conformation, the measurements show that to a certain extend *gauche*-conformations are present.

From the blue marked groups the disorder parameter can be distinguished via the alkyl modes. The red marked part consist of deuterated alkyl chains. The disorder parameter retracted from the deuterated modes is therefore only a measure for the structure of the phospholipids. In figure 5.13 deuterated alkyl spectra of **DMPC-d** and a mixture of **DMPC-d** with **Ru==** are shown. The resulting disorder parameter is calculated in the same way as before with the only difference that the symmetric stretch modes of the deuterated alkyl chain, namely

CD_2 and CD_3 are used. In figure 5.14 the change of the disorder parameter upon addition of **Ru==** compared with the previous determined value of **DMPC** is shown. While the disorder parameter decreases in the case of **DMPC**, it remains almost constant in the deuterated case.

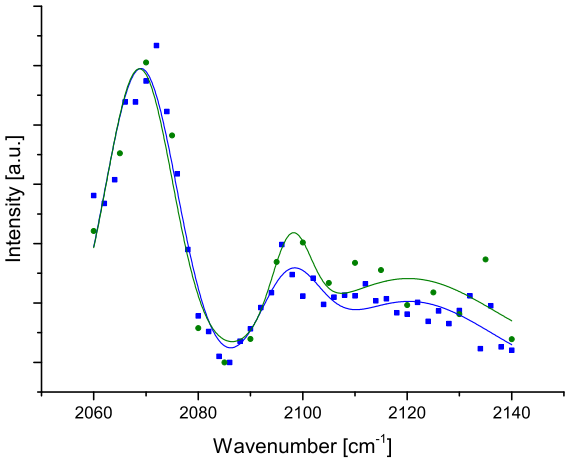

Figure 5.13.: SFG spectra of the deuterated alkyl region of **DMPC-d** with (green) and without (blue) added **Ru==**. The peak allocation are according to Allen et al. the symmetric stretch of the CD_3 (2070 cm^{-1}) and CD_2 modes (2100 cm^{-1}) and the Fermi resonance of CD_3 (2126 cm^{-1}).[59]

The disorder parameter is by definition normalized to the number of CH_3/CD_3 groups. It is therefore in the undeuterated case a measure of the average order of both, phospholipid and photosensitizer. In the deuterated case, only the phospholipid contributes. Since the disorder parameter remains in the deuterated system almost constant, the order of the phospholipid **DMPC** barely changes upon addition of the photosensitizer. Therefore, the previously measured increase in order is mainly based on a contribution of the photosensitizer. In this case, according to the disorder parameter, is the order of **Ru==** much higher than the order of **DMPC**. The structure of the phospholipid is barely altered. This fits well to the data acquired by surface tension measurements. The space requirement of **DMPC** is barely altered by the photosensitizer, and so the structure. Therefore, **Ru==** has a slightly larger headgroup than **DMPC** (according to surface tension measurements) and slightly better ordered alkyl chains (according to SFG spectra of **DMPC-d**).

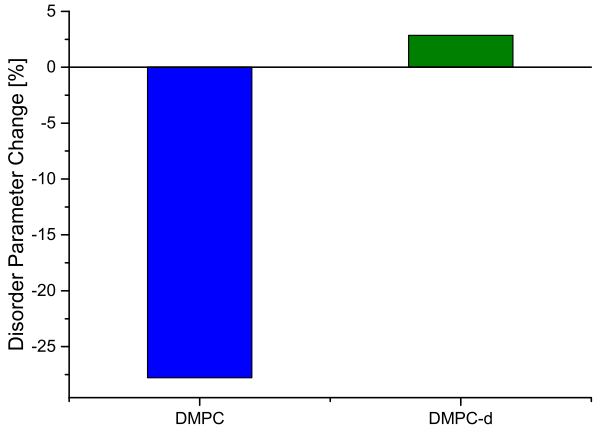

Figure 5.14.: Comparison of the change of disorder parameter over all alkyl chains (blue bar, compare figure 5.12: blue resonances of a) and b)) versus the change of the disorder parameter of only the deuterated **DMPC-d** tails (green bar, compare figure 5.12: red resonances of c) and d)).

Apparently, **Ru==** fits the structure of **DMPC** pretty well, because the surface tension measurements show a strong impact of the photosensitizer in the case of **DOPC** and **DPPC**. In the case of **DPPC**, **Ru==** destroys the well ordered surface structure, and the liquid crystalline phase does not form. In this environment, the reaction is much less effective compared to the other phospholipids. **DOPC** is the only investigated phospholipid with a double bound in the alkyl structure. Therefore, it is not able to form as simple very ordered structures. In this case, the **Ru==** induces structure to the alkyl chain order. The change of the disorder parameter (see figure 5.6) is higher than for **DMPC**, where only the photosensitizer contributes, because in this case both, the photosensitizer and the phospholipid decrease their disorder. Since the turnover numbers of these two systems are very similar (see figure 5.3), the resulting order is similar.

6 Lipid Ion Pairing

The behavior of ions at interfaces is one major object of this thesis. In this part we investigated a system containing an amphiphilic cation and a simple anion as counterion. In figure 6.1 two variants of the molecule are shown. **C12-DMP-Br** is an ion pair, consisting of an amphiphilic cation and the bromide as a simple counter ion. On the other hand, **C12-DMP-bet** is a zwitterionic compound. The structure is identical, except that the negative charge carrying betaine is directly linked to the cation. Therefore, this molecule is classified as zwitterion and not as ion pair.

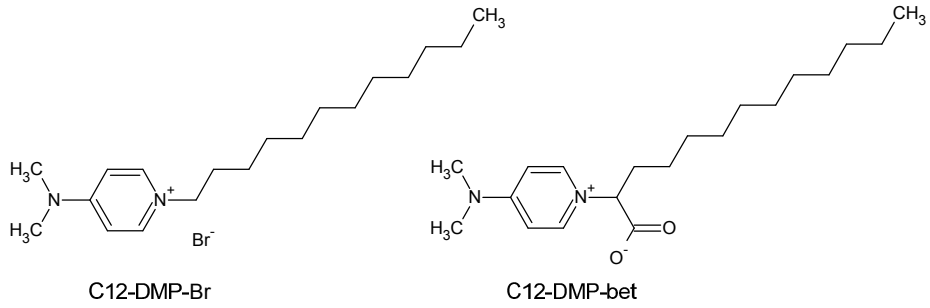

Figure 6.1.: Chemical structures of the molecules used for this investigation: **C12-DMP-Br**: dodecyl dimethylamino pyridine bromide, **C12-DMP-bet**: dodecyl dimethyl pyridinium betaine.

6.1. Preliminary Work

In preliminary work, this system was investigated with SHG, ellipsometry and MD-simulation. Some interesting features occurred in these exploratory investigations, which I will present in the following. To meet the demands, the probes were specifically synthesized for these works. An aromatic push-pull headgroup

is needed for SHG, on the other hand, the aliphatic tail should grant a similar behavior to other tensides.

Both, in the preliminary work and in the here presented work the purification of the probe is an important issue. The Lunkenheimer cleaning device (see section 3.3.4) was applied in both cases. It is important to note, that the stock solution was prepared at a concentration below the critical micelle concentration of 4.31 mmol/L.[105] Contamination can accumulate within the unpolar inner part of the micelle, which makes it inaccessible for this purification process. Upon dilution of the probe the micelles would release the contamination.

6.1.1. SHG

SHG is based on a similar mechanism as SFG (see section 3.3.7). The greatest difference is the different spectral range. Very often, not the wavelength is tuned, but rather the polarization angle of the fundamental. SHG active groups are in most cases aromatic push-pull structures. In this work, the headgroup of the **C12-DMP** derivates gives rise to the SHG signal. The number density N is proportional to the susceptibility $\chi^{(2)}$ (see equation 3.6 in section 3.1.2). The orientation of the headgroup can be examined with an intensity spectra over the different polarizations of the fundamental, called a polar diagram. In the case of **C12-DMP-Br**, the tilt angle is constant at 49° over all concentrations.[105] This is a quite common behavior of surfactants.[106] Since the orientation remains constant at all bulk concentrations, the intensity is directly proportional to the number density squared.

SHG is an intrinsic surface specific method. Therefore, only the molecules at the surface contribute to the signal. The investigated **C12-DMP** cation is amphiphilic and forms below the cmc a monolayer. SHG is therefore a direct probe of the surface coverage of the lipid. In figure 6.2 the SHG signal in terms of concentration is shown, as measured by Teppner et al.[105] The signal increases in a monotonic, almost linear fashion, indicating an accumulation of the lipid at the surface with increasing bulk concentration.

6.1.2. Ellipsometry

Ellipsometry is a non-destructive optical method to characterize thin films and surfaces (see section 3.3.6). From the amplitude ratio of the reflection, $\tan\Psi$, and

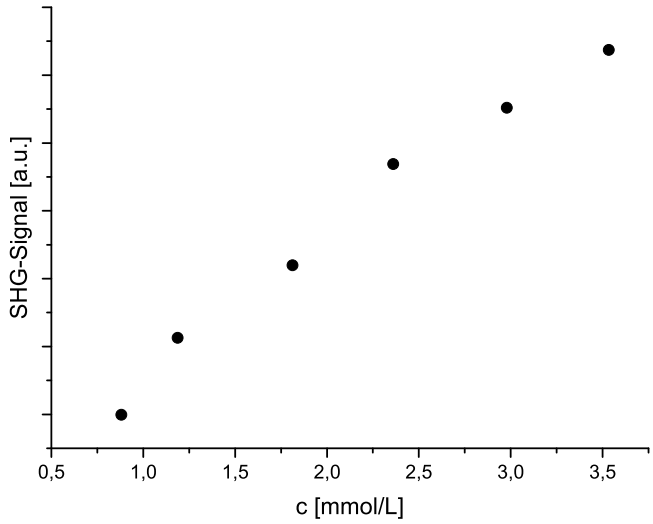

Figure 6.2.: SHG signal of **C12-DMP-Br** according to Teppner et al.[105]

the phase shift Δ of the two polarizations information over the surface architecture can be retrieved. The great drawback of this method is the need of modeling the surface with realistic concentration profiles, since the only unambiguous interpretation is possible for the case of an isotropic, homogeneous and infinitely thick surface layer. The change of bare to the film covered surface $d\Delta = \Delta - \Delta_0$ is in most cases assumed to be proportional to the adsorbed amount. Usually, ellipsometric data change with concentration in a monotonic manner. A positive sign of $d\Delta$ is interpreted in such a way that air is the effective environment of the adsorption layer, a negative sign on the other hand indicates an aqueous chemical environment of the surfactant.

In figure 6.3 the Ellipsometric data from Teppner et al. are reprinted.[107] $d\Delta$ decreases and runs through a minimum at approximately 1.75 mmol/L. At higher concentrations the values of $d\Delta$ increase again. This is a quite unusual behavior for ellipsometric data of a lipid layer. The concentration is almost direct proportional to the surface coverage (figure 6.2), this means that two different surface coverages reveal the same refractive index. Taking only the adsorbed layer into account, this behavior cannot be described, because the refractive index of the layer n_{layer} depends on the surface coverage.[108] For the explanation of this behavior, we have to take the sublayer into account. The surface is build up from the film, followed by a diffuse layer. Since the film is charged, a Stern layer can form, where

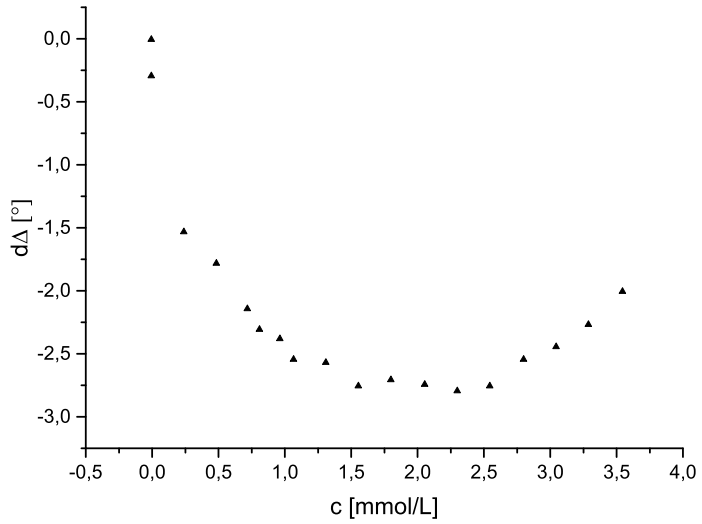

Figure 6.3.: Ellipsometry signal of **C12-DMP-Br** according to Teppner et al.[107]

some counterions are condensed to the surface layer. The Stern layer screens the surface layer charge, resulting in a less deep reaching diffuse layer. With such a model system it was possible to fit the ellipsometric data, assuming the formation of contact ion pairs to set off only at higher concentrations. This was supported by the measurement of the specific charge per adsorbed **C12-DMP** cation.[107] Close to the extreme value of Ellipsometry, the charge per molecule begins to decrease from approximately 1 elementary charge per molecule to about 0.1 elementary charge per molecule close to the cmc, indicating the adsorption of the counterions at the surface layer.

As a reference, a zwitterionic species **C12-DMP-bet** (see figure 6.1) was used. This molecule is chemically identically, only instead of the free counterion, a negative charged betaine group is firmly attached to the molecule. Therefore, no charged surface is present, and therefore no diffuse counterion layer. In this case, the surface will play the predominant role of the refractive index. In figure 6.4 the ellipsometric data on **C12-DMP-bet** from Teppner et al.[107] are reprinted. Other than **C12-DMP-Br** the curve does not attain a minimal $d\Delta$ value at intermediate concentration, but decreases as expected for such system in a monotonic manner. This fits the introduced model, because here no counterions can condense, and therefore there are not two opposing effects leading to an extremum at intermediate concentrations.

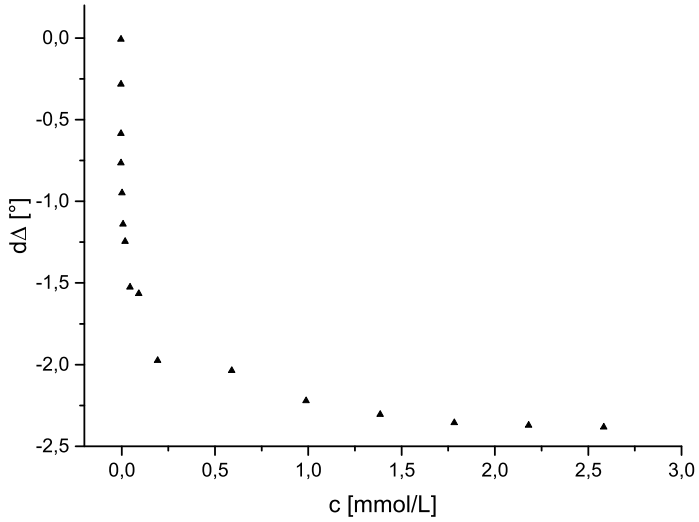

Figure 6.4.: Ellipsometry signal of **C12-DMP-bet** according to Teppner et al.[107]

6.1.3. MD-Simulation

The group of Pavel Jungwirth compared with MD simulation (see section 3.3.8) the density profiles of **C12-DMP-Br** and **C12-DMP-bet**.[109] The hydrophobic part of **C12-DMP-Br** and **C12-DMP-bet** stay almost exclusively at the surface. The distribution of the nitrogen of the headgroup broadens at higher concentrations, indicating the formation of a sublayer. The density profile of the bromide counterions has a peak at the same z-position as the nitrogen peak, however, the probability density reaches into the bulk. At higher concentrations the relative amount of bromide residing close to the interface increases.

The addition of the simple salt **KF** to **C12-DMP-Br** and **C12-DMP-bet** was probed as well with MD simulation. Both, potassium and fluorine have a low surface propensity. The potassium is additionally repelled from the surface due to the charge of the **C12-DMP** cation, and therefore resides almost exclusively in the bulk. The fluoride has a peak in the probability density curve, but this peak lies below the z-value of the maximum densities of the **C12-DMP** headgroup and the bromide anion. For **C12-DMP-bet** the picture is similar, however, in this case fluoride and potassium are equally repelled from the surface. Therefore, there is no specific interaction between either potassium or fluoride and the surface layer. The only attraction for the fluoride is given purely by electrostatics.

KBr, however, shows a slightly different picture. We know from the pure **C12-DMP-Br** solution that the bromide likes to reside close to the headgroup. This proved to be not only an electrostatic feature, because upon the addition of **KBr** to **C12-DMP-bet** a bromide peak at the same z-position as the headgroup occurred. This completely different behavior than the fluoride anion indicates a specific interaction of the bromide with the headgroup.

6.2. Measurements on C12-DMP-Br

We have seen in the preliminary work, that the presented system shows an unusual behavior of the interface. A model was postulated, where the ions condense at higher concentrations. It is expected that not only the solutes are affected by this change of structure, but the interfacial water structure as well. The scope of these investigations is to verify the postulated model with SFG data.

6.2.1. Evaluation of the Purity of the Probe

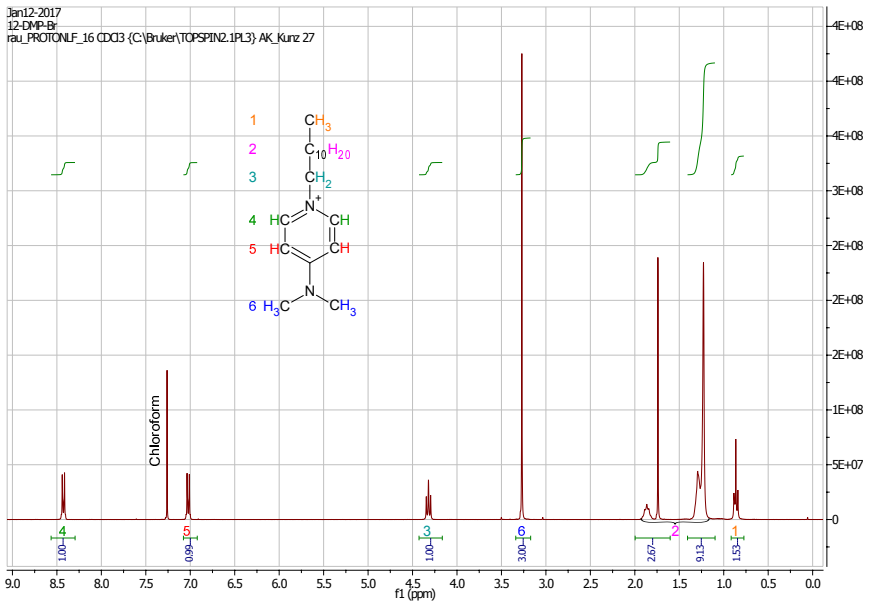

Figure 6.5.: ^{1}H-NMR of **C12-DMP-Br** dissolved in **$CDCl_3$**. The hydrogen atoms are color coded and the numbers link them to the corresponding peaks.

The probe was specifically synthesized to meet the demands of the investigation. To evaluate the quality of the probe in terms of identity and purity we

performed NMR-measurements (see section 3.3.5). ^{1}H-NMR is a suitable method for it, because the positions of the peaks are very characteristic for the particular chemical environment and the integrals give a relative concentration of all hydrogen atoms. In figure 6.5 the NMR spectrum of the used **C12-DMP-Br** is shown. All peaks could be attributed to the molecule, and the relative intensities of the contributions indicate a pure substance.

6.2.2. SFG Investigation of the System

In our SFG measurements we focused on two spectral regions, the alkyl region at about 2800-3000 cm^{-1} and the water spectra at wavenumbers higher than 3000 cm^{-1}. The alkyl modes give information on the structure of the monolayer, while the water modes are a measure for the water orientation below the lipid monolayer. We measured **C12-DMP-Br** in pure water and with added **NaBr** and **NaI**.

Alkyl Spectra

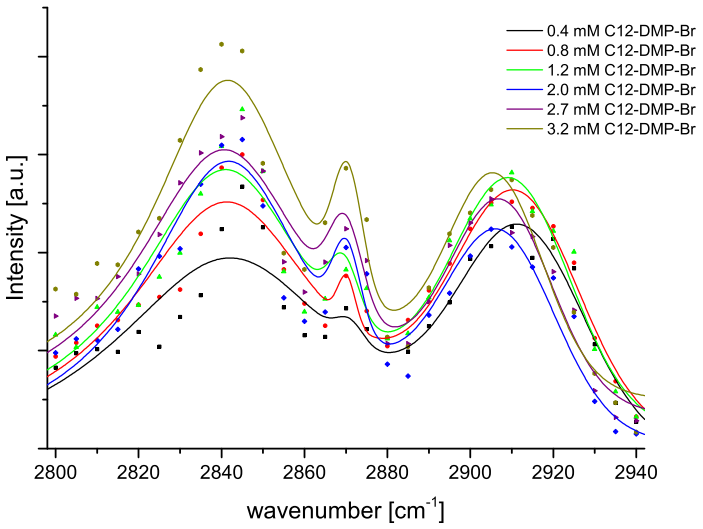

Figure 6.6.: SFG spectra of the alkyl spectra of different **C12-DMP-Br** concentrations.

In figure 6.6 the fitted alkyl peaks of **C12-DMP-Br** are shown. The intensity of all modes increases with increasing bulk concentration. This is reasonable,

because the amount of adsorbed substance increases (compare SHG data).

For the change in structure it proved to be useful to examine the disorder parameter. The ratio of the symmetric CH_2-stretch peak at approximately 2870 cm^{-1} to the symmetric CH_3-stretch mode at approximately 2842 cm^{-1} is a measure for the disorder of the system. The resulting values are shown in figure 6.7.

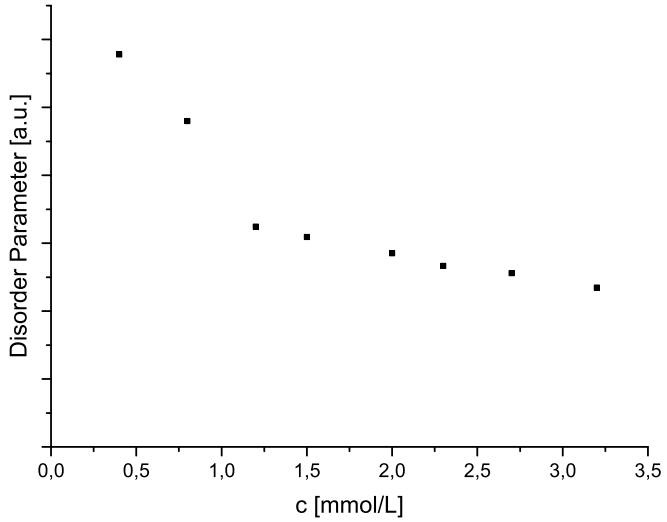

Figure 6.7.: Disorder parameter of **C12-DMP-Br**.

The disorder parameter decreases in a monotonic fashion over the entire concentration range. This correlates well with the previous data, especially with the SHG data. The higher the bulk concentration, the more lipids will contribute to the monolayer. This denser structure is only possible with better packed aliphatic tails, and accordingly with less *gauche*-defects per molecule.

Water Spectra

The water spectra of the pure **C12-DMP-Br** solutions do not change much with concentration. However, the intensity of the modes is very much increased compared to the pure water surface. In figure 6.8 the spectra of the entire measured wavenumber range are shown. For comparison, a spectra of pure water enhanced in intensity by factor 10 is additionally added to the graph.

It is blatant that the lipid alters the interfacial water structure dramatically.

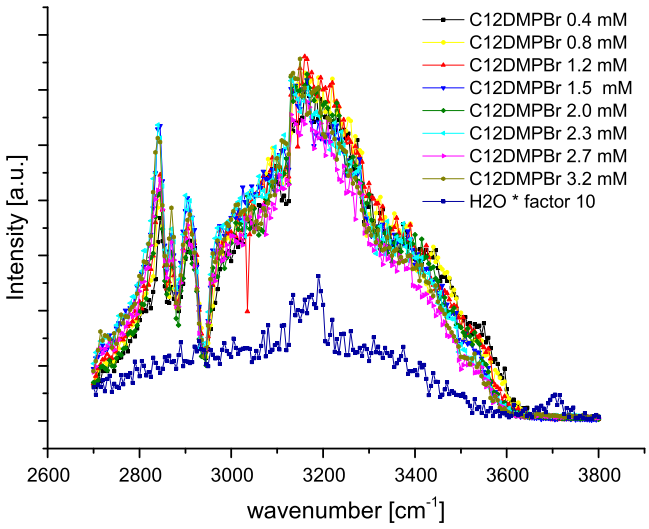

Figure 6.8.: Cumulative SFG spectra of **C12-DMP-Br** at different concentrations. In dark blue the reference spectra of pure water is shown with an intensity enhancement by factor 10.

The intensity of the water modes increases by far more than factor ten. Meanwhile, the dangling OH-mode at 3700 cm^{-1} vanishes, indicating a covered surface. Although there is no dramatic effect seen on the water intensity within different concentrations, a slight ordering becomes apparent. In figure 6.9 the integrals over the entire water regime (3000-3800 cm^{-1}) are plotted versus the concentration. Despite the small changes, a trend is visible; the intensity of the water signal slightly decreases, while the concentration increases.

6.2.3. Interpretation of the Data

Upon changing the concentration of **C12-DMP-Br**, two mechanism take place. First of all, the number of adsorbed amphiphilic cations increases. According to SHG measurements, the surface film concentration is almost proportional to the bulk concentration. This concurs with the decreasing disorder parameter measured with SFG. A higher surface concentration of a charged interface will lead to a better oriented water subphase. This would result in an increased water signal. On the other hand, it is predicted that the bromine counter ions condense at higher concentrations to the cationic lipid. This will be represented by a much lower signal. In our case we see barely any modification in the water

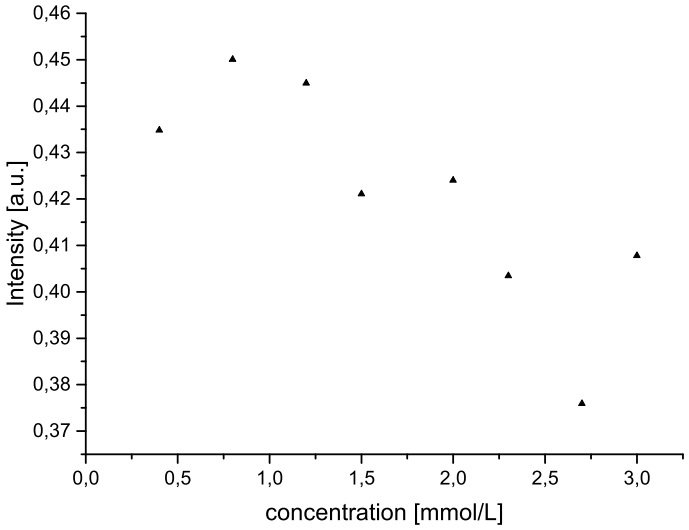

Figure 6.9.: Integral water intensity of the SFG spectra of **C12-DMP-Br** in the wavenumber range 3000-3600 cm^{-1} at different concentrations.

signal. As discussed in section 3.1.3, a deep reaching little oriented interfacial water may give rise to the same signal intensity as a highly oriented shallow water layer. In this case the two effects of the denser packed lipid layer and the increased condensation seem to nullify each other so that the resulting intensity remains almost constant. In figure 6.11 the different processes are shown in a schematic sketch. Our postulated mechanism is displayed by depiction a) for low concentrations and d) for high concentrations.

The little change in the intensity may have many reasons. A way to test for the hypothesis, is to add a halide salt to the solution. We used **NaBr** and **NaI**. In both cases the intensity of the water spectra diminishes dramatically (see figure 6.10 for the addition of **NaBr**). This drop indicates a major change in the water structure. In this case not only the bromide counterions of the surfactants are present, but as well the additional anions added with the **NaBr**. Sodium has a low surface propensity and is furthermore repelled from the surface by the **C12-DMP** cation. It is therefore unlikely that it is located at the surface. Bromide, however, has a high surface propensity and according to Petrov et al.[109] it is situated close to the headgroup of the lipid. Therefore, the change of the interfacial water structure is most likely due to the additional bromide. Iodide is even more polarizable and has therefore a relatively high probability to reside at

the interface. Therefore, the drop of the water signal has in this case most likely the same origin as for bromide.

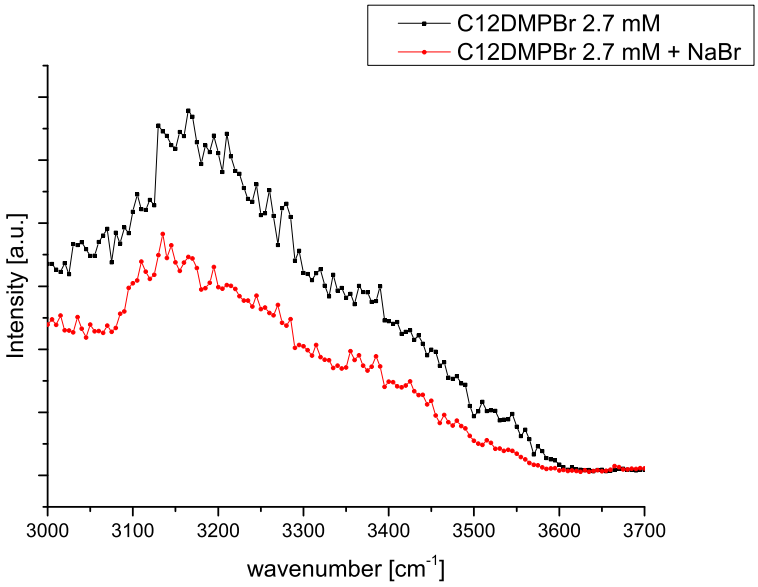

Figure 6.10.: SFG spectra of **C12-DMP-Br** over pure water (black) and **NaBr** solution (red). The corresponding spectra of **NaI** (not shown) reveal an analogous behavior.

The additional anions are in vicinity to the positive headgroups, and so less water is oriented by charge separation. This time the negation of the two effects is overcome by force pushing the anion condensation and therefore lowering the water signal.

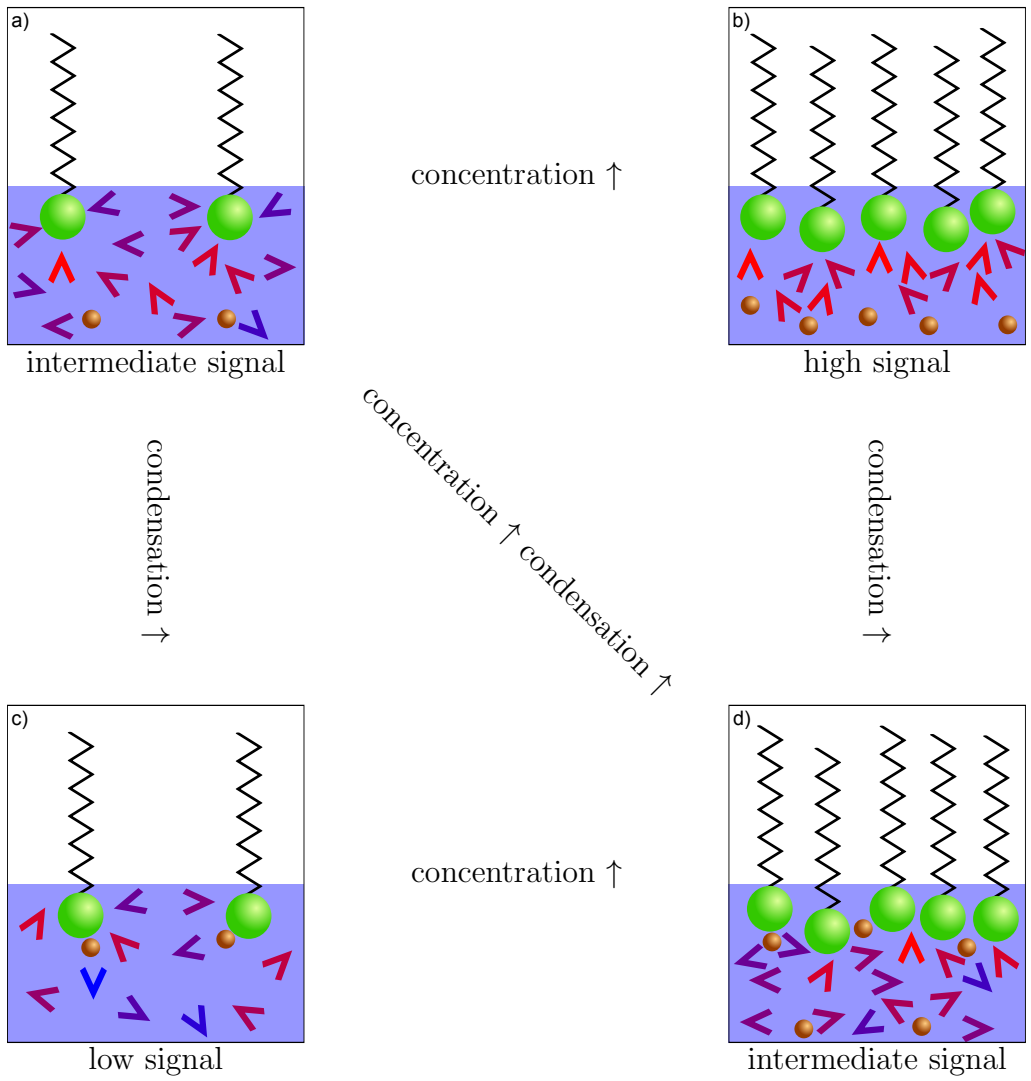

Figure 6.11.: Schematic representation of possible arrangements of the **C12-DMP** cations and the corresponding **Br** anions. The arrow heads denote the water molecules, where red water stands for well oriented water, while blue water is unoriented.
a) At low concentration and only little condensation of the anions the water is partially oriented. This leads to an intermediate SFG signal.
b) Assuming that the condensation remains constant, an increase in concentration will lead to well oriented interfacial water, which can be seen as a highly enhanced SFG signal compared to the low concentration case.
c) In this case the condensation is higher than in a). The water is less oriented and the SFG signal will be significantly lower than in the case with no condensation.
d) Both, the concentration and the amount of condensation are increased compared to the initial system. The water structure is relatively similar to a), and therefore hardly distinguishable with SFG.

7 Concluding Remarks

In this work I investigated a series of surface specific effects at the air water interface. Several systems were examined. I could show in all systems a strong effect of the molecules on the interfacial structure. In the following I will recapitulate the most important findings and outline the forward-looking implications of this research.

I investigated the two isoelectronic octahedral complexes potassium hexacyanoferrate(II) (**HCF**) and potassium hexacyanocobaltate(III) (**HCC**) (chapter 4). Two major results can be drawn from these systems. First of all, both anions give rise to a SFG signal. This is due to selection rules only possible when the octahedral symmetry is abandoned. This is a strong indication that the anions are indeed close to the interface and the nonisotropic force field pushes either the anion itself or its solvation shell in a non-centrosymmetric arrangement. The second major finding is the difference in the behavior of **HCF** and **HCC**. While the order of the interfacial water increases almost proportional to the salt concentration of **HCF**, the effect is reversed for **HCC**. Since I found for **HCF** with DRS solvent separated ion pairs in the bulk, I postulated for **HCC** contact ion pairs. This different type of ion pairs would explain the completely different surface architecture. This postulation is drawn from SFG data and requires verification with DRS measurements. It becomes clear that the type of ion pair may have a strong impact on the system. Other than the ion pairing in most theories, it is here necessary to distinguish not only between ion pairing and non-ion pairing, but as well between the types of ion pairing.

I investigated not only the pure air electrolyte interface, but as well surfaces covered with an organic Langmuir film. In the second part of the experimental analysis the focus was on the structure of the Langmuir monolayer build up by a mixture of a phospholipid and an amphiphilic photosensitizer (**Ru==**) in order to optimize a catalytic system (chapter 5). Since the initial catalytic system has

several components in a complicated architecture, I used several simplifications, e.g. I replaced the vesicle double layer by a monolayer at the air-water interface. The soluble reactants are of minor interest, because they have a high surface propensity and it is therefore likely that they are located at the interface. Nevertheless, I examined the impact of them as well. The photosensitizer **Ru==** is amphiphilic and is therefore arranged in the Langmuir layer. Astonishingly, the choice of the phospholipid has great impact on the reaction. This means that the photosensitizer must be build into the membrane in a specific fashion. I used surface-pressure-isotherms and SFG to characterize the lipid membrane. In these investigations I could correlate the turnover numbers with the disorder parameter, however, there is still a lack in understanding the underlying structural factors. Since I investigated an over-simplistic system, I do not know whether the observed effects occur in the real catalytic system as well.

The last investigated system (chapter 6) is based on a Langmuir film as well. However, only the pure **C12-DMP-Br** is used and the focus is on both, on the structure of the cationic surfactant and on the counter ion pairing of the bromide. On this system quite a bit of work was performed prior to my investigations, especially with ellipsometry and SHG. I used SFG to validate the following thesis of the ion arrangement: The surfactant concentration increases in an almost direct proportional manner with concentration. Meanwhile the amount of condensed bromide counterion increases with concentration. This model was introduced to be able to fit the ellipsometric data. The first statement was indicated by SHG data and could be reproduced with SFG by taking the disorder parameter into account. For the second part I took a closer look at the interfacial water structure. A low SFG water signal is an indication for either a low surface charge or a significant amount of counter ion condensation, a high SFG water signal vice versa. Over the investigated concentration range the SFG signal remains almost constant. I interpreted this such that an increase of both, the surface charge and the condensation, cancel each other and lead to an unchanged SFG signal. To verify this thesis I shifted the equilibrium by adding additional bromide anions to increase the impact of condensation. This reduced the water signal dramatically. With this I could affirm the model introduced for the ellipsometric data.

In this work the surface arrangement was investigated on several systems. As in most cases, finding an answer to one topic evokes several questions on a related topic. There is a basic understanding of the systems, yet we do not know why e.g. **HCF** and **HCC** behave in a different manner. We know that the phospholipid

DMPC incorporates **Ru==** better than **DPPC**, but we do not know why a small change in chainlength has such a large impact on the system. We know that the condensation of **C12-DMP-Br** increases at high concentrations, but we have not mechanism to explain it based on first principles. I hope I could contribute a little bit perception to the big puzzle of ion specific effects, however, I cannot offer a full explanation for all the effects presented in this work.

A Appendix

A.1. Character Tables

Symmetry plays a major role for the selection rules of SFG. In the following the relevant character tables are shown. For clarity the modes are color coded with red for IR-active modes, green for Raman active modes and blue for IR and Raman active modes, which are therefore SFG active.

$\mathbf{O_h}$	E	$8C_3$	$6C_2$	$6C_4$	$3C_2$	i	$6S_4$	$8S_6$	$3\sigma_h$	$6\sigma_d$	IR	Raman
A_{1g}	1	1	1	1	1	1	1	1	1	1		$x^2+y^2+z^2$
A_{2g}	1	1	-1	-1	1	1	1	-1	-1	1		
E_g	2	-1	0	0	2	2	-1	0	0	2		$(2z^2\text{-}x^2\text{-}y^2,\ x^2\text{-}y^2)$
T_{1g}	3	0	-1	1	-1	3	0	-1	1	-1		
T_{2g}	3	0	1	-1	-1	3	0	1	-1	-1		$(xz,\ yz,\ xy)$
A_{1u}	1	1	1	1	1	-1	-1	-1	-1	-1		
A_{2u}	1	1	-1	-1	1	-1	-1	1	1	-1		
E_u	2	-1	0	0	2	-2	1	0	0	-2		
T_{1u}	3	0	-1	1	-1	-3	0	1	-1	1	$(x,\ y,\ z)$	
T_{2u}	3	0	1	-1	-1	-3	0	-1	1	1		

Table A.1.: Character Table O_h.

$\mathbf{D_{2h}}$	E	$C_2(z)$	$C_2(y)$	$C_2(x)$	i	$\sigma(xy)$	$\sigma(xz)$	$\sigma(yz)$	IR	Raman
A_g	1	1	1	1	1	1	1	1		$x^2,\ y^2,\ z^2$
B_{1g}	1	1	-1	-1	1	1	-1	-1		xy
B_{2g}	1	-1	1	-1	1	-1	1	-1		xz
B_{3g}	1	-1	-1	1	1	-1	-1	1		yz
A_u	1	1	1	1	-1	-1	-1	-1		
B_{1u}	1	1	-1	-1	-1	-1	1	1	z	
B_{2u}	1	-1	1	-1	-1	1	-1	1	x	
B_{3u}	1	-1	-1	1	-1	1	1	-1	x	

Table A.2.: Character Table D_{2h}.

$\mathbf{D}_{3d}$	E	$2C_3$	$3C_2$	i	$2S_6$	$3\sigma_d$	IR	Raman
A_{1g}	1	1	1	1	1	1		$x^2+y^2,\ z^2$
A_{2g}	1	1	-1	1	1	-1		
E_g	2	-1	0	2	-1	0		$(x^2-y^2,\ xy),\ (xz,\ yz)$
A_{1u}	1	1	1	-1	-1	-1		
A_{2u}	1	1	-1	-1	-1	1	z	
E_u	2	-1	0	-2	1	0	$(x,\ y)$	

Table A.3.: Character Table D_{3d}.

$\mathbf{D}_{4h}$	E	$2C_4$	C_2	$2C'_2$	$2C''_2$	i	$2S_4$	σ_h	$2\sigma_v$	$2\sigma_d$	IR	Raman
A_{1g}	1	1	1	1	1	1	1	1	1	1		$x^2+y^2,\ z^2$
A_{2g}	1	1	1	-1	-1	1	1	1	-1	-1		
B_{1g}	1	-1	1	1	-1	1	-1	1	1	-1		x^2-y^2
B_{2g}	1	-1	1	-1	1	1	-1	1	-1	1		xy
E_g	2	0	-2	0	0	2	0	-2	0	0		$(xz,\ yz)$
A_{1u}	1	1	1	1	1	-1	-1	-1	-1	-1		
A_{2u}	1	1	1	-1	-1	-1	-1	-1	1	1	z	
B_{1u}	1	-1	1	1	-1	-1	1	-1	-1	1		
B_{2u}	1	-1	1	-1	1	-1	1	-1	1	-1		
E_u	2	0	-2	0	0	-2	0	2	0	0	$(x,\ y)$	

Table A.4.: Character Table D_{4h}.

C_{2v}	E	C_2	σ_v	σ'_v	IR	Raman
A_1	1	1	1	1	z	$x^2,\ y^2,\ z^2$
A_2	1	1	-1	-1		xy
B_1	1	-1	1	-1	x	xz
B_2	1	-1	-1	1	y	yz

Table A.5.: Character Table C_{2v}.

C_{3v}	E	$2C_3$	$3\sigma_v$	IR	Raman
A_1	1	1	1	x	$x^2+y^2,\ z^2$
A_2	1	1	-1		
E	2	-1	0	(y,z)	$(x^2-y^2,xy),(xz,yz)$

Table A.6.: Character Table C_{3v}.

C_{4v}	E	$2C_4$	C_2	$2\sigma_v$	$2\sigma_d$	IR	Raman
A_1	1	1	1	1	1	z	x^2+y^2,z^2
A_2	1	1	1	-1	-1		
B_1	1	-1	1	1	-1		x^2-y^2
B_2	1	-1	1	-1	1		xy
E	2	0	-2	0	0	(x,y)	(xz,yz)

Table A.7.: Character Table C_{4v}.

A.2. Symmetry Reduction

High order symmetry groups may loose its symmetry due to external effects. In the modes of the octahedral symmetry are attributed to the corresponding lower symmetry groups (see section 4.3.1). For clarity the modes are again color coded as in section A.1. Only the non-centrosymmetric groups C_{2v}, C_{3v} and C_{4v} give rise to an SFG active signal (blue modes). This is relevant for the interpretation of the data in section 4.

$\mathbf{O_h}$	$\rightarrow$	$\mathbf{D_{2h}}$	$\rightarrow$	$\mathbf{C_{2v}}$
A_{1g}	$\rightarrow$	A_g	$\rightarrow$	A_1
A_{2g}	$\rightarrow$	B_{1g}	$\rightarrow$	A_2
E_g	$\rightarrow$	A_g+B_{1g}	$\rightarrow$	A_1+A_2
T_{1g}	$\rightarrow$	$B_{1g}+B_{2g}+B_{3g}$	$\rightarrow$	$A_2+B_1+B_2$
T_{2g}	$\rightarrow$	$A_g+B_{2g}+B_{3g}$	$\rightarrow$	$A_1+B_1+B_2$
A_{1u}	$\rightarrow$	A_u	$\rightarrow$	A_2
A_{2u}	$\rightarrow$	B_{1u}	$\rightarrow$	A_1
E_u	$\rightarrow$	A_u+B_{1u}	$\rightarrow$	A_1+A_2
T_{1u}	$\rightarrow$	$B_{1u}+B_{2u}+B_{3u}$	$\rightarrow$	$A_1+B_1+B_2$
T_{2u}	$\rightarrow$	$A_u+B_{2u}+B_{3u}$	$\rightarrow$	$A_2+B_1+B_2$

Table A.8.: Symmetry reduction of an octahedral symmetry upon edge distortion.

$\mathbf{O_h}$	$\rightarrow$	$\mathbf{D_{3d}}$	$\rightarrow$	$\mathbf{C_{3v}}$
A_{1g}	$\rightarrow$	A_{1g}	$\rightarrow$	A_1
A_{2g}	$\rightarrow$	A_{2g}	$\rightarrow$	A_2
E_g	$\rightarrow$	E_g	$\rightarrow$	E
T_{1g}	$\rightarrow$	$A_{2g}+E_g$	$\rightarrow$	A_2+E
T_{2g}	$\rightarrow$	$A_{1g}+E_g$	$\rightarrow$	A_1+E
A_{1u}	$\rightarrow$	A_{1u}	$\rightarrow$	A_1
A_{2u}	$\rightarrow$	A_{2u}	$\rightarrow$	A_2
E_u	$\rightarrow$	E_u	$\rightarrow$	E
T_{1u}	$\rightarrow$	$A_{2u}+E_u$	$\rightarrow$	A_2+E
T_{2u}	$\rightarrow$	$A_{1u}+E_u$	$\rightarrow$	A_1+E

Table A.9.: Symmetry reduction of an octahedral symmetry upon face distortion.

$\mathbf{O_h}$	$\rightarrow$	$\mathbf{D_{4h}}$	$\rightarrow$	$\mathbf{C_{4v}}$
A_{1g}	$\rightarrow$	A_{1g}	$\rightarrow$	A_1
A_{2g}	$\rightarrow$	B_{1g}	$\rightarrow$	B_1
E_g	$\rightarrow$	$A_{1g}+B_{1g}$	$\rightarrow$	A_1+B_1
T_{1g}	$\rightarrow$	$A_{2g}+E_g$	$\rightarrow$	A_2+E
T_{2g}	$\rightarrow$	$B_{2g}+E_g$	$\rightarrow$	B_2+E
A_{1u}	$\rightarrow$	A_{1u}	$\rightarrow$	A_2
A_{2u}	$\rightarrow$	B_{1u}	$\rightarrow$	B_2
E_u	$\rightarrow$	$A_{1u}+B_{1u}$	$\rightarrow$	A_2+B_2
T_{1u}	$\rightarrow$	$A_{2u}+E_u$	$\rightarrow$	A_1+E
T_{2u}	$\rightarrow$	$B_{2u}+E_u$	$\rightarrow$	B_1+E

Table A.10.: Symmetry reduction of an octahedral symmetry upon corner distortion.

A.3. Chemicals

Table A.11.: List of chemicals used for these investigations.

Abbreviation	Long Name	Manufacturer	Purity
Asc	L-(+)-ascorbic acid	Caelo	puriss.
Chloroform	Chloroform	Merck	p.A.
C12-DMP-bet	2-[4-(dimethylamino)pyridinio]dodecanoate	synthesized at MPIKG Golm	-
C12-DMP-Br	1-dodecyl-4-(dimethylamino)pyridinium bromide	synthesized at MPIKG Golm	-
DMPC	1,2-dimyristoyl-*sn*-glycero-3-phosphocholine	Avanti Polar Lipids	>99%
DMPC-d	1,2-dimyristoyl-d54-*sn*-glycero-3-phosphocholine	Avanti Polar Lipids	>99%
DOPC	1,2-dioleoyl-*sn*-glycero-3-phosphocholine	Avanti Polar Lipids	>99%
DPPC	1,2-dipalmitoyl-*sn*-glycero-3-phosphocholine	Avanti Polar Lipids	>99%
DPPC-d	1,2-dipalmitoyl-d62-*sn*-glycero-3-phosphocholine	Avanti Polar Lipids	>99%
Ethanol	Ethanol	Sigma-Aldrich	≥99.8%
Fe-Fe	structure see figure 5.1	synthesized by König group	-
HCC	Potassium hexacyanocobaltate(III)	Sigma-Aldrich	≥97.0%
HCl	Hydrochloric acid, 37%	Fluka Chemicals	p.A.
HCF	Potassium hexacyanoferrate(II) trihydrate	Sigma-Aldrich	Bio Ultra, ≥99.5%
H_2O_2	Hydrogen peroxide, 30%	VWR Chemicals	p.a.
H_2SO_4	Sulfuric acid	Sigma Aldrich	95.0-97.0%
H_2SO_5	Peroxymonosulfuric acid	fresh prepared from **H_2SO_4** and **H_2O_2**	
NaBr	Sodium Bromide	Merck	extra pure
NaI	Sodium Iodide	Fluka	≥99.5%
Ru	structure see figure 5.1	synthesized by König group	-
Ru==	structure see figure 5.1	synthesized by König group	-

A.4. Devices

Table A.12.: List of devices used for these investigations.

Device	Unit	Manufacturer	Model
BAM	**Lasing Unit**	NFT	BAM 1 plus
BAM	**ccd Camera**	teli	CS3130
DRS	**Vector Network Analyzer**	Agilent	E8364B
DRS	**20 GHz open-ended coaxial probe**	Agilent	85070E-20
DRS	**50 GHz open-ended coaxial probe**	Agilent	85070E-50
DRS	**waveguide interferometer (60-89 GHz)**	-	-
Langmuir Trough for Laser		Riegler & Kirstein	-
Langmuir Trough Isotherm		Nima	Langmuir Film Balance 601
NMR		Bruker	Avance 300
Purification Device		Lunkenheimer	-
SFG	**Lasing Unit**	Ekspla	PL2143 A/SS
SFG	**OPG Unit**	Ekspla	PG401/DFG2-10P
SFG	**Detector Unit**	Acton	SpectraPro 2150i
SFG	**Optical Table**	Newport	RS4000TM
Tensiometer		Krüss	Processor Tensiometer K100

List of Figures

List of Tables

Bibliography

[1] Chung, E.-S.; Soden, B.; Sohn, B. J.; Shi, L. *Proceedings of the National Academy of Sciences* **2014**, *111*, 11636–11641.

[2] Hofmeister, F. *Archiv für Experimentelle Pathologie und Pharmakologie* **1888**, *24*, 247–260.

[3] Abernethy, J. L. *Journal of Chemical Education* **1967**, *44*, 177–180.

[4] Csapo, J.; v. Klobusitzky, D. *Biochemische Zeitschrift* **1925**, *157*, 354–358.

[5] Wilson, E. K. *Chemical & Engineering News Archive* **2012**, *90*, 42–43.

[6] Marcus, Y. *Chemical Reviews* **2009**, *109*, 1346–1370, PMID: 19236019.

[7] Gurney, R. W. *Ionic Processes in Solution*; McGraw-Hill Book Co., 1953.

[8] Collins, K. D.; Washabaugh, M. W. *Quarterly Reviews of Biophysics* **1985**, *18*, 323–422.

[9] Lee, J. D. *Concise Inorganic Chemistry. 4th Ed.*; Chapman and Hall, 1991.

[10] Mejri, M.; BenSouissi, A.; Aroulmoji, V.; Roge, B. *Spectrochimica Acta Part A* **2009**, *73*, 6–10.

[11] Al-Maaieh, A.; Flanagan, D. R. *Journal of Pharmaceutical Sciences* **2002**, *91*, 1000–1008.

[12] Shimizu, S. *Food & Function* **2015**,

[13] Butt, H.-J.; Graf, K.; Kappl, M. *Physics and Chemistry of Interfaces*, 3rd ed.; Wiley-VHC, 2013.

[14] Helmholtz, H. *Annalen der Physik* **1853**, *165*, 211–233.

[15] Gouy, M. *Journal de Physique* **1910**, *9*, 457–468.

[16] Chapman, D. L. *Philosophical Magazine Series 6* **1913**, *25*, 475–481.

[17] Stern, O. *Zeitschrift fuer Elektrochemie und Angewandte Physikalische Chemie* **1924**, *30*, 508–516.

[18] Grahame, D. C. *Chemical Reviews* **1947**, *41*, 441–501.

[19] Warszynski, P.; Lunkenheimer, K.; Czichocki, G. *Langmuir* **2002**, *18*, 2506–2514.

[20] Para, G.; Jarek, E.; Warszynski, P. *Colloids and Surfaces A* **2005**, *261*, 65–73.

[21] Goralczyk, D.; Hac, K.; Pawel, W. *Colloids and Surfaces A* **2003**, *220*, 55–60.

[22] Kunz, W.; Lo Nostro, P.; Ninham, B. W. *Current Opinion in Colloid and Interface Science* **2004**, *9*, 1–18.

[23] Brady, A. P. *The Journal of Physical and Colloid Chemistry* **1949**, *53*, 56–67.

[24] Hua, X. Y.; Rosen, M. J. *Journal of Colloid and Interface Science* **1982**, *87*, 469–477.

[25] Bae, S.; Haage, K.; Wantke, K.; Motschmann, H. *The Journal of Physical Chemistry B* **1999**, *103*, 1045–1050.

[26] Jarvis, N. L.; Scheiman, M. A. *The Journal of Physical Chemistry* **1968**, *78*, 74–78.

[27] Knipping, E. M.; Lakin, M. J.; Foster, K. L.; Jungwirth, P.; Tobias, D. J.; Gerber, R. B.; Dabdub, D.; Finlayson-Pitts, B. J. *Science* **2000**, *288*, 301–306.

[28] Hu, J. H.; Shi, Q.; Davidovits, P.; Worsnop, D. R.; Zahniser, M. S.; Kolb, C. E. *The Journal of Physical Chemistry* **1995**, *99*, 8768–8776.

[29] Hofmeister, F. *Archiv für Experimentelle Pathologie und Pharmakologie* **1888**, *25*, 1–30.

[30] Hofmeister, F. *Archiv für Experimentelle Pathologie und Pharmakologie* **1890**, *27*, 395–413.

[31] Hofmeister, F. *Archiv für Experimentelle Pathologie und Pharmakologie* **1891**, *28*, 210–238.

[32] Jungwirth, P.; Tobias, D. J. *Chemical Reviews* **2006**, *106*, 1259–1281.

[33] Jungwirth, P.; Tobias, D. J. *Journal of Physical Chemistry B* **2001**, *105*, 10468–10472.

[34] Powell, C. J.; Jablonski, A. *NIST Electron Inelastic-Mean-Free-Path Database Version 1.2*; 2010.

[35] Jungwirth, P.; Tobias, D. J. *Journal of Physical Chemistry B* **2002**, *106*, 6361–6373.

[36] Ghosal, S.; Hemminger, J. C.; Bluhm, H.; Mun, B. S.; Hebenstreit, E. L. D.; Ketteler, G.; Ogletree, D. F.; Requejo, F. G.; Salmeron, M. *Science* **2005**, *307*, 563–566.

[37] Liu, D.; Ma, G.; Levering, L. M.; Allen, H. C. *The Journal of Physical Chemistry B* **2004**, *108*, 2252–2260.

[38] Du, Q.; Superfine, R.; Freysz, E.; Shen, Y. R. *Physical Review Letters* **1993**, *70*, 2313–16.

[39] Cheng, J.; Vecitis, C. D.; Hoffmann, M. R.; Colussi, A. J. *The Journal of Physical Chemistry B* **2006**, *110*, 25598–25602.

[40] Gurau, M. C.; Lim, S.-M.; Castellana, E. T.; Albertorio, F.; Kataoka, S.; Cremer, P. S. *Journal of the American Chemical Society* **2004**, *126*, 10522–10523.

[41] Chen, X.; Yang, T.; Kataoka, S.; Cremer, P. S. *Journal of the American Chemical Society* **2007**, *129*, 12272–12279.

[42] Aroti, A.; Leontidis, E.; Maltseva, E.; Brezesinski, G. *The Journal of Physical Chemistry B* **2004**, *108*, 15238–15245.

[43] Petersen, P. B.; Saykally, R. J. *The Journal of Physical Chemistry B* **2006**, *110*, 14060–14073.

[44] Petersen, P. B.; Saykally, R. J.; Mucha, M.; Jungwirth, P. *The Journal of Physical Chemistry B* **2005**, *109*, 10915–10921.

[45] Petersen, P. B.; Saykally, R. J. *Chemical Physics Letters* **2004**, *397*, 51–55.

[46] Wojciechowski, K.; Gutberlet, T.; Konovalov, O. *Colloids and Surfaces A* **2012**, *413*, 184–190.

[47] Flores, S. C.; Kherb, J.; Cremer, P. S. *The Journal of Physical Chemistry C* **2012**, *116*, 14408–14413.

[48] Brandes, E.; Stage, C.; Motschmann, H.; Rieder, J.; Buchner, R. *The Journal of Chemical Physics* **2014**, *141*, 18C509.

[49] Hua, W.; Verreault, D.; Huang, Z.; Adams, E. M.; Allen, H. C. *The Journal of Physical Chemistry B* **2014**, *118*, 8433–8440.

[50] Hua, W.; Verreault, D.; Allen, H. C. *The Journal of Physical Chemistry C* **2014**, *118*, 24941–24949.

[51] Vlachy, N.; Jagoda-Cwiklik, B.; Vacha, R.; Touraud, D.; Jungwirth, P.; Kunz, W. *Advances in Colloid and Interface Science* **2009**, *146*, 42–47.

[52] Barthel, J.; Buchner, R.; Steger, H. *Wissenschaftliche Zeitschrift der Technischen Hochschule Carl Schorlemmer Leuna-Merseburg* **1989**, *31*, 409–423.

[53] de Broglie, L. *Philos* **1924**, *47*, 446–458.

[54] Hentschel, K. *Archive for History of Exact Sciences* **2001**, *55*, 297–344.

[55] Sokhan, V. P.; Tildesley, D. J. *Molecular Physics* **1997**, *92*, 625–640.

[56] Knoll, W. *Annual Review of Physical Chemistry* **1998**, *49*, 569–638.

[57] Moad, A. J.; Simpson, G. J. *The Journal of Physical Chemistry B* **2004**, *108*, 3548–3562.

[58] Lambert, A. G.; Davies, P. B.; Neivandt, D. J. *Applied Spectroscopy Reviews* **2005**, *40*, 103–145.

[59] Ma, G.; Allen, H. C. *Langmuir* **2006**, *22*, 5341–5349.

[60] Du, Q.; Freysz, E.; Shen, Y. R. *Science* **1994**, *264*, 826–828.

[61] Diels, J.-C.; Rudolph, W. In *Ultrashort Laser Pulse Phenomena*, 2nd ed.; Liao, P., Kelley, P., Eds.; Academic Press, 2006.

[62] Geusic, J. E.; Marcos, H. M.; Uitert, L. G. V. *Applied Physics Letters* **1964**, *4*, 182–184.

[63] Eckardt, R. C.; Nabors, C. D.; Kozlovsky, W. J.; Byer, R. L. *Journal of the Optical Society of America* **1991**, *8*, 646–667.

[64] Buchner, R. In *Approaches to the Structure and Dynamics of Liquids: Experiments, Theories and Simulations*; Samios, J., Durov, V. A., Eds.; Springer Netherlands, 2004; Chapter Dielectric Spectroscopy of Solutions.

[65] Kremer, F., Schönhals, A., Eds. *Broadband Dielectric Spectroscopy*; Springer Berlin Heidelberg, 2003.

[66] Hunger, J.; Stoppa, A.; Schroedle, S.; Hefter, G.; Buchner, R. *ChemPhysChem* **2009**, *10*, 723–733.

[67] Buchner, R. *Pure and Applied Chemistry* **2008**, *80*, 1239–1252.

[68] Böttcher, C. F. J. *Theory of Electric Polarization*; Elsevier, Amsterdam, Netherlands, vol 1, 1973.

[69] Böttcher, C. F. J. *Theory of Electric Polarization*; Elsevier, Amsterdam, Netherlands, vol 2, 1978.

[70] Barthel, J.; Hetzenauer, H.; Buchner, R. *Berichte der Bunsengesellschaft für physikalische Chemie* **1992**, *96*, 1424–1432.

[71] Debye, *New York: Chemical Catalog Co., Inc.* **1929**, *48*, 1036–1037.

[72] Laage, D.; Stirnemann, G.; Sterpone, F.; Rey, R.; Hynes, J. T. *Annual Review of Physical Chemistry* **2011**, *62*, 395–416.

[73] Bakker, H. J.; Skinner, J. L. *Chemical Reviews* **2010**, *110*, 1498–1517, PMID: 19916491.

[74] Qvist, J.; Halle, B. *Journal of the American Chemical Society* **2008**, *130*, 10345–10353.

[75] Laage, D.; Hynes, J. T. *Science* **2006**, *311*, 832–835.

[76] Buchner, R.; Hoelzl, C.; Stauber, J.; Barthel, J. *Physical Chemistry Chemical Physics* **2002**, *4*, 2169–2179.

[77] Buchner, R.; Hefter, G. *Physical Chemistry Chemical Physics* **2009**, *11*, 8984–8999.

[78] Kaatze, U. *Journal of Solution Chemistry* **1997**, *26*, 1049–1112.

[79] Buchner, R.; Barthel, J.; Stauber, J. *Chemical Physics Letters* **1999**, *306*, 57–63.

[80] Barthel, J.; Buchner, R.; Wurm, B. *Journal of Molecular Liquids* **2002**, *98*, 51–69.

[81] Fukasawa, T.; Sato, T.; Watanabe, J.; Hama, Y.; Kunz, W.; Buchner, R. *Physical Review Letters* **2005**, *95*, 197802.

[82] Kaatze, U.; Behrends, R.; Pottel, R. *Journal of Non-Crystalline Solids* **2002**, *305*, 19–28.

[83] Wachter, W.; Kunz, W.; Buchner, R.; Hefter, G. *The Journal of Physical Chemistry A* **2005**, *109*, 8675–8683.

[84] Schrödle, S.; Rudolph, W. W.; Hefter, G.; Buchner, R. *Geochimica et Cosmochimica Acta* **2007**, *71*, 5287–5300.

[85] Hofer, T. S.; Randolf, B. R.; Rode, B. M. *Physical Chemistry Chemical Physics* **2005**, *7*, 1382–1387.

[86] Hofer, T.; Pribil, A.; Randolf, B. *Pure and Applied Chemistry* **2009**, *80*, 1195–1210.

[87] Mancinelli, R.; Botti, A.; Bruni, F.; Ricci, M. A.; Soper, A. K. *Physical Chemistry Chemical Physics* **2007**, *9*, 2959–2967.

[88] Baar, C.; Buchner, R.; Kunz, W. *The Journal of Physical Chemistry B* **2001**, *105*, 2906–2913.

[89] Tromans, A.; May, P. M.; Hefter, G.; Sato, T.; Buchner, R. *The Journal of Physical Chemistry B* **2004**, *108*, 13789–13795.

[90] Wachter, W.; Buchner, R.; Hefter, G. *The Journal of Physical Chemistry B* **2006**, *110*, 5147–5154.

[91] Rahman, H. M. A.; Hefter, G.; Buchner, R. *The Journal of Physical Chemistry B* **2012**, *116*, 314–323.

[92] Eigen, M.; Tamm, K. *Zeitschrift für Elektrochemie, Berichte der Bunsengesellschaft für physikalische Chemie* **1962**, *66*, 93–107.

[93] Hefter, G. *Pure and Applied Chemistry* **2006**, *78*, 1571–1586.

[94] Pockels, A.; Strutt Baron Rayleigh, J. W. *Nature* **1891**, *43*, 437–439.

[95] Lunkenheimer, K.; Pergande, H. J.; Krueger, H. *Review of Scientific Instruments* **1987**, *58*, 2313–16.

[96] Drude, P. *Annalen der Physik* **1887**, *268*, 584–625.

[97] Drude, P. *Annalen der Physik* **1889**, *272*, 532–560.

[98] Drude, P. *Annalen der Physik* **1889**, *272*, 865–897.

[99] Hommel, E. L.; Allen, H. C. *Analyst* **2003**, *128*, 750–755.

[100] Brandes, E.; Karageorgiev, P.; Viswanath, P.; Motschmann, H. *The Journal of Physical Chemistry C* **2014**, *118*, 26629–26633.

[101] Sega, M.; Kantorovich, S. S.; Holm, C.; Arnold, A. *The Journal of Chemical Physics* **2014**, *140*, 211101.

[102] Eiberweiser, A.; Nazet, A.; Hefter, G.; Buchner, R. *The Journal of Physical Chemistry B* **2015**, *119*, 5270–5281, PMID: 25826464.

[103] Hansen, M.; Li, F.; Sun, L.; Konig, B. *Chemical Science* **2014**, *5*, 2683–2687.

[104] Troppmann, S.; Brandes, E.; Motschmann, H.; Li, F.; Wang, M.; Sun, L.; König, B. *European Journal of Inorganic Chemistry* **2016**, *2016*, 554–560.

[105] Teppner, R.; Bae, S.; Haage, K.; Motschmann, H. *Langmuir* **1999**, *15*, 7002–7007.

[106] Hicks, J. M.; Kemnitz, K.; Eisenthal, K. B.; Heinz, T. F. *The Journal of Physical Chemistry* **1986**, *90*, 560–562.

[107] Teppner, R.; Haage, K.; Wantke, D.; Motschmann, H. *The Journal of Physical Chemistry B* **2000**, *104*, 11489–11496.

[108] Pfohl, T.; Möhwald, H.; Riegler, H. *Langmuir* **1998**, *14*, 5285–5291.

[109] Petrov, M.; Minofar, B.; Vrbka, L.; Jungwirth, P.; Koelsch, P.; Motschmann, H. *Langmuir* **2006**, *22*, 2498–2505.